
Inertial Noise Post-Correction in Atom
Interferometers Measuring
the Local Gravitational Acceleration

Von der Fakultät für Mathematik und Physik
der Gottfried Wilhelm Leibniz Universität Hannover

zur Erlangung des Grades

Doktor der Naturwissenschaften

Dr. rer. nat. -

genehmigte Dissertation von

Logan Latham Richardson

geboren am 19.12.1989,

in Orlando Florida, United States of America

Referent: Prof. Dr. Ernst M. Rasel
Korreferent: Dr. Felipe Guzmán
Korreferent: Dr. Dennis Schlippert
Tag der Promotion: 16.01.2019

Abstract

Exploiting the quantum nature of atoms through the use of matter-wave interferometry has led to the development of devices sensitive to, among other things, the local gravitational acceleration. Measurements of the gravitational acceleration have applications ranging from detection of subterranean density differences to observation of general relativistic effects. Light-pulse atom interferometers provide an absolute measurement of the gravitational acceleration with a sensitivity competitive and even surpassing the performance of classical sensors. The advantages of atom interferometers as inertial measurement devices have led to efforts in increasing sensitivity and decreasing the physical dimensions of the measurement head, allowing them to be more transportable for field use applications. With increasing sensitivity, it becomes more critical to address the noise source limitations affecting the measurement, specifically the influence of ground motion on measurements. Vibrations coupling into the inertial reference add a time varying phase shift uncommon to the paths of the interferometer. This limitation is especially pertinent to transportable atom gravimeters measuring in the field where inertial noise is typically far higher than in relatively quiet laboratory environments.

Within this work, implementation and demonstration of inertial noise post-correction in an atom interferometer is shown within low inertial noise environments and simulated strong motion environments. For a high pulse separation time atom interferometer ($T = 78$ ms) post-correction yielded an increase in the short term stability from $4.4 \times 10^{-6} \text{ m/s}^2/\sqrt{\text{Hz}}$ to $9.2 \times 10^{-7} \text{ m/s}^2/\sqrt{\text{Hz}}$. This method was reproduced with a different motion sensor to perform post-correction in a high motion environment, generated by introducing additional movement onto the inertial reference. By performing post-correction in the high motion environment, we were able to show an increase of short term stability of $\gamma = 73.8$. Current limitations to the post-correction resulted from self noise resolution limitations and spectral resolutions limitations. Beyond corrections with commercially available sensors, this work demonstrates the first post-correction with a next generation compact optomechanical sensor. This optomechanical sensor is formed from monolithic fused silica capable of sensitively measuring accelerations of a harmonic oscillator test mass, which can be read-out optically. This novel motion sensor has the advantage to any previously shown sensor used for post-correction in the capacity that it is vacuum compatible, insensitive to magnetic fields and has the potential to be implemented directly into the inertial reference. In this work, inertial noise post-correction in a simulated high motion environment is shown, correcting from a short term stability of $8 \times 10^{-3} \text{ m/s}^2/\sqrt{\text{Hz}}$ to $5 \times 10^{-4} \text{ m/s}^2/\sqrt{\text{Hz}}$. Post-correction was limited by the parasitic cavities within the fiber required for optical read-out of the harmonic oscillator displacement and intensity noise fluctuations of the source laser. The results shown within this work are congruent with previous works on atom chip gravimeters, both of which help move towards portable hand-held gravimeter measurement heads capable of sensitive inertial measurement.

Keywords: Gravimetry, Atom Interferometry, Optomechanical Sensors

Zusammenfassung

Das Ausnutzen der Quantennatur von Atomen durch die Verwendung von Materiewelleninterferometrie hat zur Entwicklung von Geräten geführt, die empfindlich auf die lokale Gravitationsbeschleunigung reagieren. Messungen der Gravitationsbeschleunigung sind anwendbar in Bereichen von der Detektion unterirdischer Dichteunterschiede bis hin zur Beobachtung allgemeinrelativistischer Effekte. Lichtpulsatominterferometer liefern eine absolute Messung der Gravitationsbeschleunigung mit einer Sensitivität, die der Leistung klassischer Sensoren Konkurrenz macht und diese sogar übertrifft. Die Vorteile von Atominterferometern als inertielle Messgeräte haben zu Bestrebungen geführt, die Sensitivität der Messköpfe zu erhöhen und ihre räumlichen Abmessungen zu verringern, wodurch sie im Feldeinsatz einfacher zu transportieren sind. Mit steigender Sensitivität wird es anspruchsvoller, die Beschränkungen durch Rauschquellen in der Messung zu berücksichtigen, insbesondere den Einfluss der Bodenbewegung auf Messungen. Vibrationen, die an die Inertialreferenz koppeln, verursachen eine in den Interferometerpfaden unterschiedliche, zeitlich veränderliche Phasenverschiebung. Diese Einschränkung ist besonders in transportablen Atomgravimetern im Feldeinsatz relevant, da dort das Inertialrauschen üblicherweise weitaus höher ist als in relativ ruhigen Laborumgebungen.

Im Rahmen dieser Arbeit wird die Implementierung und Demonstration der Nachkorrektur von Inertialrauschen in einem Atominterferometer in Umgebungen mit geringem Inertialrauschen und simulierten stark bewegten Umgebungen gezeigt. Für ein Atominterferometer mit hoher Pulsseparationszeit ($T = 78$ ms) ergab die Nachkorrektur eine Erhöhung der Kurzzeitstabilität von $4.4 \times 10^{-6} \text{ m/s}^2/\sqrt{\text{Hz}}$ auf $9.2 \times 10^{-7} \text{ m/s}^2/\sqrt{\text{Hz}}$. Diese Methode wurde mit einem anderen Bewegungssensor reproduziert, um die Nachkorrektur in einer stark bewegten Umgebung durchzuführen, die durch zusätzliche Bewegung der Inertialreferenz erzeugt wurde. In der Durchführung der Nachkorrektur in dieser stark bewegten Umgebung konnten wir einen Anstieg der Kurzzeitstabilität von $\gamma = 73,8$ zeigen. Die derzeitigen Limitierungen der Nachkorrektur resultierten aus der beschränkten Auflösung des Eigenrauschens und des Spektrums. Über die Korrekturen mit kommerziell verfügbaren Sensoren hinaus, demonstriert diese Arbeit zum ersten Mal die Nachkorrektur mit einem kompakten optomechanischen Sensor der nächsten Generation. Dieser optomechanische Sensor besteht aus monolithischem Quarzglas, das empfindlich Beschleunigungen einer harmonisch oszillierenden Testmasse messen kann, indem es optisch ausgelesen wird. Dieser neuartige Bewegungssensor hat gegenüber allen zuvor gezeigten Sensoren den Vorteil, dass es vakuumkompatibel und insensitiv auf Magnetfelder ist und das Potential besitzt, direkt in der inertialen Referenz implementiert zu werden. In dieser Arbeit wird die Nachkorrektur von Inertialrauschen in einer simulierten stark bewegten Umgebung demonstriert, die die Kurzzeitstabilität von $8 \times 10^{-3} \text{ m/s}^2/\sqrt{\text{Hz}}$ auf $5 \times 10^{-4} \text{ m/s}^2/\sqrt{\text{Hz}}$ bringt. Die Nachkorrektur war beschränkt durch parasitäre Resonatoren innerhalb der Faser, die für das optische Auslesen der Auslenkung des harmonischen Oszillators benötigt wird, und durch Fluktuation im Intensitätsrauschen der Laserquelle. Die in dieser Arbeit gezeigten Ergebnisse sind kongruent mit vorigen Arbeiten an Atomchipgravimetern, da beide auf portable, tragbare Gravimeter-Messköpfe hinarbeiten, die empfindliche Inertialmessungen durchführen können.

Stichworte: Gravimetrie, Atominterferometry, Optomechanische Sensoren

Acknowledgement

I would like to first and foremost thank my family for supporting me throughout my education. My mom Jennifer Richardson for sacrificing so much to raise us through the hard times, and to James Richardson who took us in and raised us with extreme selflessness. I would like to thank my brother Drake Richardson, and my grandmother Marcia Smith for supporting us. I would like to thank my best friend and partner Freya.

I would like to acknowledge Ernst Rasel for supporting me through the PhD, and Dennis Schlipfert for the endless guidance. I would like to thank Henning Albers, Dipankar Nath, Jonas Hartwig and Ashwin Rajagopalan for help within the laboratory and making a great working environment. I would like to thank Christian Schubert, Waldemar Herr, Sven Abend, Sebastian Bode, Holger Ahlers, Naceur Gaaloul, Dennis Becker, Torben Schulze, Dorothee Tell, Étienne Wodey, Klaus Zipfel, Manuel Popp, Maral Sahelgozin, Baptist Piest, Christian Meiners, Jonas Matthias, Maike Lachmann, Matthias Gerseemann, and Kai Frye for the many years of advice, discussion and help. Lastly I would like to thank Felipe Guzmán and Lee Kumanchik for providing the optomechanical sensor, and guidance with their usage.

Contents

1	Introduction	8
1.1	Measuring the Local Gravitational Acceleration	8
1.2	Atom Interferometry for Measuring Accelerations	10
1.3	Opto-mechanically Enhanced Atom Interferometry	12
1.4	The Goal of this Work	13
1.5	Organization of this Thesis	14
2	Atom Interferometry	16
2.1	Atom Interferometry	16
2.1.1	The Two Level System	16
2.1.2	Stimulated RAMAN Transitions	19
2.2	The Mach-Zehnder Atom Interferometer	20
2.2.1	Sensitivity Formalism	21
3	Gravimetry with the 22 cm Prototype	24
3.1	Experimental Setup	24
3.1.1	Vacuum chamber	25
3.1.2	Laser System	28
3.2	Experimental Sequence	32
3.2.1	Cooling and Trapping	32
3.2.2	State Preparation	33
3.2.3	Raman Transitions	34
3.2.4	Interferometry	36
3.3	Detection and Evaluation of data	36
3.3.1	Measuring the Gravitational Acceleration	37
3.3.2	Momentum Reversal	39
4	Inertial Noise and Post-Correction	40
4.1	Introduction	40
4.1.1	Sources of Inertial Noise	41
4.2	How Vibrations affect the Atom Interferometer	42
4.2.1	Frequency Dependence of the Atom Interferometer to Vibrations	43
4.3	Inertial Noise Mitigation in Atom Interferometers	45

4.3.1	Vibration Attenuation	45
4.3.2	Vibration Post correction	45
5	Sensor Post-correction	48
5.1	Post-correction Algorithm	48
5.1.1	Sensor Preparation	49
5.1.2	Acquisition of Ground Motion	50
5.1.3	Sensor Response	51
5.1.4	Filtering	51
5.1.5	Signal Delay Correction	52
5.1.6	Fringe Reconstruction	53
5.2	Atom Interferometer Response and Fitting	54
5.2.1	Evaluation of Post-Correction	54
5 A	Inertial Noise Post-Correction with Commercially Available Sensors	56
5 A.1	Measurements of Post-Correction Performance	56
5 A.1.1	Post-Correction in Low Inertial Noise Environments	56
5 A.1.2	Post-Correction in a Simulated High Motion Environments	57
5 A.2	Limitations to Gravimetry	60
5 A.2.1	Self Noise and Spectral Noise Limitation	61
5 A.2.2	Alignment Noise of the Sensor	64
5 A.2.3	Raman Phase lock loop	65
5 A.2.4	Synchronous Noise Due to Magnetic Field Sensitivity	65
5 A.2.5	The Mechanical Transfer Function	67
5B	Opto-mechanical resonator enhanced atom interferometry	68
5B.1	Inertial Sensing with an opto-mechanical resonator	68
5B.2	OMIS Theory	69
5B.3	Experimental Setup	71
5B.4	Sensor Specifications	72
5B.4.1	OMIS Generator Constant	75
5B.5	Results from Hybridization with the Optical Resonator	75
5B.5.1	Optical Resonator post-correction in High motion Environments	75
5B.5.2	Long Term Stability of Hybridization with the Optical Resonator	77
5B.5.3	Comparison of Titan and OMIS	79
5B.6	OMIS Post Correction Limitations	80
5B.6.1	Frequency Noise	80
5B.6.2	Intensity Noise	81
5B.6.3	Parasitic Cavities and Fiber Noise	82
5B.6.4	Mechanically Induced Transmission Loss	86
5B.6.5	Thermal Limitation	87
5B.6.6	Combined Noise Sources	87

6 Conclusion	88
6.1 Improvements in the Post-Correction method	89
6.2 Improvements to Post-Correction with the OMIS	89
6.3 Outlook with Future Sensors	92
A Sensors	96
A.1 Motion Sensing	96
A.1.1 Simple Harmonic Oscillator Model	96
A.1.2 Frequency Response	98

Chapter 1

Introduction

The property of inertia inherent to matter-waves paired with available optical tools capable of addressing their quantum states have made atom interferometers some of the most sensitive and versatile inertial measurement devices built to date [1]. Ultra-cold atoms provide a repeatable test mass that allows measurement of a variety of phenomena such as accelerations [2, 3, 4], rotations [5, 6, 7], gravitational gradients [8, 9] and, potentially, gravitational waves [10]. Atom interferometry has been used for fundamental tests such as the universality of free fall [11, 12, 13], measurements of the NEWTONIAN gravitational constant [14], and the fine structure constant [15, 16]. The techniques required to reach sensitivities capable of testing fundamental physics have many applications outside of fundamental physics, and have the capability to make a large impacts on modern issues facing society.

An example of a potential application of atom interferometry is seen in the water scarcity crisis in developing nations. The *United Nations Development Programme* estimates that 1.2 billion people in the world do not have access to clean drinking water [17]. In the developing world, access and monitoring of groundwater resources has remained un-utilized [18]. The amount of water in a given water table is dynamic and has a different density than it's surrounding soil, rock and limestone. These changes would correspond to a minute difference in the gravitational acceleration above the surface, creating a geoid that varies spatially and temporally. Tracking and measuring these small changes of the gravitational acceleration could help determine the location of water, map the geography of a water table to prevent pollutants from entering an aquifer, and monitor the current amount of water in a given region over time for water resource management. The process of measuring the gravitational acceleration in this manner is known as **gravimetry**. Outside of water resource detection the act of measuring the local gravitational acceleration has applications in geology, vulcanology [19], archaeology [20, 21], resource detection [22], navigation [23] and civil engineering [24].

1.1 Measuring the Local Gravitational Acceleration

Gravitational acceleration can be described from a general relativistic perspective as an attribute of space time curvature [25, 26]. However, for measurements within the local inertial reference frame

of the Earth, we can reduce the complexity of the full gravitational acceleration to a NEWTONIAN frame [27]. In this perspective we can describe the local gravitational acceleration at a given point on the Earth’s surface as equation 1.1.

$$\vec{g} = -\frac{GM_{\oplus}}{r^2}\hat{r} \quad (1.1)$$

Where, \vec{g} is the local gravitational acceleration, G is the NEWTONIAN gravitational constant, M_{\oplus} is the mass of the Earth, and r is the distance between the center of mass of the Earth and the measurement point.

Gravimeters

A gravimeter is a device capable of measuring the gravitational acceleration at a given point. Gravimeters can be divided into two types of sensor, **absolute gravimeters** and **relative gravimeters**:

- **Relative gravimeters** - These devices employ a test mass with a restoring force device, such as a spring or electromagnetic field. The force of gravity is in equilibrium with the restoring force, and therefore small test mass displacement corresponds to a small change in acceleration. However, these restoring force devices are prone to temperature changes and other effects, and therefore the signal measured corresponding to the same acceleration will change over time, leading to measurement drifts. This is the operating principle behind devices such as the super conducting gravimeter, spring gravimeters; or used within this work the Titan and OMIS.
- **Absolute gravimeters** - These devices observe the local gravitational acceleration by measuring the acceleration of a test mass in free fall. This type of measurement may not be as sensitive as relative gravimeters, but in general is stable over long periods of time. Absolute gravimeters require device ‘dead-time’: time between measurements where the test mass is prepared, enters free fall and detection is performed; however this can be addressed through the use of interleaved measurements, or use of multiple sensors. Atom interferometers and the FG-5 are absolute gravimeters.

Table 1.1: List of gravimeters presently operating. *Atom interferometers have been grouped together in this table, a full list of current atom gravimeters can be found in table 1.2.

Sensor	Sensor Type	Sensitivity	Drift
FG5 [28]	Absolute	150 nm/s ² /√Hz	—
Atom Interferometers*	Absolute	42 nm/s ² /√Hz	—
Spring Gravimeter [29]	Relative	50 nm/s ² /√Hz	2000 nm s ⁻² d ⁻¹
MEMS [30]	Relative	400 nm/s ² /√Hz	1500 nm s ⁻² d ⁻¹
Super Conducting Gravimeter [31]	Relative	1 nm/s ² /√Hz	0.1 nm s ⁻² d ⁻¹
OMIS [32]	Relative	98.1 nm/s ² /√Hz	System Dependent ¹

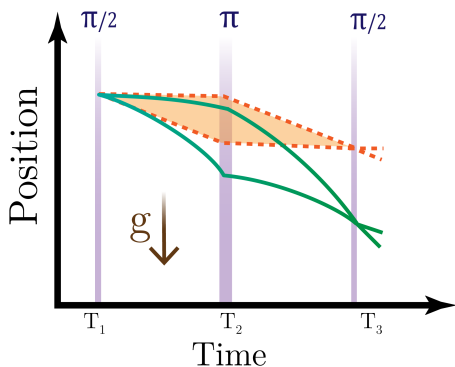
¹The drift of the OMIS is primarily determined by the optical read-out system. This will be discussed further in section 5B.6.

The drift and calibration requirements of relative gravimeters are not suitable for measurements occurring over large timescales, such as long period oscillation measurements. Additionally applications these sensors are not suitable for environments where calibration is not easily achieved, for example a deep borehole gravimeter with remote access.

For these types of applications, long-term stable absolute gravimeters present a better option; however, not all absolute gravimeters present an acceptable solution. For example, the FG-5[28, 33], utilizes a falling corner cube to measure test mass position using a MICHELSON-MORLEY optical interferometer. The FG-5's test mass is a moving mechanical part and prone to fatigue, requiring calibration after a given number of measurements. Additionally sensitive mechanical components within the device have low clipping levels and are not suitable for high-noise environments such as a sounding rocket, sea-faring vessel or aircraft. However, atom interferometry stemming from the wider field of matter-wave interferometry presents a robust and dynamic solution for absolute gravimetry.

1.2 Atom Interferometry for Measuring Accelerations

The first measurement [34, 35] of gravitational effects using matter-wave interferometry was performed with thermal neutrons which were spatially separated paths into two distinct paths. The relative height and therefore gravitational potential between the two paths could be varied. By interfering these two paths, one could measure the gravitationally induced phase shift at the output of the interferometer as a function of relative gravitational potential between the two paths.



With the development of techniques for cooling and optical manipulation of the quantum state² of atoms the ability to measure gravitational effects was extended to atoms [38, 39, 40]. Measurements of the gravitational acceleration are obtained by cooling and trapping cold atoms, allowing them to enter free fall and manipulating their quantum state in an interferometer configuration. By detecting the phase difference between the two paths of the interferometer, we can obtain the acceleration experienced by the atoms.

At the heart of measurement is the light-pulse atom interferometer. In a broad sense, we can think of a light-pulse atom interferometer as the analog to a classical light interferometer, but with the role of light and atoms reversed.

By controlling the pulse duration, beam intensity, and detuning from resonance, we can realize the atom optics equivalent of beam-splitters ($\frac{\pi}{2}$ pulses) and mirrors (π pulses). One major difference in this analogy is that atoms couple much stronger to gravitation than light does, something that is exploited in inertial measurements.

In principle, atom interferometers are sensitive to any acceleration experienced by the atoms which act as the test mass. We can design the experiment to measure the effect that we are

²Atom interferometry is also possible with gratings [36, 37], but due to the flexibility optical pulses provide, this work will focus solely on light-pulse atom interferometry.

interested in. For example, in the case of an atom gravimeter, we reduce transverse motion and align the interferometry axis to the axis of gravitational acceleration \hat{g} .

The field of measuring gravitational acceleration with atom interferometers is actively under development and atom gravimeters have been demonstrated with a variety of sensitivities, cycle times and physical dimensions (see table 1.2); a fact that determines the applicability to a given measurement scenario. Various methods for improving the sensitivity of atom interferometers includes increasing the baseline [41], increasing the momentum transfer [42], and exploiting quantum properties of the atoms, such as squeezing [43].

Outside of increasing the sensitivity of atom interferometers, there is an active push towards reducing the physical dimensions of atom interferometers making these devices more portable. Experiments such as GAIN [4], the Cold Atom Gravimeter [2], Muquan’s Absolute Quantum Gravimeter [3], and the currently in development QG-1 are transportable, yet still possess physical dimensions that may limit the location of measurements the bounds of modern infrastructure. To address this, an ultimate goal to reach would be a ‘gravity in hand sensor’, a sensor-head that can be held within a hand, with a backpack size optical system. Such a device would be capable of performing sensitive measurements of the gravitational acceleration in spaces currently not reachable with current devices, yielding applications for ground water detection in remote locations not accessible by truck, or in space-borne craft where the size of a measurement device is critical. To reach this goal, we need to address the current limitations to gravimetry with cold atoms.

Group	Sensitivity	T_c	T	Comments
Wuhan [44]	42 nm/s ² /√Hz	1 s	300 ms	Active vibration stabilization (Guralp CMG3ESP).
SYRTE [2]	54 nm/s ² /√Hz	500 ms	80 ms	Correlation with Guralp CMG-3T.
GAIN [4]	96 nm/s ² /√Hz	1.2 s	260 ms	Active Stabilization and post-correction.
MuQuans [3, 45]	500 nm/s ² /√Hz	500 ms	58 ms	Post-correction - sensor not officially stated.
ANU [46]	600 nm/s ² /√Hz	Not Stated	60 ms	GAS vibration isolation.
This Work	923 nm/s ² /√Hz	2.3 s	78 ms	Post-correction with sensors.
Berkeley [47]	6 μm/s ² /√Hz	2 s	78 ms	Multi-axis, no seismic post-correction published
VLBAI* [41]	0.33 nm/s ² /√Hz	11 s	1 s	GAS vibration isolation, post-correction with Trillium 240
QG-1*	14 nm/s ² /√Hz	2 second	300 ms	Post-correction with Titan

Table 1.2: Where T_c is the cycle time and T is the pulse separation time. * Under development, projected number.

As with any measurement device, atom interferometers are sensitive to a device specific set of parameters that contribute to measurement uncertainty. For atom interferometers this can be generated from, for example, time varying magnetic field gradients, optical power fluctuations, or ground motion.

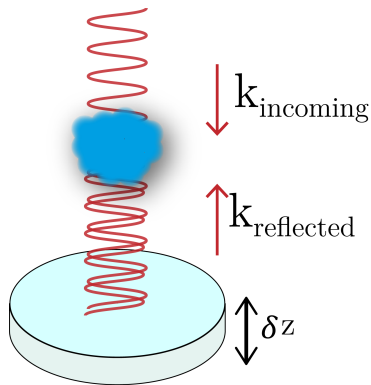


Figure 1.1: In this experiment accelerations of the retro-reflection mirror used for interferometry pulses present a frequency dependent acceleration noise that enters as noise in the measurement of the DC gravitational acceleration.

Ground motion when compared to other noise sources, is a major limitation to improving the sensitivity of atom gravimetry measurements, especially for field deployable gravimeters. This motion couples into the atom interferometer inertial reference and affects the relative phase difference between the incoming and retro-reflected light required for addressing the atoms. This phase shift cannot be discerned from the gravitational acceleration of the test mass. The effect generated from these vibrations is given the name **inertial noise**, also known as parasitic vibration noise, figure 1.1.

By measuring the frequency dependent motion of the inertial reference over the course of a measurement cycle using a motion sensor, it is possible to calculate the inertial noise experienced by the atom interferometer and distin-

guish the DC gravitational acceleration signal from the AC ground motion. This method can be applied over multiple measurement cycles to extract the gravitational acceleration in a noisy environment. If the effectiveness of the post-correction surpasses the intrinsic measurement limitations of the atom interferometer (such as the detection noise), then it is possible to eliminate the contribution from inertial noise in an arbitrarily noisy environment. This would allow for atom interferometers that could be placed directly at points of interest without the need for vibration isolation, which is large and hinders miniaturization efforts. Extending this principle, this would allow for placement of sensors on drones for aerial gravimetry, use in pipe detection for street construction, or on submersible craft for use of measurements of water density.

1.3 Opto-mechanically Enhanced Atom Interferometry

Inertial noise post-correction has been demonstrated with commercially available sensors [48, 49, 50]. However, these sensors are highly sensitive to magnetic fields, pressure and temperature changes. These traits limit the ability of commercial motion sensors to accurately measure the motion occurring during a measurement cycle. Additionally the large physical dimension of commercial motion sensors relative to the inertial reference creates a dynamic transfer function between the motion occurring on the inertial reference, and the signal measured by the motion sensor; further limiting the ability of these sensors to post-correct inertial noise.

Recent developments in optomechanics have lead to the creation of a small sensor capable of accurately measuring motion [51, 32, 52]. The optomechanical inertial sensor (OMIS) (figure 1.2) is comprised of a harmonic oscillator test mass supported by two flexures connected to a rigid body, where small displacements of the test mass can be optically read out. The entire sensor is constructed from one monolithic piece of fused silica. The device is much smaller in comparison to traditional accelerometers, magnetic field insensitive, and suitable for measurements within vacuum. Additionally these devices have the prospect to be placed directly into the inertial reference, such as retro-reflection mirror or atom chip, reducing the effect of dynamic transfer functions. These properties make the optomechanical sensor an ideal candidate as a replacement to traditional commercially available motion sensors for use in inertial noise post-correction.

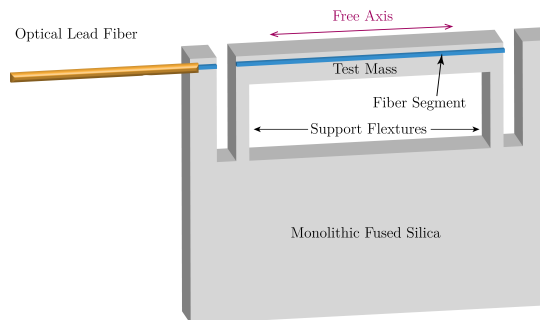


Figure 1.2: The optomechanical inertial sensor (OMIS). The advantages of this device surpass the applicability of commercial sensors to post-correction.

1.4 The Goal of this Work

Inertial noise post-correction is an integral part of performing measurements of the gravitational acceleration with light-pulse atom interferometers, especially in high-inertial noise environments. For that reason the work of this thesis has set out to address two primary objectives:

1. To implement vibration post-correction, determining which factors impact the ability to reduce the contribution from inertial noise, effectively reducing the short term uncertainty in measurements of the gravitational acceleration that can be obtained with atom interferometry. This includes evaluating different sensor types, with various self noises and sensitivity to environmental effects in different inertial noise environments, something not fully addressed in previous works on the subject [48, 49, 53].
2. To evaluate the applicability, performance and limitations of the OMIS as a replacement for commercially available motion sensors for use in inertial noise post-correction. To increase the number of environments where atom gravimetry can be performed it is not enough to simply reduce the effects of inertial noise, but also reduce the size of the systems required to do so. Additional benefits such as magnetic field insensitivity, vacuum compatibility and the prospect to directly integrate into the inertial reference make the OMIS an ideal candidate for motion sensing. This is especially critical when considering ongoing developments in transportable atom interferometers, or space-borne missions such as BECCAL.

To achieve these goals, an operating atom interferometer was used. The experiment used in this work was designed for quantum tests of the universality of free fall between ^{39}K and ^{87}Rb [11]. This experiment makes an ideal test-bed for inertial noise post-correction, as atom gravimetry with ^{87}Rb

is established and the reference mirror is easily accessible, allowing for easy integration of different motion sensors.

1.5 Organization of this Thesis

The initial chapters of this thesis work will focus on how measurements of the gravitational acceleration are possible with atom interferometers. **Chapter 2- Atom Interferometry** outlines the theoretical framework used within this thesis, establishing the light-matter interactions that allow for atom interferometry to be possible. **Chapter 3 - Gravimetry** focuses on the specific experimental apparatus used for measurements within this work, as well as the method for obtaining the local gravitational acceleration with a light-pulse atom interferometer.

From here, the work will begin to focus on how vibrations creates a noise source limitation to gravimetry, what can be done to address it, and the results from doing so. **Chapter 4 Inertial Noise Post-Correction** discusses how vibrations enter into a measurement of the gravitational acceleration, what strategies can be employed to mitigate this noise source. **Chapter 5 - Post-Correction Results** is prefaced by the inertial noise post-correction method used within this experiment, then broken into two sub-chapters: **Chapter 5A** focuses on post-correction with commercially available sensors as well as the limitations, and **Chapter 5B** focuses on how the optomechanical resonator can obtain inertial reference motion, perform inertial noise post-correction and the current limitations of the device.

Lastly **Chapter 6 - Outlook** will discuss the results obtained within this thesis work, what is required for improved results, and extrapolation of what is possible in future experiments.

:

Chapter 2

Atom Interferometry

2.1 Atom Interferometry

By utilizing the matter-wave nature of cold atoms we can experimentally measure inertial phenomena such as acceleration and rotations. In this work, we use alkali atoms, specifically ^{87}Rb . Alkali atoms have the benefit of having one free valence electron, which allows us to work in a hydrogen-like system with minimal interactions with the other shell electrons. Here, we will focus on measurements of gravitational acceleration, \vec{g} . This is performed by using timed optical pulses to perform atom interferometry which measure the acceleration of our test mass atoms in free fall. In our experiment, we realize these pulses with stimulated RAMAN transitions between the states $|F = 1, m_f = 0\rangle$ and $|F = 2, m_f = 0\rangle$. By addressing the inertially sensitive transitions of the accelerating test mass, we can create a MACH-ZEHNDER atom interferometer where the phase shift at the output of the interferometer is dependent on the local gravitational acceleration. This section will cover the underlying principles of atom interferometry that are required to perform these inertial measurements.

2.1.1 The Two Level System

Manipulation of the ensemble of atoms requires the use of coherent light. To model how coherent light affects our atomic ensemble, we can model our atomic system as a 2 level system with a ground and excited state, interacting with an electromagnetic field. In this two state picture, we have our two states: a ground state $|1\rangle$ with energy $E_1 = \hbar\omega_1 = 0$ and excited state $|2\rangle$ with $E_2 = \hbar\omega_2$. The complete unperturbed two level system can be described by the state vector, equation 2.1.

$$\Psi(r, t) = C_1 |1\rangle e^{-i\omega_1 t} + C_2 |2\rangle e^{-i\omega_2 t} \quad (2.1)$$

Under the condition $|C_1|^2 + |C_2|^2 = 1$ and $\frac{dC_n}{dt} = 0$.

The HAMILTONIAN of this system can be written as, equation 2.2.

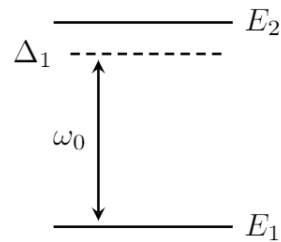


Figure 2.1: The Two level system: A ground state with energy $E_1 = \hbar\omega_1$ and an excited state with energy $E_2 = \hbar\omega_2$. An external electromagnetic field with frequency ω_0 detuned by Δ interacts with the 2 level system.

$$\hat{H}_0 = -\frac{\hbar^2}{2m}\hat{P}_0^2 + V(r) \quad (2.2)$$

Where m is the particle mass, $V(r)$ is the external potential and $\hat{P} = i\frac{\partial}{\partial r}|r\rangle$ the momentum operator, both of which are in the position representation.

In the presence of a dynamic external field the HAMILTONIAN is, equation 2.3.

$$\hat{H}(r, t) = -\frac{\hbar^2}{2m} = [\hat{P}_0 + eA(r, t)]^2 - e\Phi(r, t) + V(r) \quad (2.3)$$

Here, $A(r, t)$ is the vector potential and $\Phi(r, t)$ is the scalar potential of the external field. Under the assumption that the external field is light with wavelength in the optical region, we can reduce the HAMILTONIAN using the dipole approximation [54], equation 2.4.

$$\hat{H} = -\frac{\hbar^2}{2m}\hat{P}^2 + V(r) + e\hat{r} \cdot \vec{E}(t) \quad (2.4)$$

Where e is the electric charge, $\vec{d} \equiv e\hat{r}$ and $\vec{E}(t)$ is the time dependent electric field, equation 2.5.

$$\vec{E}(t) = E_0 \cos(\omega_0 t) \hat{e} \quad (2.5)$$

\hat{e} is the polarization vector, and ω_0 is the angular frequency of the driving electromagnetic field. The HAMILTONIAN can be recast in terms a time dependent perturbation, equation 2.6.

$$\hat{H} = \hat{H}_0 + W(t) \quad (2.6)$$

Where $W(t) = -\vec{d} \cdot \vec{E}(t)$.

To describe how this system evolves in time, we can use the time dependent SCHRÖDINGER equation, equation 2.7.

$$i\hbar \frac{\partial |\Psi\rangle}{\partial t} = \hat{H} |\Psi\rangle \quad (2.7)$$

Which in the matrix representation gives us equation 2.8.

$$i\hbar \begin{bmatrix} \dot{C}_1(t) \\ \dot{C}_2(t) \end{bmatrix} = \hbar \begin{bmatrix} 0 & -\frac{\Omega_0}{2}(e^{-i\omega_0 t} + e^{i\omega_0 t}) \\ -\frac{\Omega_0}{2}(e^{i\omega_0 t} + e^{-i\omega_0 t}) & \omega_2 \end{bmatrix} \begin{bmatrix} C_1(t) \\ C_2(t) \end{bmatrix} \quad (2.8)$$

Where

$$\Omega_0 \equiv \frac{\vec{d} \cdot \hat{e} E_0}{\hbar}.$$

From equation 2.8, we get the coupled equations 2.10.

$$i\dot{C}_1(t) = -\frac{1}{2}\Omega_0(e^{-i\omega_0 t} + e^{i\omega_0 t})C_2(t) \quad (2.9)$$

$$i\dot{C}_2(t) = \omega_2 C_2 - \frac{1}{2}\Omega_0(e^{-i\omega_0 t} + e^{i\omega_0 t})C_1(t) \quad (2.10)$$

Trying the solution $C_1(t) = C_1(t)$ and $C_2(t) = C_2(t)e^{-i\omega_0 t}$ and using the rotating wave approximation (terms $e^{\pm 2i\omega_0 t}$ terms average to 0), we get equations 2.11 and 2.12.

$$i\dot{C}_1 = -\frac{\Omega_0}{2}C_2 \quad (2.11)$$

$$i\dot{C}_2 = -\Delta C_2 - \frac{\Omega_0}{2}C_1 \quad (2.12)$$

Where $\Delta = \omega_2 - \omega_0$. For the two-level system, this can be solved exactly, equations 2.13 and 2.14.

$$C_1(t) = \left[\cos \frac{\Omega t}{2} - \frac{i\Delta}{\Omega} \sin \left(\frac{\Omega t}{2} \right) \right] e^{\frac{i\Delta t}{2}} \quad (2.13)$$

$$C_2(t) = \left[\frac{i\Omega_0}{\Omega} \sin \left(\frac{\Omega t}{2} \right) \right] e^{\frac{i\Delta t}{2}} \quad (2.14)$$

Where $\Omega = \sqrt{|\Omega_0|^2 + \Delta^2}$ known as the RABI frequency.

If we start in the ground state, $C_1(0) = 1$, the probability of finding the system in state $|2\rangle$ as a function of time is given by equation 2.15.

$$|C_2(t)|^2 = P_{1 \rightarrow 2}(t) = \frac{|\Omega_0|^2}{\Omega^2} \sin^2 \left(\frac{\Omega t}{2} \right) \quad (2.15)$$

From eq. 2.15 it is clear that for a given detuning, Δ , optical power Ω_0 , and pulse time τ , we can transfer atoms between states $|1\rangle$ and $|2\rangle$. In practice this is performed by utilizing pulses of light with a detuning that can be approximated ¹ as fixed. With these pulses, we can vary the temporal length to transfer atoms from one state to another. For shorthand, we can abbreviate pulses as:

π Pulse: For an atom starting in the state $|1\rangle$, a pulse with length $\tau = \pi/\Omega$ will transfer the atom completely to state $|2\rangle$. In a two level system, the π pulse will flip or 'reflect' the initial atomic state.

$\pi/2$ Pulse: For an atom starting in $|1\rangle$, a pulse with length $\tau = \pi/2\Omega$ will transfer the atom into an a superposition of internal states $\Psi(t) = \frac{1}{\sqrt{2}}[|1\rangle + |2\rangle]$.

¹In our experiment we linearly sweep the RAMAN detuning to address the DOPPLER shifted ensemble as it accelerates in free fall. This change in frequency is minor relative to the total detuning.

2.1.2 Stimulated Raman Transitions

To build an atom interferometer, we are interested in performing interferometry between long-lived magnetically insensitive states of alkali atoms. In theory, single photon transitions are possible, but in accordance with selection rules, optical transitions from one magnetically insensitive ($m_f = 0$) state to another are highly suppressed.

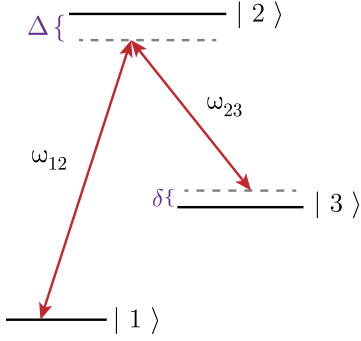


Figure 2.2: For a 2 photon process, 1 photon with driving frequency ω_{12} couples states $|1\rangle$ to $|2\rangle$ with detuning Δ , a second photon with driving frequency ω_{23} couples state $|2\rangle$ to $|3\rangle$ with detuning δ .

To circumvent this, we can use 2-photon transitions, such as stimulated RAMAN transitions. Stimulated RAMAN transitions allow us to coherently transition between long lived hyperfine ground states of an alkali atom by using 2 detuned optical beams.

To model stimulated RAMAN transitions, we can extend the above two level single photon calculations to a 3-level 2 photon process. To start, we can model the 2 photon driving field as equation 2.16.

$$E(t) = E_1 \cos(\omega_{12}t + \phi)\hat{e}_1 + E_2 \cos(\omega_{23}t + \phi)\hat{e}_2 \quad (2.16)$$

with driving frequencies, ω_{13} and ω_{23} . The perturbation term of the HAMILTONIAN then becomes equation 2.17.

$$H'(t) = \hbar\omega_{12} |1\rangle\langle 3| + \hbar\omega_{23} |3\rangle\langle 2| \quad (2.17)$$

The total equation can be reduced to the same form as 2.15, equation 2.18.

$$|C_2(t)|^2 = P_{1 \rightarrow 2}(t) = \frac{|\Omega_0|^2}{\Omega_{\text{eff}}^2} \sin\left(\frac{\Omega_{\text{eff}}t}{2}\right) \quad (2.18)$$

Where,

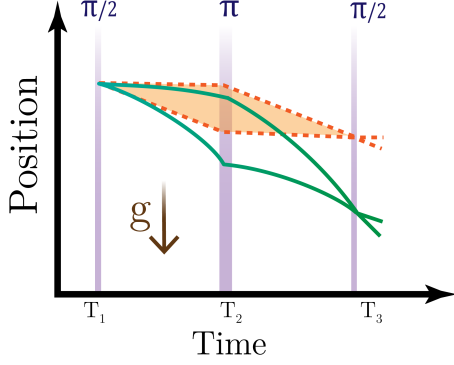
$$\Omega_{\text{eff}} = \frac{\Omega_1\Omega_2^*}{2\Delta\hbar} = \frac{\langle 1|\vec{E}(t) \cdot \hat{d}|3\rangle\langle 3|\vec{E}(t) \cdot \hat{d}|2\rangle}{2\Delta\hbar} \quad (2.19)$$

This two-photon process couples not only the internal states, but also external momentum states as well. The change in momentum For such a system is: $|1, p_0\rangle$ to the intermediate state $|3\rangle$, and a second photon with ω_{23} couples $|3\rangle$ to $|2, p_0 + \hbar\vec{k}_{\text{eff}}\rangle$. For a pair of counter-propogating beams, the momentum transfer is given by equation 2.20.

$$\Delta\vec{p} = \hbar\vec{k}_{\text{eff}} = \frac{\omega_{12} + \omega_{23}}{c} \quad (2.20)$$

Where c is the speed of light. With stimulated RAMAN transitions it is possible to change the frequency of either ω_{12} or ω_{23} to perform spectroscopy. To take a practical example, in the case of the ^{87}Rb we fix ω_{12} and scan the $|F=1\rangle \rightarrow |F=2\rangle$ transition by changing the frequency of ω_{23} . This process can be applied to accelerating ensembles of atoms in free fall. As the cloud accelerates relative to the inertial reference, the cloud's transitions frequencies will DOPPLER shift.

2.2 The Mach-Zehnder Atom Interferometer



By utilizing RAMAN transitions we can use π and $\pi/2$ pulse to create an inertially sensitive MACH-ZEHNDER atom interferometer. In such an interferometer, an ensemble of atoms enters in a pure state $|F = 1, m_f = 0\rangle$, is split into a superposition of ground and excited state with a $\pi/2$ pulse, the internal states are then exchanged with a π pulse and then recombined with a final $\pi/2$ pulse. Phase differences accumulated between the two paths will result in a phase dependent population of the excited (or ground) state, equation 2.21.

$$P_{|F=2\rangle} = \frac{C_0}{2} [1 + \cos(\Delta\Phi)] \quad (2.21)$$

Where P is the normalized population, and C is the contrast of the interferometer, and $\Delta\Phi$ is the phase difference between the two paths. In practice the final atomic state population is read out by state selective fluorescence detection.

The phase difference $\Delta\Phi$ between the two paths at the output of the interferometer for an ensemble of free falling atoms in a gravitational potential can be calculated using a path integral formulation [55] or by calculating the phase contribution of the pulses [38]. From either method, the phase difference is given by equation 2.22.

$$\Delta\Phi = \underbrace{\vec{k}_{\text{eff}} \cdot \vec{g} T^2}_{\text{Accelerations}} + \underbrace{2\Omega_{\text{rot}}(\vec{v}_0 \times \vec{k}_{\text{eff}})T^2}_{\text{Rotations}} + \underbrace{\Delta\phi_{\text{HO}}}_{\text{Higher order terms}} \quad (2.22)$$

By aligning the Raman interferometry beams parallel to the gravitational acceleration axis and reducing the velocity v_0 along the axis perpendicular to the gravitational acceleration, we can minimize the effect from the rotation term. The higher order terms will be addressed in section 4.

By introducing a frequency sweep on one of the two RAMAN beams, we can scan the output of the atom interferometer, giving us equation 2.23.

$$\Delta\phi = \vec{k}_{\text{eff}} \cdot \left(\vec{g} - \frac{\alpha}{\vec{k}_{\text{eff}}} \right) T^2 \quad (2.23)$$

When a value of the sweep rate $\alpha/\vec{k}_{\text{eff}}$ that matches the gravitational acceleration \vec{g} , the phase difference of $\Delta\phi = 0$ for all values of the pulse separation time T .

2.2.1 Sensitivity Formalism

The sensitivity formalism [49, 56] is a tool for understanding how spatial and temporal phase effects change the output of the atom interferometer, something that will be useful when exploring how vibrations affect the atom interferometer. The sensitivity function is defined as the change in transition probability for a phase jump $\delta\phi$ occurring at a time t , equation 2.24.

$$g(t) = 2 \lim_{\delta\phi \rightarrow 0} \frac{\delta P(\delta\phi, t)}{\delta\phi} \quad (2.24)$$

To calculate the sensitivity function for a MACH-ZEHNDER interferometer we can continue to use the two-state picture, equation 2.25.

$$\begin{bmatrix} C_1(t_f) \\ C_2(t_f) \end{bmatrix} = M \begin{bmatrix} C_1(t_0) \\ C_2(t_0) \end{bmatrix} \quad (2.25)$$

Where M is our total evolution matrix comprised of $\pi/2 - \pi - \pi/2$ pulses, with pulse duration τ and pulse separation time T , equation 2.26.

$$M = \begin{bmatrix} e^{-i\omega_1(t-t_0)} \cos(\frac{\Omega_R}{2}(t-t_0)) & -e^{-i\omega_1(t-t_0)} e^{i(\omega t_0 + \phi)} \sin(\frac{\Omega_R}{2}(t-t_0)) \\ -e^{-i\omega_2(t-t_0)} e^{i(\omega t_0 + \phi)} \sin(\frac{\Omega_R}{2}(t-t_0)) & e^{-i\omega_2(t-t_0)} \cos(\frac{\Omega_R}{2}(t-t_0)) \end{bmatrix} \quad (2.26)$$

We can then use this evolution matrix to calculate the probability of a transition into the C_2 state at a given time t for our atom interferometer. Giving us our sensitivity function $g(t)$. Where $g(t)$ is the velocity representation of the sensitivity function, given as equation 2.27.

$$g(t) = \begin{cases} -\sin(\frac{\Omega_{\text{eff}}}{2}t) & \text{if } 0 < t \leq \tau \\ -1 & \text{if } \tau < t \leq \tau + T \\ -\sin(\frac{\Omega_{\text{eff}}}{2}(t-T)) & \text{if } T + \tau < t \leq 3\tau + T \\ -1 & \text{if } \tau < t \leq 3\tau + T < t \leq 3\tau + 2T \\ -\sin(\frac{\Omega_{\text{eff}}}{2}(t-2T)) & \text{if } 3\tau + 2T < t \leq 4\tau + 2T \\ 0 & \text{Otherwise.} \end{cases} \quad (2.27)$$

By integrating the phase shifts occurring at a specific time during the atom interferometer, we can obtain the total phase shift that occurred, equation 2.28.

$$\Delta\Phi = \int_{-\infty}^{\infty} g(t)d\phi = \int_{-\infty}^{\infty} g(t) \frac{d\phi}{dt} dt \quad (2.28)$$

In the case mirror motion, a phase shift (Chapter 4) is given by $\delta\phi = k_{\text{eff}}\delta z$, where is the \hat{z} axis displacement of the mirror. From equation 2.28, it is clear that $g(t)$ can be used to describe the velocity of mirror motion. To obtain the acceleration sensitivity function $g_a(t)$ we can integrate $g(t)$ giving us equation 2.29.

$$g_a(t) = \begin{cases} \frac{2}{\Omega_{\text{eff}}}(1 - \cos(\frac{\Omega_{\text{eff}}}{2}t)) & \text{if } 0 < t \leq \tau \\ t + \frac{2}{\Omega_{\text{eff}}} - \tau & \text{if } \tau < t \leq \tau + T \\ T + \frac{2}{\Omega_{\text{eff}}}(1 - \cos(\frac{\Omega_{\text{eff}}}{2}(t - T))) & \text{if } T + \tau < t \leq 3\tau + T \\ 2T + \frac{2}{\Omega_{\text{eff}}} + 3\tau - t & \text{if } T + 3\tau < t \leq 3\tau + 2T \\ \frac{2}{\Omega_{\text{eff}}}(1 - \cos(\frac{\Omega_{\text{eff}}}{2}(t - 2T))) & \text{if } 3\tau + 2T < t \leq 4\tau + 2T \\ 0 & \text{Otherwise.} \end{cases} \quad (2.29)$$

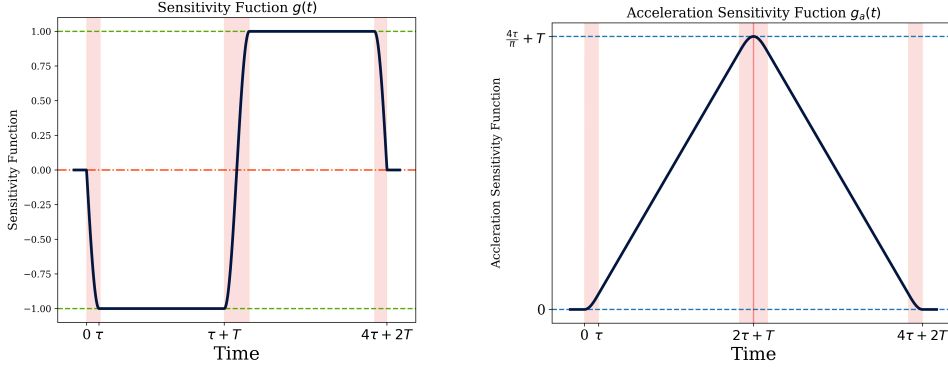


Figure 2.3: (left) The sensitivity functions $g(t)$ of the MACH-ZEHNDER atom interferometer. (right) The acceleration sensitivity function $g_a(t)$.

Chapter 3

Gravimetry with the 22 cm Prototype

In this section we will discuss how measurements of the gravitational acceleration are possible with this specific experiment. As mentioned in the introduction, this experiment is designed to test the universality of free fall with test masses ^{87}Rb and ^{39}K ¹, however this work will focus solely on measurements of the gravitational acceleration performed with ^{87}Rb .

Gravimetry with ^{87}Rb in this experiment starts by heating a sample of rubidium to sublimation. From vapor the atoms are cooled and trapped using a 2D-3D magneto-optical trap (MOT) system [58]. The use of a 2D MOT [59, 60] lowers the time between measurements by reducing the loading time of the 3D MOT. All coherent light used for cooling and interferometry is generated from ECDLs. This light is amplified by tapered amplifiers and coupled into fibers that connect to collimators used to facilitate the magneto-optical trap. After cooling and trapping, the atoms are released and enter free fall. The ^{87}Rb atoms then are cooled below the DOPPLER limit [54], and prepared into the $|F = 1, m_f = 0\rangle$ sub-state. Three stimulated two-photon RAMAN pulses coherently transfer atoms between the $|F = 1\rangle$ and $|F = 2\rangle$ states of the ensemble in a $\pi/2 - \pi - \pi/2$ configuration. The final state of the atom is read out using state-selective fluorescence detection. This process is repeated and the data is evaluated, from which a measurement of the gravitational acceleration is obtained.

In this chapter we will cover a basic overview of the experimental methods required to perform gravimetry with this experiment. This chapter is broken in to three sections, firstly the **experimental setup** which covers the optical and mechanical elements that comprise this experiment. The second section will cover the **experiment sequence** and the last section covers **interferometry**.

3.1 Experimental Setup

Atom interferometry is performed in a vacuum chamber, referred to as the ‘main science chamber’. The mechanical structure of the science chamber can be broken into three interconnected parts: the

¹Although the total experiment shares optics with ^{39}K , for the purposes of simplicity the potassium system will be excluded from this work. For a detailed overview of the potassium system see [57]

2D MOT chamber (with attached oven), the 3D MOT chamber and the free-fall tube with attached detection region; all three of which are supported by an optical table.

A second optical table contains all lasers, amplifiers and locking systems required to perform interferometer. This optical table is connected to the main science chamber via fiber-optics.

3.1.1 Vacuum chamber

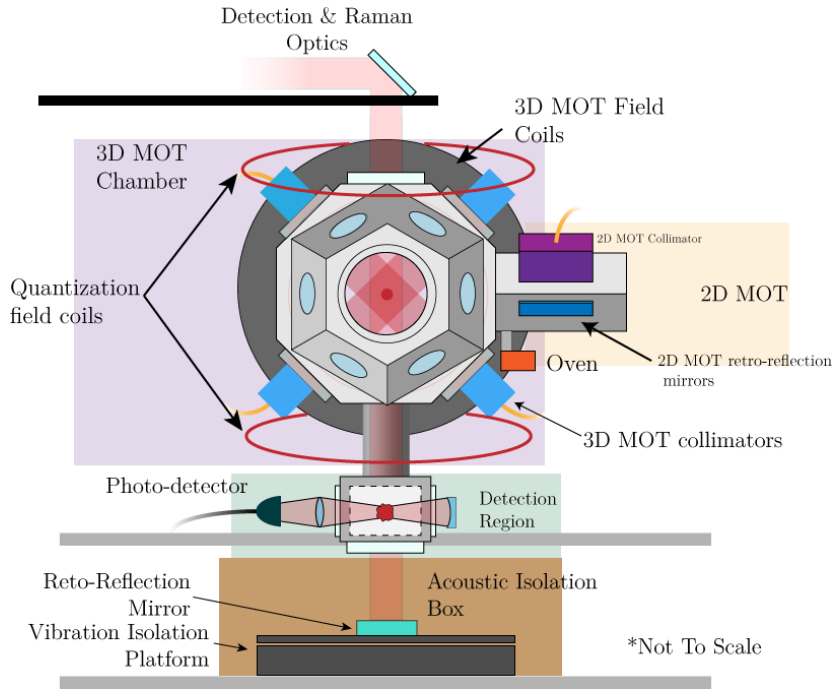


Figure 3.1: An overview of the experiment.

The main structure of the 2D and 3D chambers are constructed from milled aluminum. Across all chambers, viewports are indium sealed to the aluminum body to allow optical access to the atoms. The entire apparatus is sealed and pumped to vacuum with a residual pressure of $\approx 4 \times 10^{-11}$ mbar. This is achieved with an ion getter pump (IGP) [Gamma Vacuum, TiTan-IGP, 401/s] and a titanium sublimation pump [VG-Scienta, ZST23], and monitored by a cold cathode gauge [Vacuum Generators, ZCR40R].

The 2D MOT chamber is used to collect atoms, cool them along 2 dimensions with the un-cooled axis aimed towards the 3D MOT chamber via a differential pumping stage. The chamber is a glass cell which is a rectangular cuboid in shape with a connection to the atomic source ovens. Surrounding the glass cell is a metal structure with optical access to the glass cell. Housed within the metal structure are magnetic field coils, arranged in a quadrupole configuration. Attached to the metal structure on two of the lateral faces (orthogonal relative to each other) are collimators which connect to an optical fiber which links to the 2D MOT light distribution module (discussed later). Counter to each of the collimators are retro-reflection mirrors aligned to the collimator.

Within the 3D MOT chamber, atoms are cooled, trapped, prepared and, released; where they enter the free fall tube. Geometrically the chamber is comprised of two hexagonal prisms bisected by an octagonal prism². Along each edge face of the hexagonal prisms is a 1.5 cm viewport [Heraeus INFRASIL 301] for optical access. Each viewport is custom coated with an anti-reflective coating [Laseroptik Garbsen, B-01196] for light with wavelengths 767 nm, 780 nm, 1064 nm and 1960 nm. Of the total 12 hexagonal edge view ports 4 are currently used for dipole trap beam access, 2 are used for absorption imaging, and 1 is used for basic MOT monitoring. Both base faces are capped with a 7 cm view ports used for 2 MOT beams (one along each direction) as well access for an in-house built microwave horn capable of performing microwave transitions and optical access for a CCD imaging device [ALLIED vision technologies Guppy GF 033B].

Two coils are used to generate the quadruple field for the 3D MOT, placed on either side of the octagonal prism. Five 1.5 cm viewports adorn the faces of the aluminum octagonal prism, 4 of which are used for 3D MOT collimators which are attached and the top viewport is used for RAMAN and detection light access. Attached to one edge face is a tube which is used for vacuum monitoring and the IGP. Counter the IGP pump tube is the 2D MOT connection. The bottom octagonal edge face is connected to the free fall tube with a lead seal. The tube connects the 3D MOT chamber to the detection region.

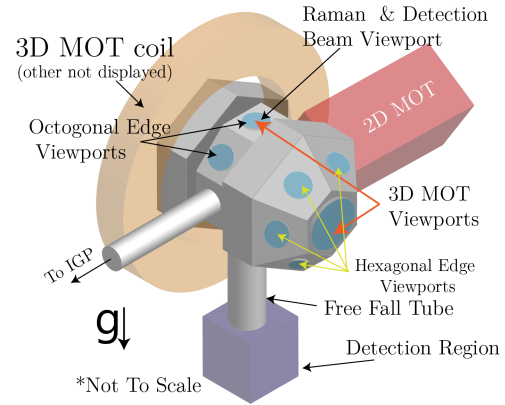


Figure 3.2: A model of the 3D MOT chamber. Not all components and viewports are shown. This model is not to scale.

²Prism here refers to the geometric shape and not an optical component.

The center of the detection region is 228 mm below the center of the 3D MOT chamber, corresponding to a free fall time of 213 ms.

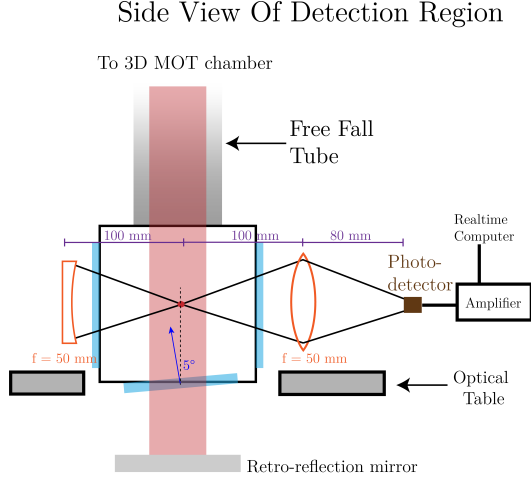


Figure 3.3: Detection system and corresponding optics.

On the bottom of the detection chamber is a viewport angled with a 5° tilt relative to the vertical axis to avoid parasitic cavities between it and the top viewport. This bottom viewport is where the RAMAN light exits the vacuum chamber, and is then retro-reflected back from a mirror below which is outside of vacuum.

On one edge face of the detection chamber a positioned 100 mm away from the center of the detection region is lens with focal length $f = 50$ mm. 80 mm behind the lens is a photo detector [OSI Opto Electronics PIN 10D] which is connected to a low noise amplifier [Femto DLPCA-2000] and connected to the input into an ADC. Opposite to the lens detection side of the detection chamber is a viewport with a $f = 50$ mm concave mirror placed 100 mm from the center of the detection zone. This mirror is designed to enhance the fluorescence signal measured on the photo-diode.

Quantization Field Coils

Cooling, interferometry and detection, requires the ability address the hyperfine structure of ^{87}Rb . In this experiment, this is achieved through the use of a magnetic field generated from two coils in a HELMHOLTZ configuration, which are centered around the free fall trajectory of the atoms over the entire free fall distance. The two coils are separated by a distance of 20 cm with a large radius which ensures for a uniform field over the the trajectory of the atoms.

The magnetic field can be calculated from the BIOT-SAVART law for a single coil. For our coil configuration, where the coil radius is equal to the coil separation, $R = D = 20$ cm, the field at the center is given by equation 3.1.

$$\vec{B} = \frac{8}{5\sqrt{5}} \frac{\mu_0 n I}{R} \quad (3.1)$$

Where B is the magnetic field, μ_0 is the free-space permeability constant and n is the number of windings and I is the coil current. The coils within this experiment have 8 windings each, a radius

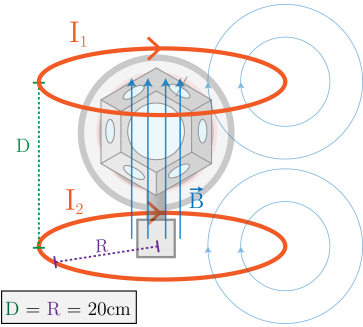


Figure 3.4: Two coils with radius R generate a uniform magnetic field over the free fall tube. This field can be used to shift the hyperfine energy levels, allowing us to optically address these states.

of $R = 20$ cm and current $I = 1.2$ A, generating a magnetic field $B = 43 \mu\text{T}$ in the center of our coils.

To reduce the influence of background magnetic fields, including those generated from the Earth, we utilize a magnetic field isolation.

3.1.2 Laser System

Light generation, amplification, frequency control, switching and distribution are all performed on an optical table separate from the optical table housing the science chamber and connected via optical fibers, which are fiber-coupled from the source optical table.

On the source optical table, light is generated from 5 external cavity diode lasers (ECDL) [61, 62] lasers which utilized for 4 distinct subsystems: reference, 3D MOT light, 2D MOT light and RAMAN Light.

Stable ^{87}Rb reference light is generated by locking to the $|F = 2\rangle - |F = 3\rangle$ cross-over line of the D_2 transition using frequency modulation spectroscopy. This light is then fiber coupled for use with the other laser systems required for cooling and interferometry.³

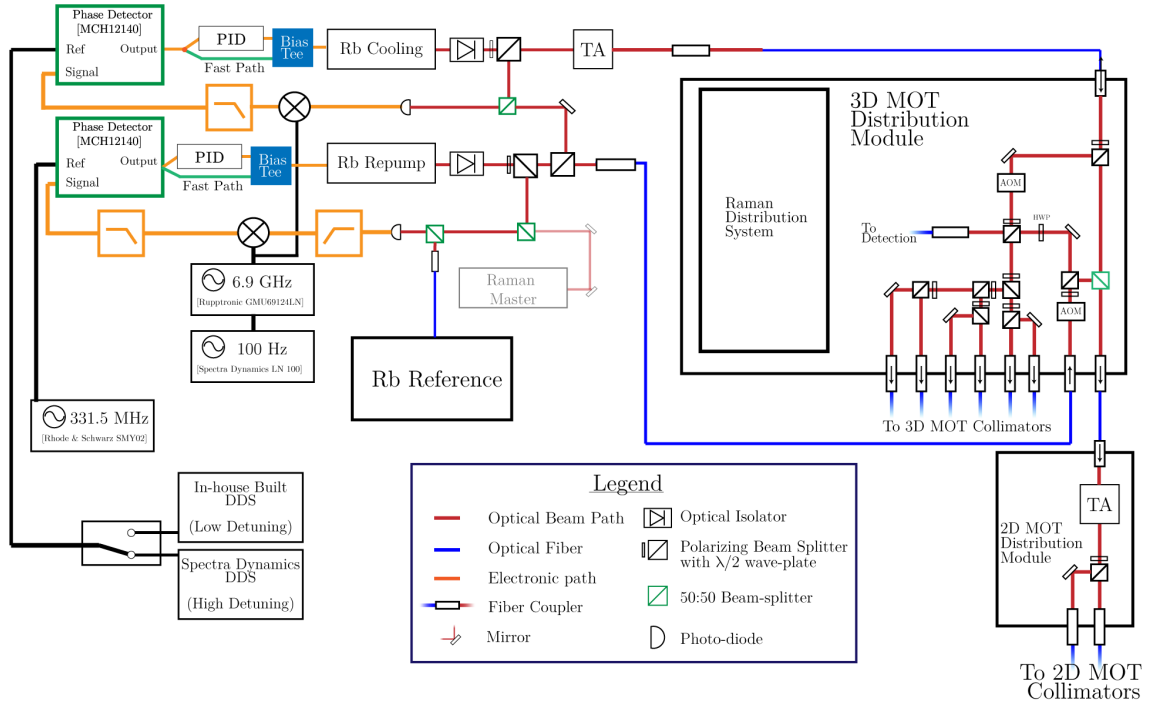


Figure 3.5: A simplified model of the light distribution paths in the experiment. The potassium system, and alignment optics are excluded from this model for clarity. The RAMAN system is shown in figure 3.6

Cooling and repump light for the 2D and 3D MOT systems for rubidium is common and is generated from two ECDLs with an output of roughly ≈ 30 mW per laser. An optical isolator

³A thorough discussion of the ^{87}Rb reference system can be found in [63].

placed after each ECDL prevents back reflections from interfering with the diode within the ECDL. Approximately ≈ 3 mW is diverted from the main path for locking to the reference using a $\lambda/2$ wave plate and polarizing beam-splitter (PBS). After the reference laser lock path, a portion is separated for the cooling laser lock. The remaining light passes through a $\lambda/2$ wave plate and fiber coupled into a polarization maintaining fiber and sent to the 3D distribution module.

The repump light diverted from the first PBS is overlaid with light from the reference laser and collected on an ultra-fast photodiode [Hamamatsu - G4176-03]; which is shared with the RAMAN Master Laser. From a Bias-tee connected to the photodiode we obtain the RF signal, which is high-pass filtered to separate it from the RAMAN Master beat note. We amplify the signal and mix down the signal with a 6.9 GHz oscillator [Rupptronik GMU69124LN]. The signal is low-pass filtered and compared to a reference 331.5 MHz oscillator [Rhode Schwarz SMY02] on a phase detector [MCH12140]. This signal is fed to a PID controller and the error signal which is fed back to the laser ring-piezo of the ECDL. A 'fast-path' output is from the phase detector and sent through a bias tee, which we couple directly to the current of the laser.

Cooling light is sent into a 1 W tapered amplifier [Eagleyard EYP-TPA-0780]. The amplified light passes through an additional optical isolator, $\lambda/2$ waveplate and PBS. Approximately ≈ 3 mW are diverted offset locked to the RP light. The combined repump cooler beat-note is measured on an ultra-fast photodiode [Hamamatsu - G4176-03], amplified and mixed down with a 6.9 GHz oscillator [Rupptronik GMU69124LN]. The signal is then low-pass filtered and sent as the signal input to a phase detector [MCH12140]. We require the ability to change the cooling detuning for sub-DOPPLER cooling, so the reference is an in-house built Direct digital synthesis (DDS) for low detunings ($\delta_{\text{Cool}} = 0-14\Gamma$) and can switched to a [Spectra Dynamics LNFS-100] for large detunings ($\delta_{\text{Cool}} \geq 15\Gamma$). The signal is sent to the laser diode and PID controller. The remainder of the cooling light passes through a $\lambda/2$ wave plate, fiber coupled into a PM fiber and sent to the 3D distribution module.

Within the 3D distribution module light, ≈ 20 mW of rubidium 3D cooling light is picked off for the 2D MOT system. The remainder of the light passes through an 80 MHz AOM, used for switching.

Approximately ≈ 6 mW of the rubidium cooling light is diverted from the post-AOM path for detection. The light passes through a mechanical shutter and sent to a series of polarizing beam-splitters that distribute the light into 6 distinct paths optical paths, 1 for each MOT collimator. Each MOT light path is set to a linear polarization using a wave plate to match the slow axis of a polarization maintaining (PM) fiber. The light is coupled into a polarization maintaining fiber and sent to the 3D MOT collimator.

Within each MOT collimator light from the fiber is outcoupled to free space, collimated and polarized to either σ_+ or σ_- to match the MOT configuration [58]. Approximately ≈ 8 mW are fiber coupled into each 3D MOT collimator, and the ratio of powers between the 6 paths can be altered by changing the angle of the distribution $\lambda/2$ wave plates. The fiber coupled RP light is also sent to the 3D distribution module. A portion is diverted and overlaid with the 2D MOT cooling light. The remainder of the repump light is overlaid with detection and 3D MOT cooling light and also distributed amongst the MOT collimator fibers.

The overlaid cooling and repump light for the 2D module passes through a $\lambda/2$ wave plate and fiber coupled into a PM fiber. This light is then sent to the 2D distribution module. Within the 2D module the combined repump cooling light seeds a 2 W tapered amplifier [Eagleyard EYP-TPA-0780]. The output light passes through an optical isolator and is split to two fiber cou-

pled paths for the 2D MOT collimators. Light within the 2D MOT collimator passes through a $\lambda/4$ waveplate to give the light σ_+ or σ_- in accordance with the 2D MOT configuration [60].

Interferometry Light

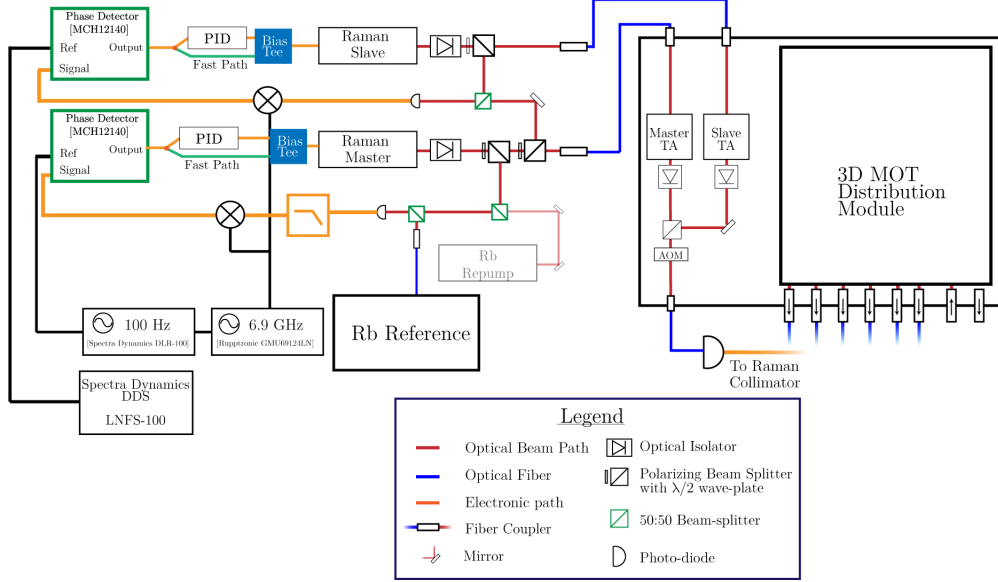


Figure 3.6: The RAMAN laser system as outlined below.

Interferometry light is generated from two source lasers, which we will refer to as the **Raman Master** and **Raman Slave**. Raman Master light is generated from an ECDL, a portion of this light is sent to the lock path, where it is overlaid with reference and picked up by an ultra-fast photodiode; the one shared with the repump laser. From the bias tee the Raman signal is separated through the use of a low-pass filter, amplified and mixed with a 1.6 GHz synthesizer. The signal is referenced to a 100 MHz stable reference [spectra dynamics 100] on a phase detector [MCH12140]. The phase output is sent via fast path to the laser current, and the error signal is sent to a PID which sends feedback signal to the laser piezo.

Raman Slave light is generated using an ECDL, a portion is diverted for locking. This light is overlaid with the Raman Master, and collected on an ultra-fast photo-diode [Hamamatsu - G4176-03]. From the bias tee, the signal is amplified and mixed down with a stable 6.9 GHz oscillator [Rupptronik GMU69124LN]. Interferometry in this experiment requires precise control of the Raman Slave detuning. The mixed down signal is referenced to signal from a DDS [Spectra Dynamics LNFS-100]. By phase-locking to a DDS we generate the frequency sweeps required for inertially sensitive interferometry. The phase-detector signal is sent to a PID controller. The remainder of the Slave light is fiber coupled and sent to the RAMAN module.

Within the RAMAN module, fiber coupled RAMAN Master and Slave light are sent through collimators, through optical isolators and then into 1 W tapered amplifiers. The RAMAN Master and Slave are overlaid, and the ratio of optical power between the Master and Slave can be tuned

by using a $\lambda/2$ waveplate and a PBS. This allows us to set the ratio that compensates the AC stark shift[57]. This light is then sent through an 80 MHz AOM [Crystal Technology 3200-124]. The combined light is coupled into the 1st order of the AOM and coupled into a fiber which is sent to the RAMAN collimator. By having light from the 1st order coupled into the fiber, we can switch the AOM to allow for short pulses.

Raman and Detection Beam Path

Linearly polarized RAMAN light from the distribution module is sent to a collimator via PM fiber which collimates the light with a beam $1/e^2$ radius of 2 cm. Similarly linearly polarized light from the detection path of the distribution module is sent to a different collimator⁴. Light from the RAMAN and detection is overlaid on a polarizing beam-splitter (figure 3.7). The detection and RAMAN light are sent through an iris with manually controlled aperture, followed by a $\lambda/4$ wave plate, which generates for σ -polarized light required for stimulated RAMAN transitions. The detection and RAMAN light are then reflected off two mirrors which which divert the beam into a vertical alignment.

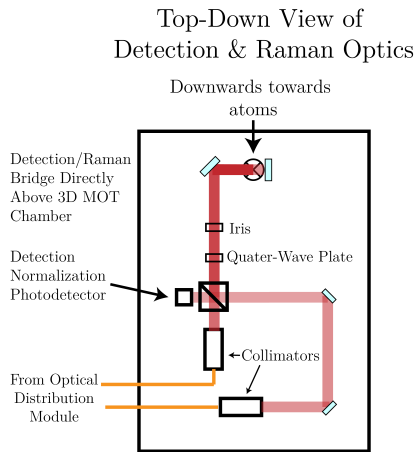


Figure 3.7: A top-down view of the fiber bridge located directly over the 3D MOT chamber.

The light passes through the top edge window of the octagonal prism through the 3D MOT chamber, the free fall tube, and through the bottom window of the detection chamber. This combined light is retro-reflected off of a mirror with surface flatness $\lambda/20$ [Fichou]⁵. The retro-reflection mirror is placed upon a vibration isolation platform [Minus K 150BM-1], which is housed in an acoustic isolation box. The retro-reflected light is aligned to match the path of the incoming light, both of which are aligned to the axis of gravitational acceleration⁶. Retro-reflected light passes back through the $\lambda/4$ plate, giving orthogonal polarization to the incoming light. The light is reflected from the polarizing beam cube and is sent to a photodetector which can be used for detection light optical power monitoring.

⁴Although the detection and RAMAN beams share the same path, they can be independently switched on or off relative to each other

⁵In the case of the OMIS, this retro-reflection mirror was replaced with a 1 in square mirror with the OMIS attached, (section 5B.3).

⁶To align the incoming RAMAN beam, we place a container with oil large enough to minimize meniscus effects directly under the RAMAN beam. The oil's surface will settle perpendicular to the gravitational acceleration. Light from above is aligned match the retro-reflected light from the oil. The retro-reflection mirror is then replaced and aligned to match the incoming beam, at which point the RAMAN beam is aligned parallel to the axis of gravitational acceleration.

3.2 Experimental Sequence

All experiment controlled elements such as AOM switching, DDS triggering, shutter switches, coil current, changes in detuning, *etc.* are individually programmed to occur at a specific time in the experimental sequence. Before each measurement cycle, this sequence is sent to a **National Instruments Real-time** computer, which executes the program by outputting the appropriate Transistor-Transistor Logic (TTL) signals and analog voltage outputs to each individual experimental element at the proper time during the measurement. The interface between experimental elements and control computer is facilitated through the use of input-output cards [NI PCI 6723] and [NI PCI 6229].

3.2.1 Cooling and Trapping

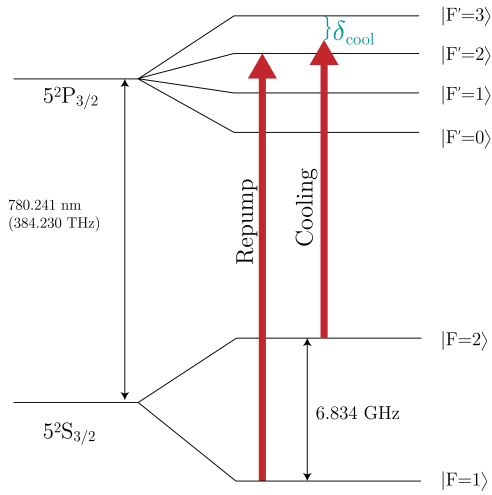


Figure 3.8: Cooling and repump light. Cooling light is red-detuned from the $|F = 2\rangle \rightarrow |F' = 3\rangle$ transition by δ_{cool} . Repump light is resonantly tuned to the $|F = 1\rangle \rightarrow |F' = 2\rangle$ transition.

Loading of the 3D MOT trap begins when ovens heat a sample of rubidium containing ^{87}Rb , causing sublimation to vapor. This atomic vapor diffuses into the 2D MOT chamber where light generated on the optical table, and the magnetic field coils confine the ^{87}Rb vapor into a cold atomic beam. Atoms pass through the differential pumping stage and into the 3D MOT chamber.

Light along 3 orthogonal axes is generated from the 6 MOT collimators, which are fiber coupled to the 3D distribution module. Magnetic field coils arranged in a anti-HELMHOLTZ configuration create a magnetic field minimum at the center of the 3D MOT chamber. The cooling light is $\delta_{\text{cool}} = 2.6\Gamma$ (14.9 MHz) red detuned from the $|F = 2\rangle \rightarrow |F' = 3\rangle$ transition. Atoms that decay into the $|F = 1\rangle$ state are dark to the cooling cycle transition, and therefore repump light tuned to the $|F = 1\rangle \rightarrow |F' = 2\rangle$ transition is used. Atoms in the $|F' = 2\rangle$ state will decay, into the $|F = 2\rangle$ state,

among others, and hence are reintroduced into the cooling cycle. Once loading is complete, the magnetic field is switched off and the atoms enter free fall.

The sample can be cooled below the DOPPLER limit cooling through polarization gradient cooling [64, 65], which brings the temperature of the atoms to $6.4\ \mu\text{K}$. This is achieved by switching off the repump light, and further red detuning the cooling light to $8\ \Gamma$ (45.9 MHz). After sub-DOPPLER cooling, the ensemble is ready for state-preparation.

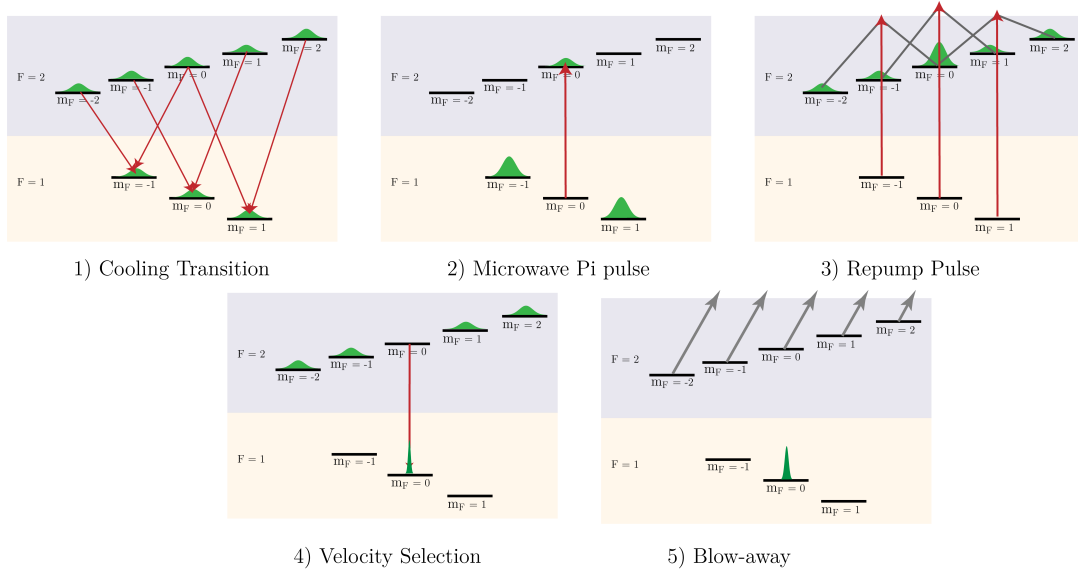


Figure 3.9: The state preparation method as outlined below.

3.2.2 State Preparation

Preparation into the $|F = 1, m_f = 0\rangle$ sub-state reduces magnetic field sensitivity and provides a pure state to perform interferometry with. The process is outlined in detail here [57, 66]. The primary steps of state-preparation process are as follows:

1. Cooling light from the polarization gradient cooling has optically pumped atoms into the $|F = 1\rangle$ state.
2. A microwave π pulse transfers atoms from the $|F = 1, m_F = 0\rangle \rightarrow |F = 2, m_F = 0\rangle$ state. Transferring $1/3$ of the total atoms in the $|F = 1\rangle$ state to the $|F = 2\rangle$ state.
3. Resonant repump light is turned on and atoms in the $|F = 1\rangle$ manifold are driven to the $|F' = 2\rangle$ state, from which they decay into the $|F = 2\rangle$ manifold.
4. A two photon RAMAN transition performs velocity selection [67], transferring atoms within a velocity slice back to the $|F = 1, m_F = 0\rangle$ state.
5. Cooling light is tuned to the resonance of the $|F = 2\rangle \rightarrow |F = 3\rangle$ transition and atoms are blown away from the $|F = 2\rangle$ state ejecting atoms from the ensemble.

3.2.3 Raman Transitions

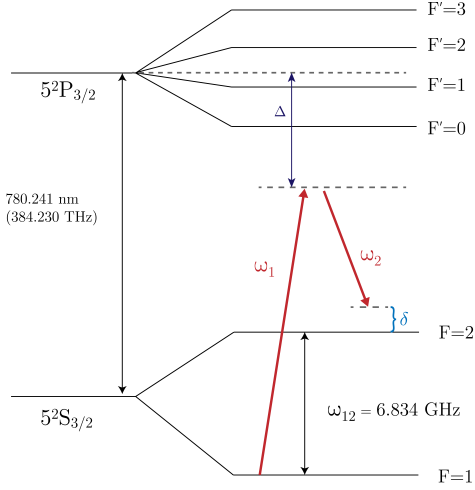


Figure 3.10: Two photon transitions transfer the atoms from the $|F = 1\rangle$ $|F = 2\rangle$ state. The overall detuning to the $5^2P_{3/2}$

Atom interferometry is performed on the $|F = 1, m_f = 0\rangle \rightarrow |F = 2, m_f = 0\rangle$ states of the $5^2S_{1/2}$ level of ^{87}Rb . The driving frequency of the transition is determined by performing a frequency scan on the prepared $|F = 1, m_f = 0\rangle$ state atoms. A measurement with a RAMAN pulse with length τ_π and a detuning δ (figure 3.10) is performed on the prepared atoms, and the $P_{|F=2\rangle}$ population is recorded. With the DDS as a reference on the Slave phase detector, we can change the frequency of δ by changing the frequency of the DDS. This measurement is repeated scanning the $|F = 2\rangle$ population as a function of RAMAN Slave detuning (figure 3.11).

The quantization field lifts degeneracy of the $|F = 1\rangle \rightarrow |F = 2\rangle$ transition, allowing for sub-state transitions. However, due to the two-photon selection rules [68] for the polarization vectors of the driving fields within this experiment, we can only drive transitions between between sub-states where $\Delta m_f = 0$. In our spec-

troscopy measurement, the splitting of the hyperfine states is given by the weak field ZEEEMAN effect, equation 3.2.

$$\Delta \omega_{m_F}^{\text{Zeeman}} = m_f \frac{\mu_0}{\hbar} g_F \vec{B}; \quad (3.2)$$

Where \vec{B} is the magnetic field, μ_0 is the BOHR magneton, and g_f is the LANDÉ-g factor for the sub-states of ^{87}Rb [69].

Once the 3D MOT field coils are switched off, the atoms are no longer trapped and will undergo gravitational acceleration. This acceleration will DOPPLER shift the transition frequency of the atoms relative to the laboratory frame as $\omega(t)_{\text{Doppler}} = 2\pi \vec{k}_{\text{eff}} \cdot \vec{v}_{\text{COM}}(t)$. Where $\vec{v}_{\text{COM}}(t)$ is the center of mass velocity of the ensemble over time.

The standing wave configuration of the interferometry light generates two pairs of counter-propagating beams capable of addressing the atoms, as well as two pairs of co-propagating beams. The counter-propagating RAMAN beams which are sensitive to the ensemble acceleration are referred to DOPPLER *sensitive*, and the co-propagating beams which are not shifted by the ensemble acceleration are referred to DOPPLER *insensitive* transitions. Under gravitational acceleration, the velocity of the ensemble will linearly increase, and therefore to stay resonant with an atomic transition, we can provide a linear ramp of the Slave laser from the initial transition frequency, equation 3.3.

$$\alpha = \frac{d\omega}{dt} \quad (3.3)$$

By sweeping the frequency negatively or positively over time, we can address the atoms with a specific pair of counter-propagating beams. The residual momentum given by $\vec{p} = \hbar\vec{k}_{\text{eff}}$ is dependent on which pair of counter-propagating beams are used.

Beyond the center of motion DOPPLER shift, the non-zero temperature of the cloud constitute a distribution of velocities around the center of mass. This velocity follows a MAXWELL–BOLTZMANN distribution. The $1/e$ DOPPLER broadening-width of the frequency spread is given by equation 3.4.

$$\sigma = k_{\text{eff}} \sqrt{\frac{2k_{\text{B}}T_e}{m}} \quad (3.4)$$

Where k_{B} is the BOLTZMANN constant, m is the mass of a ^{87}Rb particle, and T_e is the ensemble temperature.

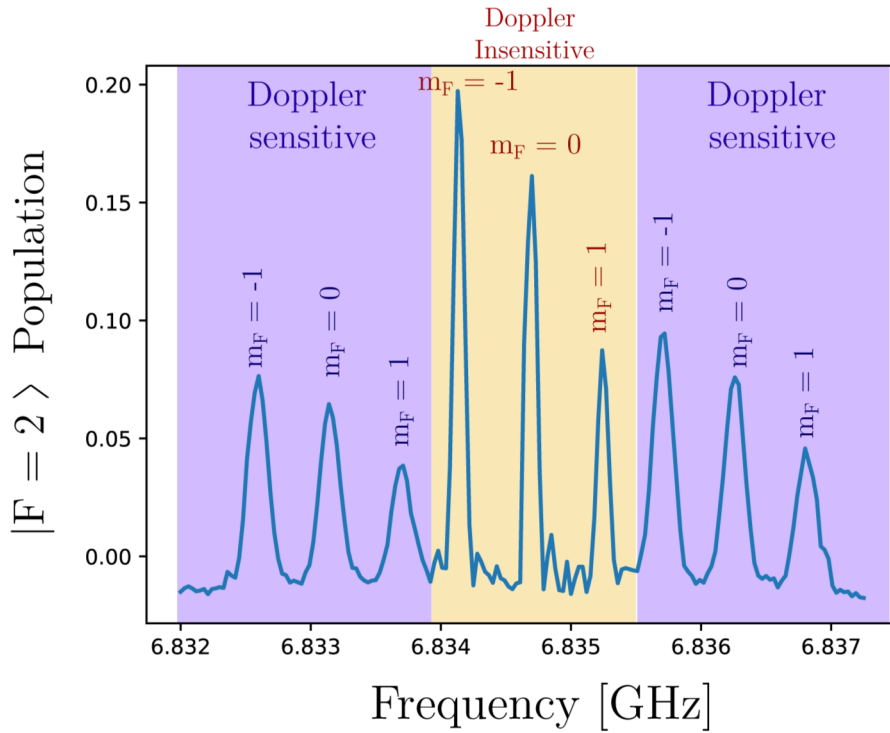


Figure 3.11: Spectroscopy of the $|F=1\rangle \rightarrow |F=2\rangle$ transition. The magnetic field from the quantization field splits the magnetic sub-states. Gravitational acceleration DOPPLER shifts the transitions depending on the direction of momentum transfer from the two-photon transition. Lastly the velocity spread of the ensemble around the center of mass motion DOPPLER broadens the transitions.

3.2.4 Interferometry

A MACH-ZEHNDER type atom interferometer is constructed from a set of $\frac{\pi}{2} - \pi - \frac{\pi}{2}$ pulses, with a separation time T between the pulses. As mentioned above, as the ensemble accelerates the frequency of the inertially sensitive transitions will linearly change in time. This means a RAMAN detuning δ resonant to a transition at the start of the interferometer will not be resonant at the last pulse. To compensate the DOPPLER shift, we linearly sweep the RAMAN detuning, equation 3.3. Additionally the direction of the sweep allow to address a specific direction of momentum transfer.

Once the atoms are prepared into the $|F = 1, m_f = 0\rangle$ state we begin interferometry. At the velocity selective pulse of the state preparation we begin to sweep the frequency with $\alpha \approx 25.2 \text{ MHz s}^{-1}$ for 200 ms covering the length of the atom interferometer.

We can define an interferometer time which starts at $t_{\text{int}} = 0$ with the first $\frac{\pi}{2}$ pulse. The AOM controlling the fiber coupling into the bridge fiber is switched on for $\tau = \frac{\pi}{2\Omega}$, transferring the atoms into a superposition of $|F = 1, \vec{p}_0\rangle$ and $|F = 2, \vec{p}_0 + \hbar\vec{k}_{\text{eff}}\rangle$. At $t_{\text{int}} = \tau$ the AOM is switched and RAMAN light is no longer present in the chamber. The ensemble evolves in the superposition for a free evolution time T . At $t_{\text{int}} = T + \tau$, Raman light is again switched on until $t_{\text{int}} = 3\tau + T$, reflecting the internal and external states the ensemble. After the light is switched off the atoms enter a free evolution time T . Lastly the atoms undergo one last $\frac{\pi}{2}$ pulse at $t_{\text{int}} = 3\tau + 2T$. This recombines the superposition of states, at which point the final atomic state of the atoms can be read-off with state selective detection.

3.3 Detection and Evaluation of data

After interferometry the phase information can be obtained by reading out the final output population of the interferometer. In this experiment, this is achieved by using state selective fluorescence detection⁷.

As the atoms enter the detection region, resonant cooling light is switched on for 600 μs , during which time atoms cycle on this transition fluorescing photons, which are picked up by the detection photo-diode. From there the cooling light is switched off and repump light is switched on for 200 μs , resonant with the $|F = 1\rangle \rightarrow |F' = 2\rangle$ transition, from which the atoms decay into the $|F = 2\rangle$. With atoms in the $|F = 2\rangle$ state, the resonant $|F = 2\rangle \rightarrow |F' = 3\rangle$ light is pulsed again for 600 μs , and the fluorescence signal is measured again. After 20 ms, long after the atoms have left the detection region, a final 600 μs pulse occurs, and the background signal is measured. During each pulse the cooling pulse intensity is monitored to account for changes in optical power during detection. This is obtained from the reflected detection signal on a photo-detector on the detection bridge.

The fluorescence signal is measured by dividing the first two cooling pulse signals to obtain population information from the output of the atom interferometer⁸, equation 3.5.

$$P_{\text{output}} \propto \frac{N_{|F=2\rangle}}{N_{|F=1\rangle} + N_{|F=2\rangle}} \quad (3.5)$$

⁷Absorption imaging or spatial resolution are not applicable to this experimental setup. The cloud density is too low, and spatial separation is minimal

⁸In reality the background pulses and normalized photo-diode response are taken into account when measuring the relative population, but are not shown here for clarity.

3.3.1 Measuring the Gravitational Acceleration

The population of the $|F = 2\rangle$ state of the atom interferometer is dependent on the phase difference between the two paths, equation 4.3.

$$P_{|F=2\rangle} = \frac{C_0}{2} [1 + \cos(\Delta\Phi)] + B \quad (3.6)$$

Where C_0 is the fringe contrast, and B is the offset. For our experiment, the leading order phase shift is dependent on the gravitational acceleration. Incorporating the linear sweep of the RAMAN detuning α , we get equation, 3.7.

$$\Delta\Phi = k_{\text{eff}} \left(g - \frac{\alpha}{k_{\text{eff}}} \right) T^2 \quad (3.7)$$

By altering the sweep rate α we can scan the output of the atom interferometer. For a sweep rate $\alpha = k_{\text{eff}} g$, the phase difference between the two paths of the interferometer is zero, $\Delta\Phi = 0$ for all pulse separation times T . Experimentally we can measure the value of g by scanning α for various pulse separation times, and determining where $\alpha = k_{\text{eff}} g$.

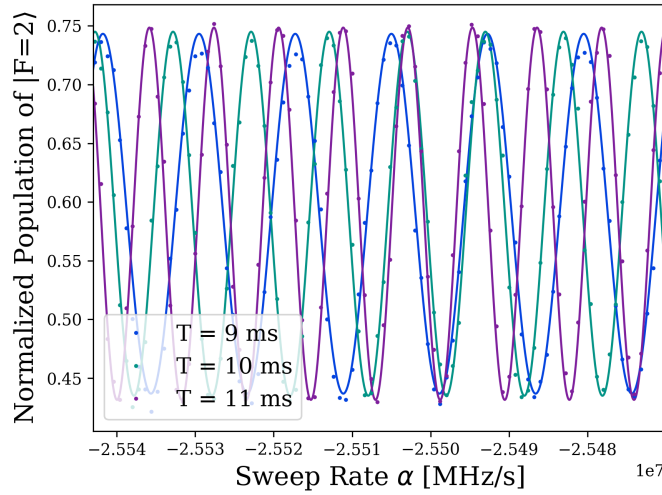


Figure 3.12: Data (points) and fit for a scan of a $T = 9$ ms, $T = 9$ ms and $T = 9$ ms atom interferometers.

Once the value of the sweep rate corresponding to the gravitational acceleration is known, since k_{eff} is experimentally determined, we can calculate the gravitational acceleration from equation 3.8.

$$g = \frac{\alpha}{k_{\text{eff}}} \quad (3.8)$$

Gravitational acceleration is a dynamic quantity, and therefore the sweep-rate that matches the gravitational acceleration will change over time. There are multiple methods for dynamically tracking the gravitational acceleration over time.

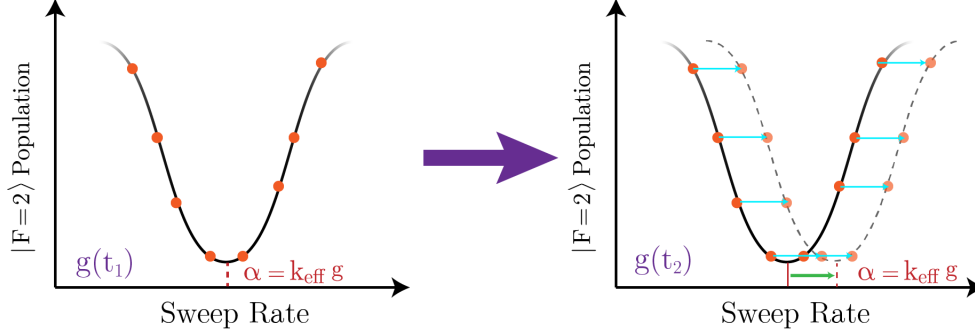


Figure 3.13: The multiple sweep rate measurement. Performing this measurement over time will allow us to fit, and track changes in the gravitational acceleration.

Method 1: Entails tracking g by scanning α (figure 3.13) with a set number of points around the fringe minimum (usually 4-10) with equidistant sweep rate increments (figure 3.13). From the resultant population measurements a sinusoid can be fit. All parameters except the phase of the sinusoid are determined by experiment, and therefore we can record the phase of the fit, from which we can extract a value of g .

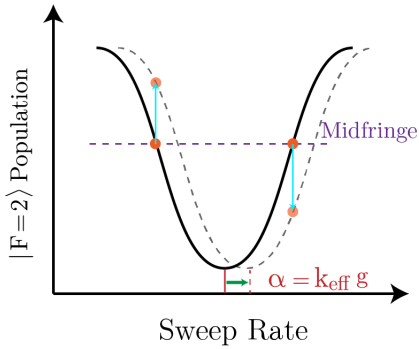


Figure 3.14: 2 point mid-fringe style measurement.

Method 2: [53] is to measure the output population at the sweep rates corresponding to the mid-fringe positions surrounding the fringe minimum (figure 3.3.1). A change in the gravitational acceleration will shift the output population relative to each other.

From the difference in population, an adaptive the positioning of α will maintain mid-fringe as the value of g changes. The main advantage of this two point measurement technique is a much higher measurement repetition rate. Instead requiring 4-10 atom interferometer measurements for one measurement of g , the measurement can be performed with 2 points. This measurement method is more sensitive to signal, but on the other hand is also more susceptible to phase-noise, and any phase shift enough to leave the non-linear regime of the fringe introduces ambiguity into the g measurement.

Method 3: A third measurement method will be explored further when analyzing measurements of the gravitational acceleration that enact vibration post correction (Section 5.1.6). This method entails sweeping with a fixed sweep rate corresponding to a mid-fringe position. Vibrations will shift the phase output of the interferometer around the mid-fringe point. We can apply the phase-corrections from the post-correction method, and fit a sine. By grouping the points into a large

enough bin to constitute a good sinusoidal fit, we can extract the phase of the fit and obtain the gravitational acceleration.

Once we have a set of measurements of the gravitational acceleration we can begin analyzing the time variance of the acceleration. We do this by calculating an ALLAN Deviation (ADEV) [70], from which we can obtain short and long term stability of the measurement.

3.3.2 Momentum Reversal

The output population of the atom interferometer is not only sensitive to the leading order phase shift, but also determined by effects that will shift the phase of our measurement away from the gravitational acceleration g . Some of these phase shifts are dependent on the direction of momentum transfer (such as the differential light shift [71, 72]), while others are independent. The phase difference at the output of the interferometer for a given direction of momentum transfer $\Delta\Phi_{(+)}$ or $\Delta\Phi_{(-)}$ we get equation 3.9.

$$\begin{aligned}\Delta\Phi_{(+)} &= \Delta\phi_g + \Delta\phi_{\text{independent}} + \Delta\phi_{\text{dependent}} \\ \Delta\Phi_{(-)} &= \Delta\phi_g + \Delta\phi_{\text{independent}} - \Delta\phi_{\text{dependent}}\end{aligned}\tag{3.9}$$

By changing directions of momentum transfer between measurements of the gravitational acceleration, we can take the differential of the two to reduce the effect from momentum independent shifts, equation 3.10.

$$\Delta\Phi = \frac{\Delta\Phi_{(+)} + \Delta\Phi_{(-)}}{2}\tag{3.10}$$

This experimental technique is known as momentum reversal, or ‘k-flip’ [73, 74]. Experimentally this is enacted by switching between the direction of momentum transfer between measurements of the gravitational acceleration.

Chapter 4

Inertial Noise and Post-Correction

4.1 Introduction

When performing atom interferometry, beam-splitter pulses require a strict phase relation between the counter-propagating beams. In the case of an atom gravimeter, any change in the phase relation cannot be discerned from an acceleration signal. Vibrations coupling into the retro-reflection mirror shift the wave-front phase relative to the incoming beam, adding an additional phase. This phase contribution is known as **inertial noise**. In comparison to other noise sources within the experiment, untreated inertial noise represents a large component, see table 4.1 for the leading phase uncertainties in our experiment. In this chapter we will discuss how ground motion creates inertial phase noise and what can be done to correct for it.

Noise Contribution	RMS Phase Uncertainty
Inertial Noise	434.0 mrad/ $\sqrt{\text{Hz}}$
Raman PLL Noise	40.2 mrad/ $\sqrt{\text{Hz}}$
Quantum Projection Noise	4.4 mrad/ $\sqrt{\text{Hz}}$

Table 4.1: A demonstration of the current largest noise sources in measurements of the local gravitational acceleration calculated for a $T = 78$ ms atom interferometer. Values were calculated for an atom interferometer in a quiet inertial environment with vibration isolation [Minus-K 150 BM-1], yet still inertial noise represents a large component of the total noise sources present. Calculations of these values can be found in section 5 A.2.

4.1.1 Sources of Inertial Noise

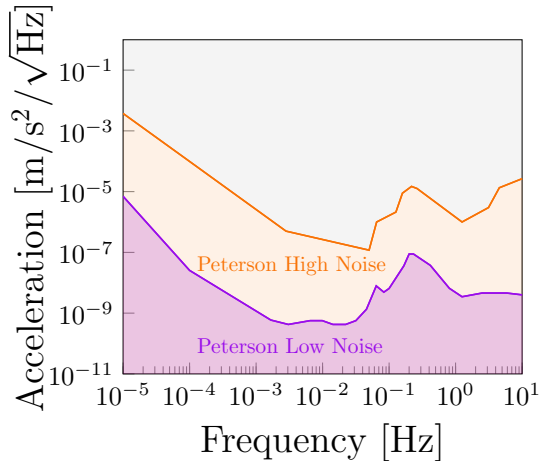


Figure 4.1: The PETERSON high and low noise models. These represent the base level of ground motion from the Earth. Even in relatively quiet environments ground motion from the Earth will couple into a gravimeter.

giving a scale that we know we can measure to.

Vibrations in normal laboratory conditions are several orders of magnitude above the PNHNM and are attributed to what we will refer to as cultural or anthropogenic noise [77, 78]. This noise stems from cars, railways, mechanical pumps and even wind turbines. This amalgamation of noise sources will collectively couple into an interferometer generating inertial noise.

¹This does not take into account extreme outliers such as volcanic eruption, earthquakes, or tsunamis.

4.2 How Vibrations affect the Atom Interferometer

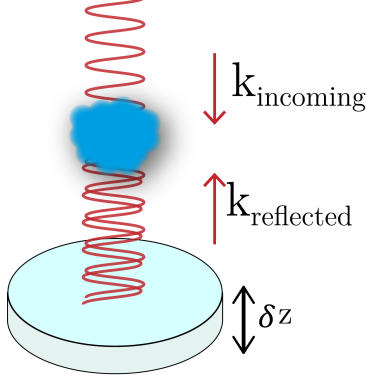


Figure 4.2: Relative to the incoming wave-front, vibrations of the incoming beam will distort the phase of the retro-reflected beam, effectively changing the phase relation between the two beams.

Any phase noise uncommon to the counter-propagating beams addressing the atoms will add a phase to the atom interferometer. In the case of our experiment, motion of the retro-reflection mirror shifts the phase of the retro-reflected light for only one direction of momentum transfer. For a displacement of the mirror δz , the induced phase shift of the reflected wave-front ϕ_{WF} is given by equation 4.1.

$$\delta\phi_{\text{WF}} = k_{\text{eff}}\delta z \quad (4.1)$$

Where we define \hat{z} parallel to \vec{k}_{eff} and therefore \vec{g} ³.

For a given atom interferometer sensitivity function [49] $g(t)$ (section 2.2.1) we can calculate the total atom interferometer phase shift $\Delta\phi_{\text{vib}}$ using equation 4.2.

$$\Delta\phi_{\text{vib}} = \int_{-\infty}^{\infty} g(t)d\phi(t) = \int_{-\infty}^{\infty} g(t)\frac{d\phi}{dt}dt \quad (4.2)$$

This vibration induced phase shift will change the output of the atom interferometer, in our case this will manifest as a change in the normalized population $P_{|F=2\rangle}$ the excited state, equation 4.3.

$$P_{|F=2\rangle} = \frac{C_0}{2}[1 + \cos(\Delta\Phi_{\text{Tot}})] + B \quad (4.3)$$

Where C_0 is the atom interferometer contrast, B is the atom interferometer offset, and $\Delta\Phi_{\text{Tot}}$ is defined by equation 4.4.

$$\Delta\Phi_{\text{Tot}} = \left(g - \frac{\alpha}{k_{\text{eff}}}\right) \cdot k_{\text{eff}}T^2 + \Delta\phi_{\text{vib}} + \Delta\phi_{\text{other}} \quad (4.4)$$

In our atom interferometer, which utilizes RAMAN pulses, our primary mechanism for scanning the output of the interferometer is changing the sweep rate of the RAMAN detuning, α . From equation 4.4, we can see that for a given α , for a non-time varying gravitational acceleration, we will measure a constant relative population $P_{|F=2\rangle}$ at the output of the interferometer. However, a non-zero contributions from vibrations will change the output of the interferometer for a constant sweep rate.

³The validity of this statement will be explored in section 5 A.2.2.

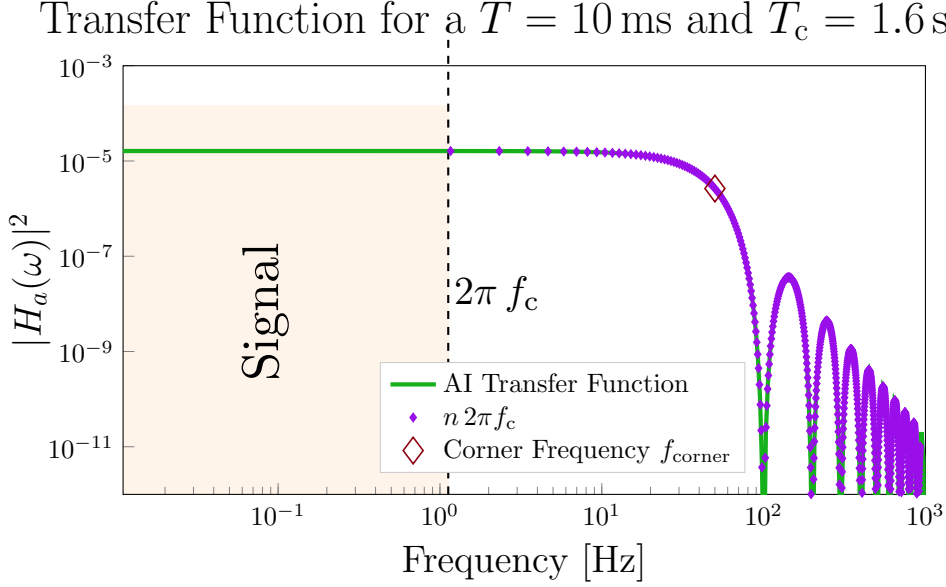


Figure 4.3: The acceleration transfer function $H_a(\omega)$ shows the atom interferometer's sensitivity to inertial noise with frequency ω . The atom interferometer is less sensitive to inertial noise as the frequency increases in a manner f^{-2} above the corner frequency, defined as $f_{\text{corner}} = 1/2T$. Vibration noise is sampled by the atom interferometer at the cycle frequency f_c of the atom interferometer.

4.2.1 Frequency Dependence of the Atom Interferometer to Vibrations

To obtain the frequency dependence of the atom interferometer to a inertial phase noise of frequency [49] ω , we can calculate the transfer function² $H_\phi(\omega)$ of the atom interferometer, equation 4.5.

$$H_\phi(\omega) = \omega G(\omega) \quad (4.5)$$

Where $G(\omega)$ is the FOURIER transform of the sensitivity function $g(t)$, equation 4.6.

$$G(\omega) = \frac{4\Omega i}{\omega^2 - \Omega^2} \sin\left(\frac{\omega}{2}(T + 2\tau)\right) \left(\cos\left(\frac{\omega}{2}(T + 2\tau)\right) + \frac{\Omega}{\omega} \sin\left(\frac{\omega}{2}T\right) \right) \quad (4.6)$$

For a given power spectral density of vibrations, $S_\phi(\omega)$, we can calculate the root mean squared phase spread ϕ_{RMS} of the atom interferometer from equation 4.7.

$$(\tilde{\phi}_{\text{RMS}})^2 = \int_{-\infty}^{\infty} |H_\phi(\omega)|^2 S_\phi(\omega) d\omega \quad (4.7)$$

We can calculate the acceleration power spectral density from the phase power spectral density from the relation defined in equation 4.1, giving us equation 4.8.

$$S_\phi(\omega) = k_{\text{eff}}^2 S_z(\omega) = \frac{k_{\text{eff}}^2}{\omega^4} S_a(\omega) \quad (4.8)$$

²The transfer function $H(\omega)$ is not to be confused with the *mechanical* transfer function, which describes how a vibration propagates through a system (a topic that will be explored in section 5 A.2.5).

Where $S_z(\omega)$ is the displacement power spectral density. We then define the acceleration transfer function in terms of the phase transfer function, equation 4.9.

$$(\tilde{\phi}_{\text{RMS}})^2 = k_{\text{eff}}^2 \int_0^\infty \frac{1}{\omega^4} |H_\phi(\omega)|^2 S_a(\omega) d\omega \quad (4.9)$$

For a set of n MACH-ZEHNDER measurement sequences with cycle time T_c and cycle frequency $f_c = 1/T_c$, the short term uncertainty of the atom interferometer will measure this RMS phase noise according to equation 4.10 [49].

$$\sigma_\phi^2(\tau) = \frac{k_{\text{eff}}^2}{\tau} \sum_{n=1}^\infty \frac{|H_\phi(2\pi n f_c)|^2}{(2\pi n f_c)^4} S_a(2\pi n f_c) \quad (4.10)$$

Any signal with a frequency lower than f_{cycle} will be measured by multiple cycles of the atom interferometer and is therefore interpreted as atom interferometer signal; *e.g.*, changes in gravitational acceleration due to the tidal force have a frequency much lower than the the cycle frequency f_c of the atom interferometer, and therefore do not contribute to the short term uncertainty of the atom interferometer, but rather are a measurable phenomena.

We can define the RMS acceleration noise \tilde{a}_{RMS} , which provides a useful metric as an upper bound to noise sources present in the atom interferometer. By utilizing the scale-factor $\phi = a k_{\text{eff}} T^2$, and applying it to equation 4.9, we get equation 4.11.

$$(\tilde{a}_{\text{RMS}})^2 = \int_0^\infty \underbrace{\frac{1}{T^2 \omega^4} |H_\phi(\omega)|^2}_{\equiv H_a(\omega)} S_a(\omega) d\omega \quad (4.11)$$

Where $H_a(\omega)$ is defined as the acceleration-transfer function. Lastly, we can use $H_a(\omega)$ to the short term uncertainty in terms of acceleration 4.12.

$$\sigma_a^2(\tau) = \frac{k_{\text{eff}}^2}{\tau} \sum_{n=1}^\infty |H_a(2\pi n f_c)|^2 S_a(2\pi n f_c) \quad (4.12)$$

4.3 Inertial Noise Mitigation in Atom Interferometers

We can now explore two methods for addressing vibrations: vibration attenuation systems which reduce the level of mirror motion, and inertial noise post-correction, which uses an external sensor to record the mirror motion and the weighting function of the atom interferometer to calculate the inertially induced phase shift.

4.3.1 Vibration Attenuation

One method for reducing noise induced by vibrations is to attempt to attenuate them to reduce the mirror motion as much as possible. This is also possible by choosing a low noise environment such as the Cold Atom Gravimeter (CAG) [79] which has performed gravimetry in the *Walferdange Underground Laboratory for Geodynamics*. However, restricting measurements of the gravitational acceleration to low noise environments excludes all but a few environments and therefore applications of the gravimeter, and one is still limited to micro-seismic noise.

We can however reduce the level of inertial noise in the system through the utilization of vibration isolation platforms. These systems typically employ a mass-spring system which exploit the property of harmonic oscillators through which motion above the resonance frequency f_0 is attenuated as $1/f^2$. These systems benefit greatly from attaining extremely low resonance frequencies, and therefore typically employ ‘negative spring constant’ mechanisms to achieve this. The mechanical design of these systems varies widely, but in general utilize compound spring systems that couple multiple degrees of freedom to keep a mass in equilibrium, however once the mass leaves equilibrium, the other degrees of freedom couple in to reduce the total spring constant. This allows for the spring constant to be tuned to a low value, therefore lowering the total resonance of the system. Negative spring constant systems can be found in the geometric anti-spring filters found in LIGO, VIRGO [80] and VLBAI [41]; the LaCoste super-spring systems of the FG-5 [28] and spring gravimeters; and in the Minus K BM-1 vibration isolation platform used within this experiment.

There are however several limitations to these vibration isolation systems, especially for field use gravimeters in noisy environments. The relatively portable vibration isolation systems can only attenuate the vibrations by a few orders of magnitude. Larger vibration attenuation systems can provide higher vibration attenuation, but their large weight of over 1 ton is not suitable for portability. Additionally, these systems tend to have low dynamic ranges, requiring tuning and consideration for environmental conditions such as temperature. Lastly at the resonance these systems offer no attenuation, and can in fact add noise, if not properly dampened.

4.3.2 Vibration Post correction

From equation 4.2, we can calculate the phase shift occurring at the output of the atom interferometer $\Delta\phi_{\text{Vib}}$ given by the phase shift of the RAMAN wave-front $\phi_{\text{WF}}(t)$, weighted by the sensitivity function $g(t)$. Knowing that the phase shift of the retro-reflection beam for a small displacement is given by $\delta\phi_{\text{WF}} = k_{\text{eff}}\delta z$. If we record the dynamic motion of the mirror and weight the signal according to the time dependent sensitivity function $g(t)$, we can calculate the phase shift that occurred during that measurement cycle. Additionally, by taking the derivative of the sensitivity function $g(t)$, we can obtain the velocity and acceleration sensitivity function; $g(t)$ and $g_a(t)$ respectively.

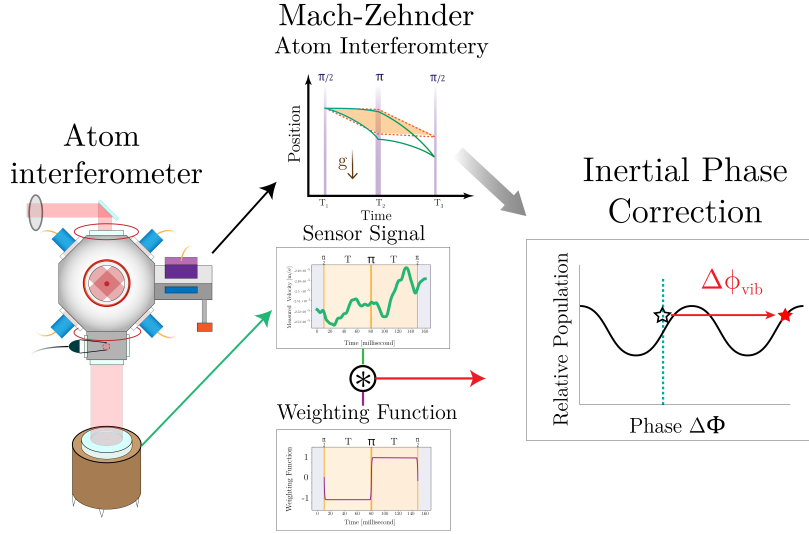


Figure 4.4: Inertial noise post-correction is performed by measuring the mirror motion during a MACH-ZEHNDER-type interferometer. By convolving the time dependent sensitivity function $g(t)$, we can calculate the phase shift ϕ_{PC} that occurred during the measurement cycle. We can then apply the phase shift to the measurement data to reconstruct the fringe.

$$\phi_{PC} = k_{\text{eff}} \int_0^{2T+4\tau} a_{\text{meas}}(t) g_a(t) dt \quad (4.13)$$

This is the operating principle behind inertial noise post-correction. The time dependent mirror motion during the atom interferometer cycle is measured using a motion sensor such as a seismometer or accelerometer and convolved with the appropriate sensitivity function to obtain the phase shift ϕ_{PC} . This phase shift is applied to the output of the interferometer to determine where the vibrations during the measurement cycle shifted the measurement to. This method is also called fringe-reconstruction, due to the fact, that for enough post-corrected data points, we can ‘reconstruct’ the fringe pattern from seemingly random noise. From this fringe reconstruction we can extract the phase of the fit and calculate the value of the gravitational acceleration for a given set of measurements.

The remainder of this work will discuss how this process is performed within our experiment, evaluation of the performance of different sensors and their limitations. Additionally using this concept we can utilize post-correction using a next generation motion sensor known as an optomechanical inertial sensor (OMIS).

Chapter 5

Sensor Post-correction

In this chapter we discuss the post-correction method used within this thesis, as well as measure and evaluate the performance of this method with various sensors. After the preface, this chapter has been broken into two separate sub-chapters: post-correction with commercially available sensors and opto-Mechanical enhanced atom Interferometry.

5.1 Post-correction Algorithm

The process of post-correction is performed by convolving signal from a motion sensor with the atom interferometer sensitivity function to produce a phase shift that corrects for the phase shift from inertial noise during a measurement cycle.

The process begins when signal from a motion sensor is recorded over the time interval of the atom interferometer. The sensor dependant amplitude and phase response (section A.1.2) will mandate the acceleration or velocity from the voltage measured. From this measured signal, we can then perform filtering to exclude non-physical signals generated by the sensors. Signal for some time from before and after the atom interferometer is also recorded, which allows us to compensate for any phase delays that occur between the atom interferometer and motion sensor. We can then use the signal along with the sensitivity function $g(t)$ to calculate the phase shift that occurred during that specific measurement cycle. Applying this phase shift to the data point corresponding to that measurement cycle, we can reconstruct the fringe pattern. To evaluate the performance of the post-correction,

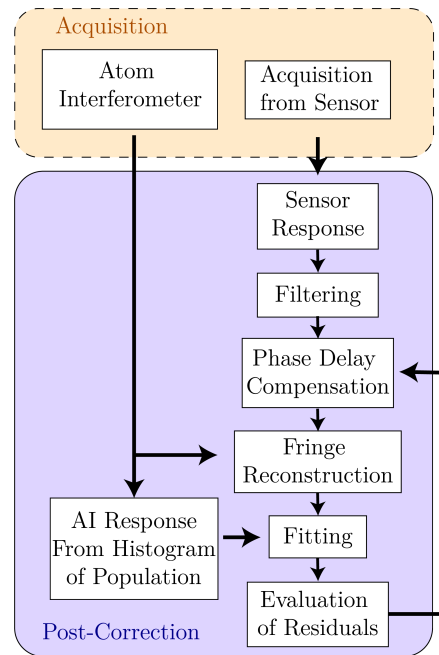


Figure 5.1: A concept model of the post-correction algorithm.

we fit a subset of the total data and extract the phase from the fit. Fit parameters are determined from the expected atom interferometer response, which is obtained by a histogram of the population data, or from previous measurement.

5.1.1 Sensor Preparation

The experimental setup for each commercial sensor was performed in a similar manner, only with minor variations to accommodate each sensor’s individual conditions. For inertial noise post correction in our experiment, the point of interest for measurement is the surface of the retro-reflection mirror. This means we need to physically connect the motion sensor to the retro-reflection mirror so that signal from the sensor reflects the motion of the mirror surface. Each sensor’s physical dimensions required a different method of attachment; for example for the flat surfaces of the **Nanometrics Titan** and the **Guralp CMG-40T** meant we could simply place the mirror atop the sensor. However for the **Nanometrics Trillium 240** and **Wilcoxon 731A** we required special mounting structures. These mounting structures contribute to a non-trivial transfer function, the ramifications of which will be discussed further in section 5 A.2.5. In every case, each sensor’s \hat{z} axis was aligned to the same axis as the retro-reflection beam¹, which is in turn aligned to the axis of gravitational acceleration.

For a post-correction with a given device, the sensor and retro-reflection mirror mounting structure were placed onto the vibration **Minus-K** isolation platform. Depending on the objective of the given measurement, we could switch between the vibration isolation between isolation mode (free-floating) or by-passed (strap-down). The sensor and mounting structure were placed in a manner so that the RAMAN beam was centered on the retro-reflection mirror. We then aligned the retro-reflection mirror so that the reflected RAMAN beam overlapped with the incoming RAMAN beam. Alignment was performed by changing the counterweight distribution on the surface of the vibration isolation platform.

The breakout box gives us access to the output of each axis of the sensor, as well as the ability to center the masses or change the sensors clipping level. Using shielded cables we connected the outputs of the breakout box to the pin-out box of the analog to digital converter. To reduce mechanical coupling of ground motion onto the vibration isolation platform, we utilized a ‘slack’ cable configuration [81].

With the exception of the **Wilcoxon 731A**, each device required a DC voltage between 12 V – 36 V for operation. To avoid line voltage noise, each sensor was powered by a 12 V deep cycle lead-acid battery. The **Titan** required interface with an external computer to set the value for it’s internal resistance, which determined the sensor’s sensitivity and clipping level. Once powered, the sensors were given time² to come to thermal equilibrium. The test masses of the seismometers were centered according to their user manual before each measurement.

¹Quantatative analysis of the alignment can be found in section 5 A.4.

²This time was sensor dependent, for the **Titan** this could be as little as 10 minutes, or as long as 1 hour for the **Trillium 240**

5.1.2 Acquisition of Ground Motion

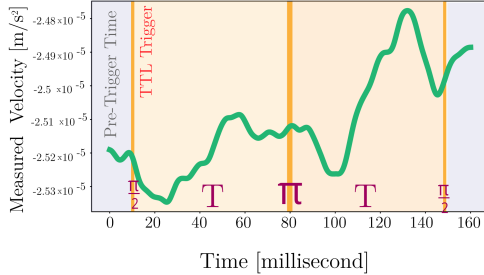


Figure 5.2: An example signal taken from a Trillium 240 measurement. Signal is triggered to acquire at the time corresponding to the first $\pi/2$ of the Mach-Zehnder atom interferometer. Pre-trigger time before the TTL trigger is recorded from the memory buffer of the ADC, along with the sensor signal following the trigger, and is used for phase delay correction.

The acquisition program initiates recording when it receives a TTL from the Realtime-control computer. This TTL is implemented into the atom interferometer control program and timed to the first $\frac{\pi}{2}$ pulse of the MACH-ZEHNDER interferometer. When acquisition is triggered, it also records the time before the trigger which is stored in the memory buffer of the ADC. This data is referred to as pre-trigger samples. Following the last $\pi/2$ pulse of the atom interferometer, we record for an additional length of time. For most measurements, both the pre-trigger and post-interferometer time was set to 20 ms. After recording the signal from the motion sensor during the atom interferometer measurement cycle, the data is written to a hard-disk along with a time-stamp. This process is repeated for every measurement cycle, and when no trigger is received after a given time interval, 5 s, the program closes and the acquisition is complete.

The sensor output from the Trillium 240, Guralp CMG-40T and Titan was directly connected to an analog to digital converter [National Instrument SCB-68] and was not amplified. The Wilcoxon 731A signal was amplified using its proprietary breakout box. With the exception of the Wilcoxon 731A, all sensors must be read out using two pins in a differential configuration, and not simply as a signal measured against ground. This differential configuration minimizes electronic pickup. The pin-out box was read out using a NI PCIe-6353 analog to digital converter (ADC) card. This acquisition card was connected to the control computer through its PCI port.

To interface with the ADC, we utilized the DAQ_MX Python package [82] which was capable of controlling which channels were acquired, the measurement timing, the measurement duration, the sampling rate and the number of pre-trigger samples acquired.

5.1.3 Sensor Response

Sensor	Generator Constant
Trillium	$1196 \text{ m s}^{-1} \text{ V}^{-1}$
Guralp	$400 \text{ m s}^{-1} \text{ V}^{-1}$
Titan	$8.16 \text{ m s}^{-2} \text{ V}^{-1}$
Wilcoxon	$9.81 \text{ m s}^{-2} \text{ V}^{-1}$

Table 5.1: The generator constants for each sensor as stated from their respective user manuals. The *Wilcoxon 731A* has a built-in amplifier in the breakout box, and the generator constant is stated for the $.25g$ configuration of the *Titan*. The *Trillium 240* and *Guralp CMG-40T* output velocity, the *Titan* and *Wilcoxon 731A* output acceleration.

times above the corner frequency $f_{\text{corner}} = 1/2T$ of the interferometer, but below the upper limit of the stated sensor frequency range.

Due to the data load requirements to acquire signal from the motion sensor continuously, we initially opted to record signal from the motion sensor for a finite interval covering the span of the interferometer. The finite duration of the recorded time signal used for inertial post-correction leads to a relatively large spectral resolution, and high-passing the low frequency self noise of the sensor can attenuate valid signal. This phenomena is discussed further in section 5 A.2.1 is known as the **spectral resolution limit** and can hinder the efficiency of post-correction.

Each individual sensor will have a frequency dependent motion-to-voltage response as covered in section A.1.2. Since the amplitude and phase response is flat for all frequencies in the region of interest for atom interferometry, we can use the generator constant for each sensor to calculate the motion from the voltage. The chosen sensitivity of the *Titan* and the amplification on the breakout box of the *Wilcoxon 731A* need to be taken into account when converting from voltage to motion. The output voltage of the seismometers (*Trillium 240* and *Guralp CMG-40T*) correspond to a velocity signal, and the accelerometers (*Titan* and *Wilcoxon 731A*) output an acceleration signal.

5.1.4 Filtering

The internal sensor structure determines the frequency response and the self noise of each motion sensor. This dictates the frequencies the sensor is capable of measuring. However as to be expected, signal from outside of this region is also output from the sensor and will influence post-correction. To correct for this, within the post-correction algorithm we implement digital high and low pass filters. Digital as opposed to analog filters were chosen for flexibility, allowing us to tailor the frequency dependent amplitude and phase response of the filter. Individual filter frequencies were tuned to optimize the post-correction, but in general low-pass filters were chosen with a frequency several

5.1.5 Signal Delay Correction

The mechanical transfer function of the mounting structure, as well the motion sensor phase response will provide a phase delay between when a vibration occurs on the mirror surface and when the signal is output from the sensor. For all sensors used, the phase response is flat for frequencies between 10 mHz-50 Hz, and therefore the signal delay can be compensated by digitally delaying the recorded motion sensor signal relative to the timing of the atom interferometer.

We can determine the value of this signal delay by evaluating the short term stability of the post-corrected data for various delays in signal. In an iterative process, by using the pre-trigger samples we can shift the sensitivity function relative to the measured signal and calculate the phase correction. By optimizing for the lowest short term stability, we can correct for any phase delay of the sensors. The interval step size of the delay was determined analytically based on our data, it was shown that for our measurements a step-size smaller than $\Delta t < 10 \mu\text{s}$ did not make a large difference in post-correction performance. An example of this phase delay correction can be seen in figure 5.3.

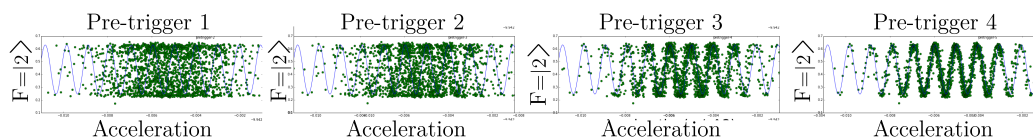


Figure 5.3: Fringe reconstructions calculated for different values for different phase delays. By calculating with a different phase delay, we can minimize the short term stability of the post-corrected phase.

5.1.6 Fringe Reconstruction

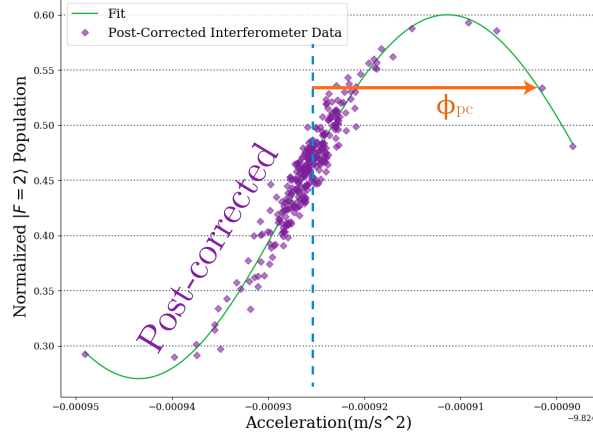


Figure 5.4: We can use the recorded from the motion sensor signal with the the sensitivity function to determine the phase correction from the inertial noise present during the measurement. By applying the phase correction, we can reconstruct the fringe pattern.

Once the signal from the sensor is processed, we sequence the signal from classical motion sensor to match the individual cycle of each measurement. Using the pulse length τ , pulse separation time T , we can calculate the appropriate sensitivity function (section 2.2.1) that matches the sensor output type (velocity or acceleration).

We apply the convolution integral of the sensitivity function with the sensor signal to calculate the phase shift for that atom interferometer cycle. For example, the phase correction using measured signal from an accelerometer $a(t)_{\text{meas}}$, and an acceleration sensitivity function $g_a(t)$, we get equation 5.1.

$$\Delta\phi_{\text{PC}} = k_{\text{eff}} \int_0^{2T+4\tau} a_{\text{meas}}(t) g_a(t) dt \quad (5.1)$$

We then apply the phase correction to the normalized population output of the atom interferometer for each measurement cycle to reconstruct the fringe.

5.2 Atom Interferometer Response and Fitting

Once we obtain a reconstructed fringe from the phase corrections, we can evaluate the fringe to gauge the effectiveness of the post-correction in suppressing vibrations. This is measured by fitting the atom interferometer response to the post-corrected data points to obtain the measured phase.

To fit the reconstructed fringe, we need the atom interferometer response amplitude, frequency, phase and offset. The amplitude is the the fringe contrast C_0 , the frequency is given by the pulse separation time of the atom interferometer. We leave the phase as a free parameter.

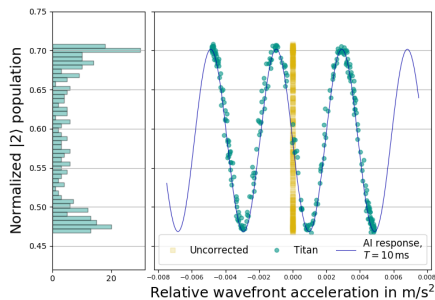


Figure 5.5: Histogram of a 300 measurement cycles of a MACH-ZEHNDER atom interferometer, with the retro-reflection mirror driven with piezos. We can then fit the histogram to determine the offset and fringe contrast, and perform post-correction.

To determine the fringe contrast and offset, we could fit the response of the atom interferometer, although technical noise of the atom interferometer will be added to the fringe contrast of the atom interferometer. In high inertial noise environments, phase noise generated from ground motion will span several fringes, making it difficult to obtain the atom interferometer response by simply scanning the RAMAN detuning sweep-rate α and recording the output population. To obtain a reliable gauge of the contrast of the atom interferometer, we create a histogram of the data normalized $|F = 2\rangle$ population. The non-linear susceptibility of the atom interferometer to inertial noise will generate a bimodal distribution, from which we can determine the contrast C_0 . Driving additional mirror motion with an oscillator, as is done in the simulated high inertial noise measurements,

can distort the bimodal distribution, however fringe contrast and offset can still be obtained.

In the case where the inertial noise is not large enough to span a full fringe, as is the case for low inertial noise measurements taken with the Trillium 240, we first increment the sweep-rate and measure the atom interferometer response.

5.2.1 Evaluation of Post-Correction

Once the fit parameters are obtained, we can fit subsets of the total reconstructed data set to obtain phase information about the post-corrected measurement. This is obtained by binning the total data set set into equal numbers of data points. With the phase as the only free parameter, we then perform a linear least squares regression fit to obtain the fitted phase from each subset. From the fitted phase values, we can use the scale factor to obtain the measured acceleration and compute the ADEV of the total data set.

There are two metrics that we can use to evaluate the performance: the post-corrected short-term uncertainty, and the suppression factor. The former is ideal for low inertial noise environments, and the latter is a better rubric for understanding how well the post-correction performed in a high inertial noise environment. Ideally these two metrics would equally evaluate the post-correction, but

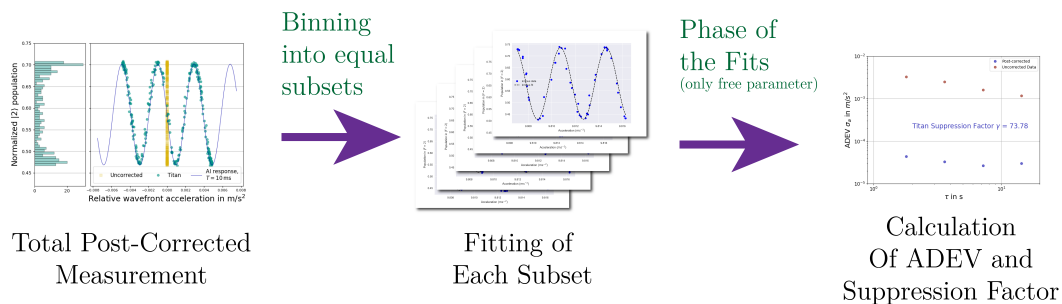


Figure 5.6: From the total data set, we can break the measurement into subsets, from which we fit each data subset and obtain the fitted phase value.

sensor dynamic range, clipping level and sensitivity come into play.

- In lower inertial noise environments, the sensitivity of seismometers to low frequency ground motion is more suited for post-correction.
- In high inertial noise environments, the high dynamic range of accelerometers perform well, but these sensors are not as sensitive as compared to seismometers. The suppression factor is defined as the ratio of the uncorrected phase spread to the post-corrected phase. To obtain the uncorrected phase spread, we calculate the ADEV of the phase corrections calculated from the post-correction integral for each measurement cycle.

$$\gamma = \frac{\phi_{\text{Uncorrected}}}{\phi_{\text{Corrected}}} \quad (5.2)$$

Chapter 5 A

Inertial Noise Post-Correction with Commercially Available Sensors

5 A.1 Measurements of Post-Correction Performance

As has been mentioned in the previous chapter, the implementation of post-correction grants us the ability to reduce inertial noise and obtain meaningful data. We performed inertial noise post-correction with the seismometers `Trillium 240` and `Guralp CMG-40T`; and accelerometers `Titan` and `Wilcoxon 731A` on 3 pulse MACH-ZEHNDER type atom interferometers of varying pulse separation times. These measurements were carried out with the aim of determining the individual advantages or disadvantages of post-correction with different sensors in a given environment.

Tests were performed in two different configurations: low inertial noise environments, where the vibration isolation was enabled, and driven strong motion environments, where the vibration isolation was disabled or extra noise was added via speaker or piezoelectric transducer (PZT). Different sensors performed better within these configurations, and since both low and high noise environments are desirable for atom interferometer post-correction, we will discuss the sensor performance in each configuration.

5 A.1.1 Post-Correction in Low Inertial Noise Environments

Broadband seismometers such as the `Trillium 240` and `Guralp CMG-40T` offer extremely high sensitivity on the order of $\sim 1 \times 10^{-8} \text{ m/s}^2/\sqrt{\text{Hz}}$ in the frequency range $10^{-2} - 50 \text{ Hz}$, but suffer from a low dynamic range and clipping level, which limits post-correction in high-noise low T interferometers. However, these sensors are ideal for a large T atom interferometers which employ vibration isolation. As the pulse separation time increases, the corner frequency f_{corner} decreases, lessening the effect from higher frequency vibrations. Interferometers with extremely large pulse separation times, such as will be possible with the VLBAI experiment[41], will benefit the most from performing post-correction using broadband seismometers.

To determine the effectiveness of broadband seismometers for inertial noise post-correction we placed these sensors on the `Minus-K` vibration isolation platform and performed inertial noise post-

correction on MACH-ZEHNDER type interferometers with pulse separation times of $T = 78$ ms. Between the Trillium 240 and Guralp CMG-40T, the low sensor self noise of the Trillium 240 performed better, so post-correction in a low inertial noise environment will be focused on this sensor.

Post-correction with the Trillium 240

The lowest short-term uncertainty reached after post-correction was performed with the Trillium 240 on a MACH-ZEHNDER style atom interferometer with pulse separation time $T = 78$ ms. For this measurement, the retro-reflection mirror was connected to the Trillium 240 via a custom mounting structure¹. The measurement was performed with the vibration isolation enabled to accommodate the low clipping level of the broadband sensor. The linear sweep rate of the RAMAN detuning was set to a mid-fringe position. 300 measurement cycles were taken with an average cycle time $T_c = 2.3$ s. During each measurement cycle, we recorded the velocity signal for a total of 196.03 ms from the Trillium 240 with a sampling rate of 10^5 samples per second.

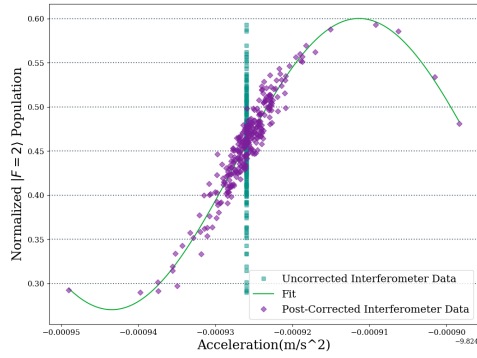
After the measurement was complete, the voltage signal was converted to velocity using the $1196 \text{ m s}^{-1} \text{ V}^{-1}$ generator constant. We implemented a digital IIR low-pass filter of 23 Hz, giving us signal up to roughly 3 times the corner frequency of the MZI ($f_{\text{corner}} = 6.41$ Hz), yet well below the sensors upper frequency range of the sensor $f_{\text{UpperTr}} = 50$ Hz. We used the measured Trillium 240 signal to perform inertial post-correction on the normalized $|F = 2\rangle$ population output of each interferometer cycle. The phase corrections were applied, and the fringe was reconstructed, see figure 5 A.1a. Ground motion was not large enough to equally distribute points in a manner where a histogram could be applied to determine fringe contrast, so before the mid-fringe measurement we scanned the sweep-rate to measure the atom interferometer response. We then binned the total 300 measurement data set into subsets of 5 measurement cycles and fit a sine to the data points; from which we obtained the phase.

we calculated the short term uncertainty of the uncorrected atom interferometer was $\sigma_{\text{UPC}} = 4.4 \times 10^{-6} \text{ m/s}^2/\sqrt{\text{Hz}}$. From the ADEV of the phase corrections, we reached a short term uncertainty of $\sigma_{\text{PC}} = 9.2 \times 10^{-7} \text{ m/s}^2/\sqrt{\text{Hz}}$, yielding a suppression factor of $\gamma = 5.4$. The post-correction performance is limited by the self noise of the motion sensor (both electronic and environmental) below the measurement cycle frequency $f_{\text{cycle}} = 0.55$ Hz. This sensor self noise below the cycle frequency cut-off corresponds to an acceleration noise of $1.2 \times 10^{-6} \text{ m/s}^2/\sqrt{\text{Hz}}$.

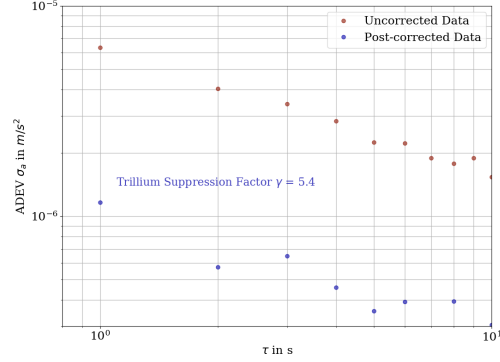
5 A.1.2 Post-Correction in a Simulated High Motion Environments

The high sensitivity at low frequencies makes broadband seismometers well suited for post-correction of MACH-ZEHNDER type interferometers with large pulse separation time. However, in high inertial noise environments, the high dynamic range and high clip level of accelerometers is more capable. Post-correction measurements with the accelerometers were taken with the vibration isolation disabled in a ‘strap-down’ configuration, further the highest suppression factor was obtained by

¹The domed roof of the Trillium 240 was designed to help aid stability in changes of barometric pressure. However, this domed top made connection to the retro-reflection mirror difficult. The retro-reflection mirror could not simply be placed onto the top of the Trillium 240, and the sensor cannot be inverted. More details about the mounting structure will be discussed in section 5 A.2.5



(a) The Reconstructed Fringe



(b) ADEV of Phase

Figure 5 A.1: (*Left*) The reconstructed fringe calculated from the post correction of a 300 cycle $T = 78$ ms atom interferometer. The total data set is split into equal subsets and fit determined by the atom interferometer response parameters; from which the phase is extracted. (*Right*) The ADEV of the obtained phase is compared with the uncorrected acceleration RMS to determine the suppression factor.

simulating a strong motion environment using the the **Titan** with additional motion added by piezoelectric transducer (PZT).

Nanometrics Titan

For this measurement the retro-reflection mirror was attached directly to the top of the **Titan** using ceramic glue. The **Titan** with the attached retro-reflection mirror was placed onto the vibration isolation platform and aligned to overlap with the incoming RAMAN beam. The internal sensitivity setting of the **Titan** was set to $.25g$. External noise was introduced from three PZT placed under the legs of the **Titan**². These PZTs were driven at 350 Hz with a driving voltage of 20 V.

A three pulse MACH-ZEHNDER type interferometer with pulse separation time $T = 10$ ms was performed at a fixed sweep-rate α that corresponded to a mid-fringe position. 300 MZI cycles were measured with an average measurement cycle time $T_c = 2.7$ s. During each measurement cycle 60.03 ms of signal from the **Titan** was measured with a sampling rate of 10^5 samples per second. We then used the titan generator constant, $K_{\text{Titan}} = 8.16 \text{ m s}^{-2} \text{ V}^{-1}$ to convert the measured voltage into an acceleration signal. We then implemented a digital high-pass filter³ of 0.3 Hz and performed a low pass filter of 400 Hz. From this filtered data, we performed the post-correction integral to obtain the phase correction. We applied the phase correction and reconstructed the fringe pattern, figure 5 A.2a.

The induced motion, generated phase corrections that spanned several fringes, allowing us to determine the offset and contrast by taking a histogram of population. The entire data set was

²A full description of PZT placement is shown in section 5B.3

³This is where the high-pass filter was set, but due to the spectral-resolution limit, the filter was actually 16.6 Hz. The reasoning for this is discussed in section 5 A.2.1.

split into a subsets of 10 measurements, the phase was extracted from the fringe fit of each subset. From the extracted phase we calculate the post-corrected short-term uncertainty and suppression factor. From the spread of the phase corrections, we calculated an uncorrected short term uncertainty of $\sigma_{\text{UPC}} = 7.4 \times 10^{-3} \text{ m/s}^2/\sqrt{\text{Hz}}$. We calculated a post-corrected short term uncertainty of $\sigma_{\text{PC}} = 1.0 \times 10^{-4} \text{ m/s}^2/\sqrt{\text{Hz}}$, yielding a suppression factor of $\gamma = 73.8$. The limitation of the post-correction in this case was the spectral resolution limit, calculated to be $1.9 \times 10^{-4} \text{ m/s}^2/\sqrt{\text{Hz}}$ for this measurement.

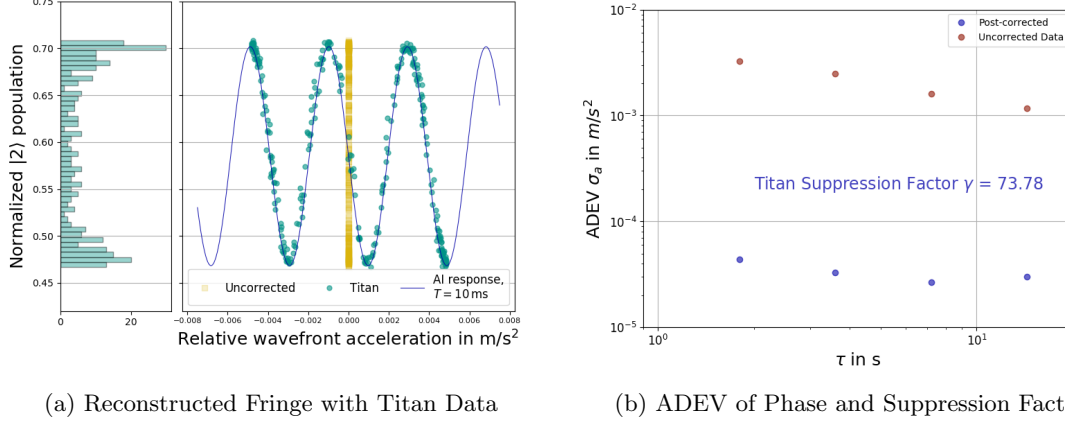


Figure 5 A.2: (*Left*) The point spread function of the population data and the reconstructed fringe of the entire data set. Since the mirror was driven with piezos, the population distribution does not follow a bimodal distribution (*Right*) The ADEV of the post-corrected phase is compared with the uncorrected phase spread to determine the suppression factor.

5 A.2 Limitations to Gravimetry

In this section we will cover the current limitations to inertial post-correction, as well as the other effects that affect post-correction. Post-correction was either limited by the spectral resolution limit sensor or self noise generated from sensor electronics and environmental effects. Due to the finite length of motion sensor signal recorded, the frequency resolution of each post-correction measurement is large. This large spectral resolution limits the placement of high-pass filters used to filter the low frequency sensor drifts. Depending on the measurement, implementing a high-pass filter could, due to the large frequency resolution, attenuate valid signal for post-correction along with low frequency self noise. The self noise and spectral resolution limit was evaluated for each measurement, which determined whether or not high-pass filtering was implemented.

Table 5 A.1: A table of the current limitations of gravimetry for the $T = 10$ ms high noise **Titan** measurement and the $T = 10$ ms low inertial noise **Trillium 240** measurement. The ‘Total Inertial Noise’ represents the unpost-corrected inertial noise affecting the atom interferometer, below the limitation to post-correction is either determined by the spectral resolution limit or the self noise of the motion sensor. This is determined by whether or not the signal from the sensor was high-pass filtered, which is determined by the sensor and measurement pulse separation time. The lower limitation of the two is shown in bold.

Measurement	High Noise Titan	Low Noise Trillium 240
Total Inertial Noise	8.9 rad/ $\sqrt{\text{Hz}}$	450 mrad/ $\sqrt{\text{Hz}}$
- Motion Sensor Self Noise	2.0 rad/ $\sqrt{\text{Hz}}$	100 mrad/$\sqrt{\text{Hz}}$
- Spectral Resolution Limit	304 mrad/$\sqrt{\text{Hz}}$	448 mrad/ $\sqrt{\text{Hz}}$
Raman PLL Noise	40 mrad/ $\sqrt{\text{Hz}}$	35 mrad/ $\sqrt{\text{Hz}}$
Sensor Alignment Noise	24.0 mrad/ $\sqrt{\text{Hz}}$	1.4 mrad/ $\sqrt{\text{Hz}}$
Quantum Projection Noise	7.7 mrad/ $\sqrt{\text{Hz}}$	4.4 mrad/ $\sqrt{\text{Hz}}$

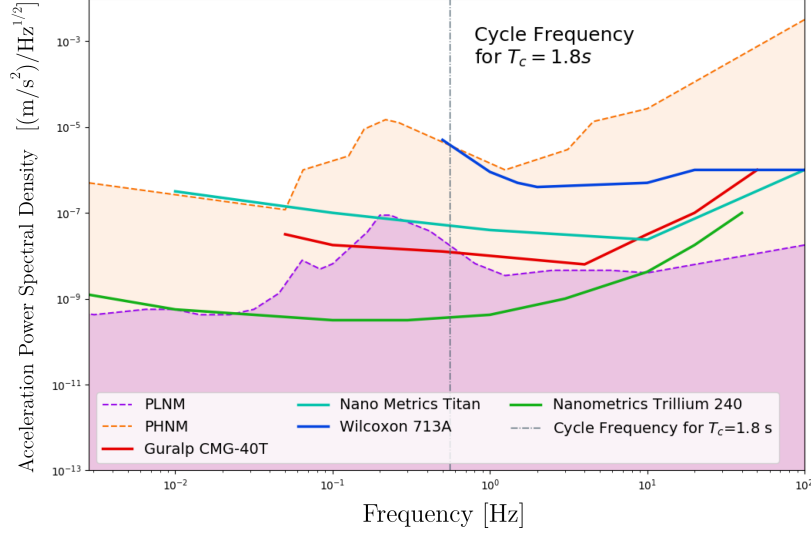


Figure 5 A.3: The self noise of each of the 4 motion sensors as either stated by the manufacturer or published. The PETERSON low and high noise is shown for reference. The blue dashed line represents the cycle frequency for a $T_c = 1.8\text{s}$ atom interferometer. Self noise is plotted for the frequency operational range stated by the manufacturer, however electronic signal from outside this region is present.

5 A.2.1 Self Noise and Spectral Noise Limitation

As mentioned previously, the ultimate limit to post-correction with a sensor is the sensor's self noise. This self noise has a frequency dependence and is specific to the individual sensor, and is defined in this work to incorporate not only the electronic noise of the test mass read-out, but also drifts caused by sensor environmental susceptibility to factors such as pressure and temperature. Sensor self noise can be measured by grouping multiple sensors of the same type and performing a huddle-test [83, 84].

Although these sensors are stated to perform for a given frequency range, they are not usually internally filtered and therefore output signal at frequencies outside of their measurement capabilities. This signal, if not filtered, will add a non-physical contribution to the post-correction. Signal below the cycle frequency of the interferometer is interpreted as atom interferometer signal, and should not be post-corrected. Additionally if not internally filtered, the self noise of the sensor increases at lower frequencies. This low frequency noise is a result of the aforementioned temperature and pressure variations that affect the sensor over time.

We calculated the contribution of sensor signal from below the cycle frequency by taking a 30 minute measurement of the **Trillium 240** and **Titan** in their respective measurement setup, from which we calculate the power spectral density of each of the sensors. From the power spectral density, we can use equation 4.9 integrating from from $\text{DC} - \omega_c$ (where $\omega_c = 2\pi f_c$) to calculate the RMS

phase contribution from the unfiltered sensor self noise below the cycle frequency $\tilde{\phi}_{\text{Self}}^{\text{RMS}}$, giving us equation 5 A.1.

$$(\tilde{\phi}_{\text{SN}}^{\text{RMS}})^2 = \int_0^{\omega^c} |H_\phi(\omega)|^2 S_a(\omega) d\omega \quad (5 \text{ A.1})$$

For the simulated strong motion **Titan** measurement, the unfiltered sensor contribution is $\tilde{\phi}_{\text{SN Titan}}^{\text{RMS}} = 2.05$ rad and for the low inertial noise **Trillium 240** measurement, the self noise contribution is $\tilde{\phi}_{\text{SN Trillium}}^{\text{RMS}} = 100.4$ mrad.

Spectral Resolution Limit

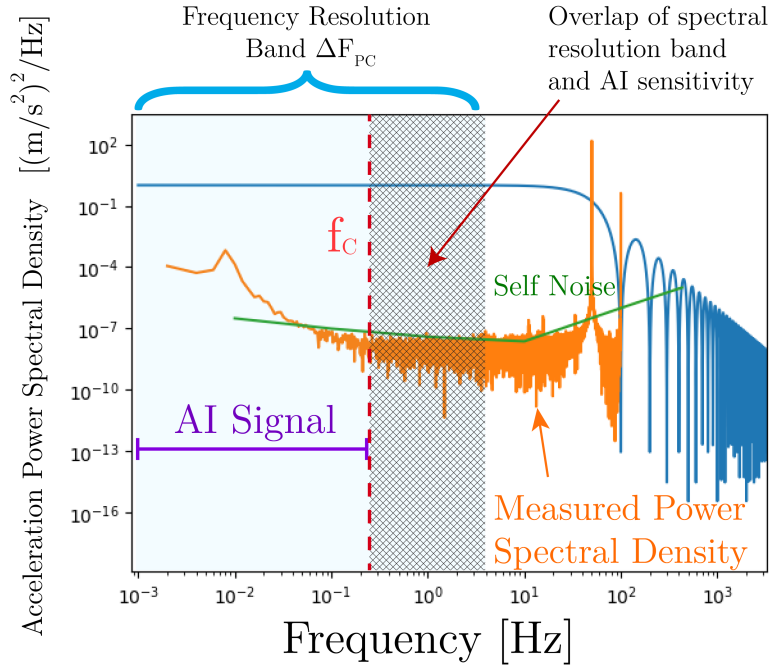


Figure 5 A.4: Power spectral density of the **Trillium 240** from a 30 minute background measurement. For the low inertial noise measurement the cycle frequency is $f_c = 0.55$ Hz; anything measured below this limit is atom interferometer signal, and therefore must be filtered from the sensor.

With the post-correction algorithm, we measure a time-series signal to post-correct the noise occurring during that specific measurement cycle. We can define this finite temporal duration as ΔT_{PC} , which for our post-correction measurements, $\Delta T_{\text{PC}} = 2T + 4\tau + t_{\text{pre-trigger}} + t_{\text{Post-AI}}$. The finite temporal duration⁴ of the recorded signal from the sensor, gives us a frequency resolution, ΔF_{PC} , equation 5 A.2. The temporal-spectral uncertainty relation in signal processing theory is

⁴As mentioned in section 5.1.4, the limited duration of measurement was a requirement for data acquisition and processing.

given the name 'the GABOR Limit' [85], and follows similar principles as the uncertainty principles used in physics.

$$1 \leq \Delta T_{PC} \cdot \Delta F_{PC} \quad (5 A.2)$$

For a $T = 78$ ms MACH-ZEHNDER atom interferometer, the total length of the recorded signal is $\Delta T_{PC} = 196.03$ ms yielding a frequency resolution of $\Delta F_{PC} \geq 5.1$ Hz.

As mentioned above, low frequency signal drifts from the motion sensor must be filtered or will contribute additional noise to the post-correction measurement. However by high-pass filtering the signal with such a large frequency resolution we cannot discern between the signal and the noise within this frequency block ΔF_{PC} . In the $T = 78$ ms atom interferometer, all signal below 5.1 Hz cannot be spectrally resolved. However, due to the spectral resolution, when high-pass filtering the data within the frequency band, $DC - F_{PC}$ will be attenuated. For example for the $T = 78$ ms atom interferometer, this means that data below spectral resolution limit, $\Delta F_{PC} = 5.1$ Hz is attenuated along with the self noise. With an average $T_c = 1.8$ s our cycle frequency $f_c = 0.55$ Hz meaning that 9 cycle-frequency sampled data points are filtered along with the self noise of each sensor.

A longer measurement of the signal from the motion sensor will increase the spectral resolution, allowing for the ability to more finely place the high-pass filter. However, the maximum T_{PC} limitation would be the cycle time T_c , at which point the frequency resolution ΔF_{PC} would be equal to f_c . This represents a fundamental limitation to the post-correction technique; the segmented nature of the process restricts spectral resolution. To increase the frequency resolution to below the cycle frequency, we need to continuously measure signal from the motion sensor.

To determine the effect of this limitation on the measurements taken above, we can simulate the uncorrected inertial noise from frequencies that are attenuated when high-pass filtering. We measured S_a ⁵ for each sensor by taking a 30 min measurement of the ground motion with a sampling rate of 200 Hz, from which we calculated the inertial noise contribution for using equation 5 A.3.

$$\sigma_{\phi}^2_{SLR}(\tau) = \frac{k_{\text{eff}}^2}{\tau} \sum_{n=1}^{N_{\text{window}}} \frac{|H_{\phi}(2\pi n f_c)|^2}{(2\pi n f_c)^4} S_a(2\pi n f_c) \quad (5 A.3)$$

Where N_{window} is the number of interferometer cycle-frequency data points between f_c and F_{PC} .

For the simulated strong motion background measurement, this phase contribution from performing a high-pass filter with the spectral resolution limitation (SRL) was $\sigma_{\phi}^{\text{Titan}}_{SRL} = 304.3$ mrad; for the **Titan** and $\sigma_{\phi}^{\text{Trillium}}_{SRL} = 447.7$ mrad for the **Trillium 240**.

High-pass Filtering and Post-Correction

Measurement	High Noise Titan	Low Noise Trillium 240
Sensor Self Noise	2.0 rad/ $\sqrt{\text{Hz}}$	100 mrad/$\sqrt{\text{Hz}}$
Spectral Resolution Limit	304 mrad/$\sqrt{\text{Hz}}$	448 mrad/ $\sqrt{\text{Hz}}$

This means for each sensor we need to decide whether or not to implement a high-pass filter. In the case of the **Trillium 240**, the spectral resolution limited phase contribution was higher than

⁵For the **Trillium 240**, we actually measure the velocity power spectral density, but we can convert from velocity PSD to acceleration PSD using the relation $S_a(\omega) = \omega^2 S_v(\omega)$.

the self noise contribution so we did not implement high-pass filtering. However, in the case of the *Titan*, the self noise was higher than the spectral resolution limit, so we implemented high-pass filtering.

In either case, the limited duration of signal measurement was the underlying contribution to the limiting the post-correction. This can be addressed in the future by implementing measurements where signal from the motion sensor would continuously be recorded. High-passed data above the cycle frequency could be used for post-correction and signal from below the cycle-frequency would be recorded from the atom interferometer. The continuous measurement from the motion sensor would allow for much finer frequency resolution, and allow for high-pass filters to be placed directly at the cycle frequency.

5 A.2.2 Alignment Noise of the Sensor

As discussed in section 3.1.2, the RAMAN beam is aligned parallel to the local gravitational acceleration. The retro-reflected beam is aligned by changing the weight distribution on the vibration isolation platform so that the retro-reflection beam is aligned to the incoming beam. It is possible for the retro-reflection mirror to be aligned to the axis of gravitational acceleration, but for the sensor not to be. This misalignment is possible if the underside of the retro-reflection mirror is not flush with the surface of the sensor, thus creating an angle.

The motion sensor signal is measured from the \hat{z} axis, and misalignment of the sensor relative to the RAMAN beam will influence the correlation of the atom interferometer with the motion sensor. Additionally, misalignment of the sensor's \hat{z} axis relative to the RAMAN beam will be picked up by the other vertical sensor axes.

To simplify the problem, we will illustrate this in two dimensions. The angle between the sensor's \hat{z} axis and the gravitational acceleration \vec{g} is given by the angle θ , which is constant over time ($\frac{d\theta}{dt} = 0$). For a given angle θ we lose signal from the \hat{z} axis and gain signal from the un-correlated \hat{x} axis. We can model the noise of misalignment using equation 5 A.4.

$$(\tilde{\phi}_{\text{Alignment}}^{\text{RMS}})^2 = (\tilde{\phi}_{\text{Vib}}^{\text{RMS}})^2 - (\tilde{\phi}_{\hat{z}}^{\text{RMS}})^2 \cos^2(\theta) + (\tilde{\phi}_{\hat{x}}^{\text{RMS}})^2 \sin^2(\theta) \quad (5 \text{ A.4})$$

We can calculate the contribution from alignment by using the spread of interferometer points to calculate $\tilde{\phi}_{\text{Vib}}^{\text{RMS}}$, and measuring the power spectral densities $S_a^z(\omega)$ and $S_a^x(\omega)$ to calculate the $\tilde{\phi}_{\hat{z}}^{\text{RMS}}$ and $\tilde{\phi}_{\hat{x}}^{\text{RMS}}$ using equation 5 A.5.

$$(\tilde{\phi}_{\hat{x}}^{\text{RMS}})^2 = k_{\text{eff}}^2 \int_0^\infty \frac{1}{\omega^4} |H_\phi(\omega, T)|^2 S_a^x(\omega) d\omega \quad (5 \text{ A.5})$$

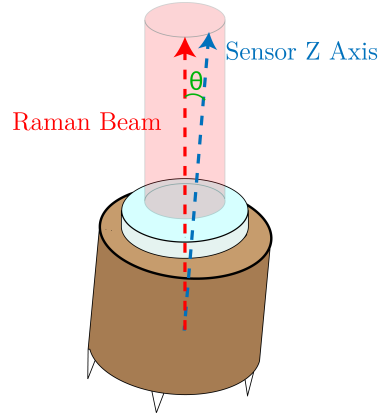


Figure 5 A.5: It is possible for the retro-reflection to be aligned, but the sensor not to be.

We measured an upper bound of the maximum angular tilt $\theta < 0.15^\circ$. We then calculate an alignment noise contribution of 1.4 mrad for the Trillium 240 and 24.0 mrad for the Titan. This noise source is not limiting, although to reduce this contribution we can measure signal from all three axis and calculate the sensor orientation that maximizes the post-correction.

5 A.2.3 Raman Phase lock loop

As mentioned previously, any uncommon phase shift between the incoming and retro-reflected beams cannot be discerned from a gravitational acceleration. In our case, light for the RAMAN Master and RAMAN Slave is generated by separate source lasers. Uncommon frequency drifts of the laser, or differential phase shifts due to index of refraction changes will change the relative phase between the beams. To address this problem, we implement a phase-lock loop (PLL) which is designed to keep the phase relative to the two laser constant.

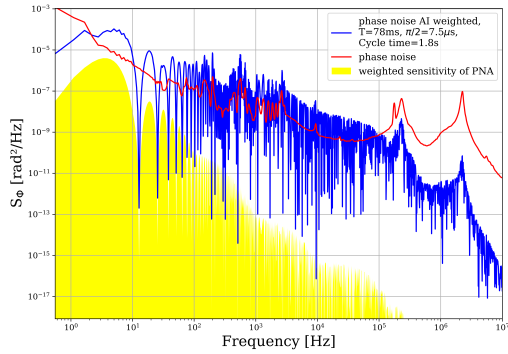


Figure 5 A.6: The phase noise analyzer output weighted by the interferometer transfer function for a $T = 78$ ms atom interferometer.

For the low inertial noise measurements with a $T = 78$ ms we measure a phase noise of $\tilde{\phi}_{\text{PLL}} = 40.24$ mrad, and $\tilde{\phi}_{\text{PLL}} = 34.87$ mrad for our for $T = 10$ ms high inertial motion measurements.

The source of this noise is the large uncommon path between the two lasers after the lock. The light from each source laser enters independent fibers and passes through independent optics before being overlaid. Ideally the phase lock between the two beams would be locked as closely as possible to the RAMAN collimator. This can be implemented in the future, but currently would require a major redesign and reconstruction.

5 A.2.4 Synchronous Noise Due to Magnetic Field Sensitivity

Dynamic magnetic fields generated by the switching of the magnetic field coils can affect the test mass position of the motion sensor. This change in test mass position will simulate motion and occurs in sync with the atom interferometer [86], causing a constant systematic phase shift for

To measure the contribution from this effect on our post-correction, we measured the phase noise of the beat between the RAMAN Master and Slave at the point where the beams enter the RAMAN collimator. Light from both the Master and Slave was coupled into a fiber at the end of which we placed a photo-diode. We can measure the phase noise of the beat between the RAMAN Master and Slave on the photo-diode using a phase noise oscillator [Rohde & Schwarz FSWP8] which is internally referenced to a stable 10 MHz OCO oscillator. From which we obtained the phase noise power spectral density. We can then use the atom interferometer transfer function to calculate the to calculate the RMS phase contribution from this lock.

For the low inertial noise measurements with

all post-corrections. In our experiment a μ -metal magnetic shield separates the field coils from the post-correction sensors, but nonetheless we can analyze our data to determine if this effect is present.

For an N cycle measurement, with M data points per measurement cycle, we will have a total measurement array u , with each element u_{nm} representing one measured signal voltage from the sensor.

$$u = \begin{bmatrix} u_{11} & u_{12} & u_{13} & \dots & u_{1M} \\ u_{21} & u_{22} & u_{23} & \dots & u_{2M} \\ \vdots & \vdots & \vdots & \ddots & \vdots \\ u_{N1} & u_{N2} & u_{N3} & \dots & u_{NM} \end{bmatrix} \quad (5 \text{ A.6})$$

Each column represents the same temporal location in the measurement sequence, and any synchronous noise present will be common to each column. We can then calculate the column-wise mean value of the measurement signal to accumulate any synchronous effect over the entire measurement into one row vector \bar{u}_m .

$$\bar{u}_m = \frac{1}{N} \sum_{n=1}^N u_{nm} \quad (5 \text{ A.7})$$

We can then calculate the normalized covariance or PEARSON coefficient, for each measurement cycle with the corresponding mean signal, equation 5 A.8.

$$r_n = \frac{\text{Cov}(u_{nm}, \bar{u}_m)}{\sqrt{|u_{nm}| \cdot |\bar{u}_m|}} \quad (5 \text{ A.8})$$

Where $\text{Cov}(u_{nm}, \bar{u}_m)$ is the covariance the vectors of the n th measurement cycle with the mean signal \bar{u} . This leaves us a column vector r_n of how each measurement cycle correlates to the mean signal. We can then compute a histogram of these PEARSON coefficients for each measurement cycle. If synchronous noise is present, we will have high correlation between the mean signal and the measurement cycle ($r_n > 0.75$).

We then performed this calculation on a 300 point Trillium 240 measurement taken in the low noise configuration, and saw an even distribution of PEARSON coefficients (figure 5 A.7), but no occurrences of $r_n > 0.75$. This implies that our measurements are likely not affected by synchronous noise.

In the future as gravimeters become smaller and motion sensors become more compact, this effect could play a larger role. This highlights one advantage of the OMIS sensor which is optically read-out and insensitive to magnetic field coil switching.

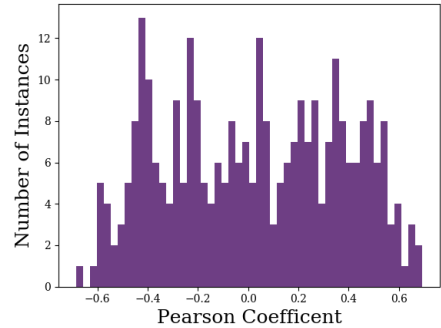


Figure 5 A.7: A histogram of the PEARSON coefficients of 300 measurement cycles measured with the Trillium 240 in the low inertial noise configuration. Each measurement cycle was correlated with the mean the mean signal \bar{u} .

5 A.2.5 The Mechanical Transfer Function

For each motion sensor we require a mounting structure that connects the retro-reflection mirror to the sensor. The reference point for post-correction is the mirror's surface, and any phase delay or magnitude attenuation that occurs between the mirror's surface and the sensor's test mass will affect the efficiency of post-correction. This change in signal magnitude and phase can be described by the system's mechanical transfer function.

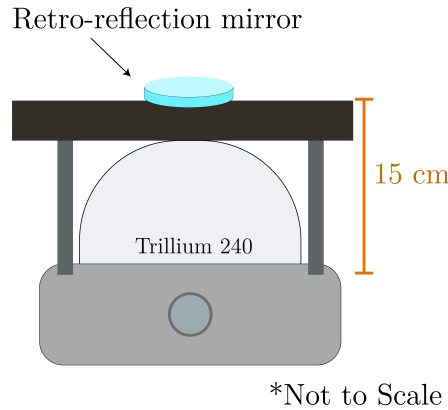


Figure 5 A.8: To take the Trillium 240 as an example, the sensor's top was designed to combat the effects of changes in atmospheric pressure, however this prevented mounting of the retro-reflection mirror to the Trillium 240. The reference point of the sensor is the bottom, and the device cannot be inverted. We attached 15 cm rigid aluminum posts to screws that attached to the base of the Trillium 240 and place a square aluminum plate on top of these posts. From which, we can place the retro-reflection mirror.

The effect of the mechanical transfer function on post-correction is difficult to measure due to the fact it has less of an effect on the post-correction than the spectral resolution limit. As the spectral resolution problem is resolved, the transfer function is potentially a source of limitations. This transfer function reflects the general problem of measuring with commercial devices; they are not designed for use within the context of atom interferometry. The resolution to this problem is one of the main advantages of the all-optical OMIS sensor, which can be directly integrated into the center of mass of the inertial reference.

Chapter 5B

Opto-mechanical resonator enhanced atom interferometry

5B.1 Inertial Sensing with an opto-mechanical resonator

Recent developments in the design and creation of opto-mechanical resonators [87] show promise for experiments capable of testing fundamental physics [88, 89, 90], applications in quantum information theory [91, 92], and even use in biology [93]. These resonators offer a nascent link between macroscopic devices and coherent quantum systems.

The techniques and principles developed in these experiments have inspired the development of a macroscopic opto-mechanical resonator capable of measuring acceleration. The optomechanical inertial sensor (OMIS) is a compact device [32, 94] capable of measuring displacement and acceleration of a harmonic oscillator through the use of optical interferometry. The device's small form factor allows for easy integration into inertial references. The OMIS does not contribute a temperature gradient, and therefore may be placed near atomic sources without contributing a black-body attraction [95]. The device's insensitivity to magnetic and electric fields allow placement near field coils or chip field wires, without fear of said fields affecting the test mass position. The sensor design and construction is bespoke, and the mechanical resonance and measurable bandwidth can be adapted to the specific environment needed. Lastly the vacuum compatibility and lack of electric or magnetic field emission means it can be placed in close proximity to an atom chip, making it ideal for miniaturization efforts (section 6.3).

All of these unique features form an accelerometer that is more capable for use in an atom interferometer when compared to traditional motion sensors. Yet, these devices have hitherto not been employed in the post-correction of atom interferometers. The focus of this chapter will be on the introduction, operating principles and application of these sensors to atom interferometers for the use of vibration post-correction.

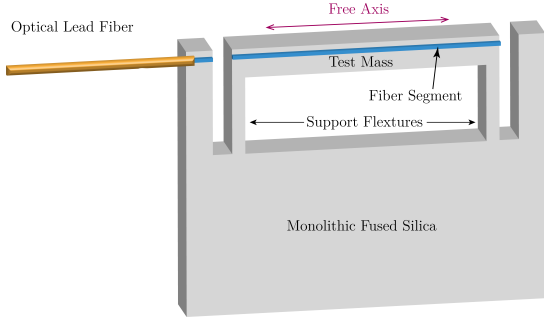


Figure 5B.1: A Schematic of the OMIS, the full setup with integration into the atom interferometer is shown in figure 5B.4.

The OMIS is constructed with a base of monolithic fused silica, with a free moving test mass connected with two support flexures (Fig. 5B.1). The flexures allow the test mass to move along one axis and suppress motion along the other axes. Parallel to the direction of motion, a flat-cleaved optical fiber segment is bonded within V-grooves of the test mass. A second optical fiber known as the lead fiber is flat-cleaved on one end and attached to the fused silica mass. The flat-cleave side of the lead fiber is aligned to face the fiber segment within the test mass; the other end of the lead fiber allows light to enter the lead fiber with an APC connector. The lead fiber is aligned to form an optical cavity between the lead fiber tip and the fiber tip of the segment contained within the test mass. The cavity length of the fiber tips is sensitive to displacement of the test mass and may be optically read out by measuring the intensity of the reflected light from the cavity. We can then use the mechanical transfer function of a harmonic oscillator to convert this displacement to acceleration.

5B.2 OMIS Theory

A displacement of the OMIS test mass will result in a change of the cavity length formed between the two fiber tips. As stated above, we can optically interrogate this cavity to determine changes in displacement of the test mass. The test mass of the OMIS is constrained by the support flexures can be approximated as a damped harmonic oscillator and can be modeled by the differential equation, equation 5B.1.

$$\frac{d^2x}{dt^2} + Q\omega_0 \frac{dx}{dt} + \omega_0^2 x = 0 \quad (5B.1)$$

Where Q is the mechanical quality factor, and ω_0 is the mechanical resonance of the oscillator. The solution to this differential equation gives us the transfer function, equation 5B.2.

$$\frac{|X(\omega)|}{|A(\omega)|} = \frac{1}{\omega_0^2 - \omega^2 + i\omega\omega_0/Q} \quad (5B.2)$$

This mechanical transfer function gives us a relation between the test mass displacement and an acceleration. This cavity follows a FABRY-PEROT cavity response[96]. We can then calculate the optical response of the OMIS to motion by calculating how a change in cavity length affects the reflected response for a cavity with length L , reflectivity R , incoming laser wavelength λ_0 and small test mass displacement Z_m , equation 5B.3.

$$I_r(\lambda) = I_{\text{offset}} + I_{\text{contrast}} \left(\frac{(1+R)^2}{2} \left[\frac{1 - \cos(\frac{4\pi}{\lambda} Z_m)}{1 + R^2 - 2R \cos(\frac{4\pi}{\lambda} Z_m)} \right] \right) \quad (5B.3)$$

The reflectivity of the uncoated fiber tips in our setup is roughly 4%, giving us a finesse, $\mathcal{F} \approx 2$, and therefore the response can be approximated as sinusoidal with respect to wavelength. By choosing a wavelength λ that corresponds to a mid-fringe position of the optical response, a linear change in the cavity length will correspond to a linear change in the reflected response, equation 5B.4.

$$\frac{dZ_m}{Z_m} = \frac{d\lambda}{\lambda}. \quad (5B.4)$$

To be able to compare the OMIS to the generator constant of the commercial devices (section 5.1) it will be compared with, we can cast the reflected optical response is given in terms of a measured voltage from a photo detector V_r . With this and the equation 5B.3 we can calculate how a test mass displacement corresponds to a change in voltage, equation 5B.5.

$$\Delta V_r(z) = \Delta Z_m \frac{\lambda_0}{L} \left(\frac{dV}{d\lambda} \right) \Big|_{\lambda_{\text{midfringe}}} \quad (5B.5)$$

where $dV/d\lambda$ is change voltage with respect to the wavelength of the light. Lastly we can use equation 5B.2 to convert our cavity displacement Z_m for the general displacement X into an acceleration as a function of change in voltage, 5B.6.

$$\Delta V_r(z) = \Delta a \frac{|X(\omega)|}{|A(\omega)|} \frac{\lambda_0}{L} \left(\frac{dV}{d\lambda} \right) \Big|_{\lambda_{\text{mid-fringe}}} \quad (5B.6)$$

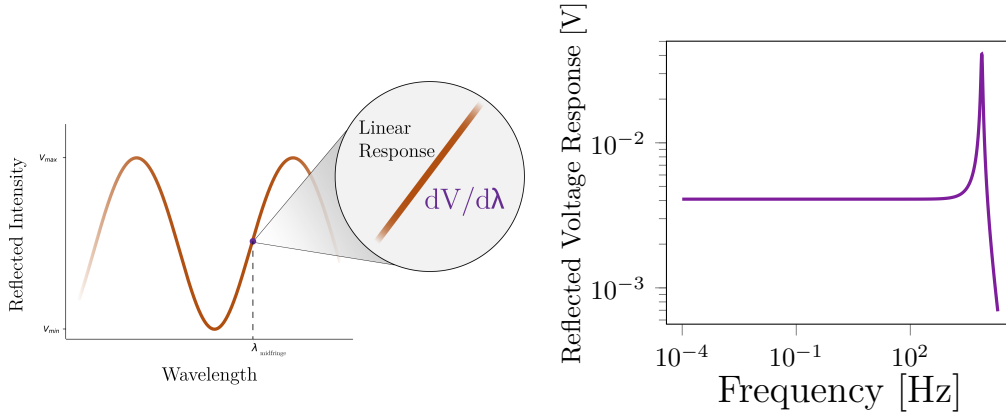


Figure 5B.2: *Left*. The optical response of a low finesse cavity. At a wavelength corresponding to a mid-fringe position, a change in length or wavelength is linearly proportional to the reflected light from the cavity. *Right*. The voltage response for an acceleration of 1 m s^{-2} OMIS 2 at port 3 (figure 5B.3) as a function of frequency for our setup. This was calculated for the measured parameters (section 5B.4) of the setup using eq. 5B.6

5B.3 Experimental Setup

Optical Setup

To show post-correction with a compact optical system, all components in this setup are fiber coupled.

The source laser for OMIS post-correction was a low noise narrow line-width [NKT Photonics Koheras ADJUSTIK] laser. Light generated from the source laser was sent through a fiber isolator, and then passed into an fiber-based optical circulator. After the fiber isolator, we send the light into port 1 of the circulator, which is sent out of port 2 where it is coupled into the OMIS cavity. Light reflected from this cavity then re-enters port 2, which is then transmitted to port 3. We then measure the optical power at the output of port 3 with a fiber coupled photo detector [Thorlabs DET10].

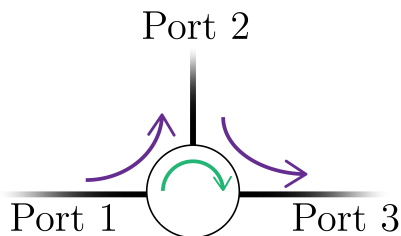


Figure 5B.3: The optical circulator has three ports, labeled: port 1, port 2 and port 3. Light sent into port 1 will travel to port 2. Light sent into port 2 will be transmitted to port 3. Light entering port 2 will experience an attenuation of > 50 dB towards port 1. Light sent into port 1 will similarly be heavily attenuated towards port 3, and light entering port 3 will also be attenuated towards port 2 or port 3.

During operation with the NKT laser, roughly ≈ 8 mW enter port 1, of which, ≈ 200 μ W exit port 3. This voltage is then bandpass filtered with frequencies: 0.33 Hz - 10.6 kHz. The filtered voltage is amplified by a factor of 1000 with a [DLPCA-200] low noise amplifier. This amplified signal is then sent to a [National Instrument SCB-68] pin-out box and read off with a [NI PCIe-6353] 16-bit analog to digital converter (ADC). We interface with the card using the NI-DAQMx Python library. The acquisition of the signal is synced with the atom interferometer using a TTL pulse generated by the control matrix, ensuring that acquisition is started concurrently with the interferometer. The measured voltage is then recorded and stored for later processing.

Mechanical Setup

For seismic post-correction, we are interested in the motion of mirror surface. The small form factor of the OMIS allows us to attach the OMIS to the side retro-reflection mirror. This was achieved by attaching the side perpendicular to the measurement axis to one side of a square 2 inch retro-reflection mirror with Torr seal. The lead fiber of the OMIS is supported using scaffolding, which is offset from the RAMAN beam. To reduce mechanical coupling of vibrations on the platform to the fiber, insulating foam was added around the fiber and the support structure. However, low frequency vibrations still mechanically couple to the fiber¹, causing fluctuations in the response the OMIS measurements. For this reason, with the first generation OMIS, low frequency vibrations on the lead fiber prevented us from performing strap down post-correction; where post-correction is performed on the intrinsic background vibrations. Because of this, all measurements of inertial post-correction with the OMIS were performed on a

¹A full discussion of the source and effect of this will be discussed in section 5B.6.3

vibration isolation platform to attenuate the low frequency component of ground motion, at which point, inertial noise higher than the mechanical coupling resonance of the lead fiber (measured to be $f_{\text{drive}} > 260$ Hz for OMIS 1, Fig. 5B.15) was introduced through the use piezoelectric transducers (PZT).

To measure the performance of the OMIS in comparison to other sensors, we attached a **Titan** beneath the retro-reflection mirror with ceramic glue. The \hat{z} measurement axis of the **Titan** was aligned to be parallel to the measurement axis of the OMIS and the normal vector of the mirror surface. To inject vibrations into the system, beneath the mounting feet of the **Titan**, three controllable piezoelectric ceramics (PZT) were installed. The **Titan** was then bolted to an aluminum base-plate that sandwiched the PZT between the legs of the **Titan** and the base-plate. Three equally spaced support legs were attached beneath the baseplate, and the whole setup was placed on a Minus-K BM-1 bench top vibration isolation platform, and housed within an acoustic isolation box. We then aligned the retro-reflection mirror to ensure overlap of the incoming and reflected RAMAN light. Alignment was achieved by changing the weight distribution of counterweights on the vibration isolation platform. The acoustic isolation box was sealed during measurements.

5B.4 Sensor Specifications

Table 5B.1: Physical Specifications of each sensor, from which we can calculate the change in reflected light as a function of test mass acceleration.

Sensor	Mechanical Resonance ω_0	Mechanical Q Factor	Cavity Length	Mid-fringe Point
OMIS 1	7636 Hz	805.8	126 μm	1559.8 nm
OMIS 2	7789 Hz	1116	111 μm	1558.0 nm
OMIS 3	7475 Hz	1318	52 μm	1560.0 nm

To determine mechanical acceleration of the sensor from a reflected optical signal, we need to determine the physical properties that govern the behavior of our sensors. In the course of the research performed in this thesis, we worked with three separate OMIS sensors with varying cavity lengths and mid-fringe points, labeled: OMIS 1, OMIS 2, and OMIS 3. The midfringe point of OMIS 2 had an ideal midfringe point wavelength for our source laser, unless otherwise stated, all measurements were taken with OMIS 2. The sensors used in this thesis were optimized for a different task, and for this reason, these devices have a large mechanical resonance on the order of 7 kHz and low optical finesse ($\mathcal{F} \approx 2$). The consequences of these mechanical properties will be discussed further in section 5B.6. This section will focus on how the measurement of the physical properties of each sensor was performed.

Measuring the Mechanical Resonance and Quality Factor of the Optical Resonator

The mechanical resonance was determined by measuring the reflected optical signal and operating the PZTs with a single driving frequency and low amplitude. We could then determine the driving frequency that maximized the time series amplitude.

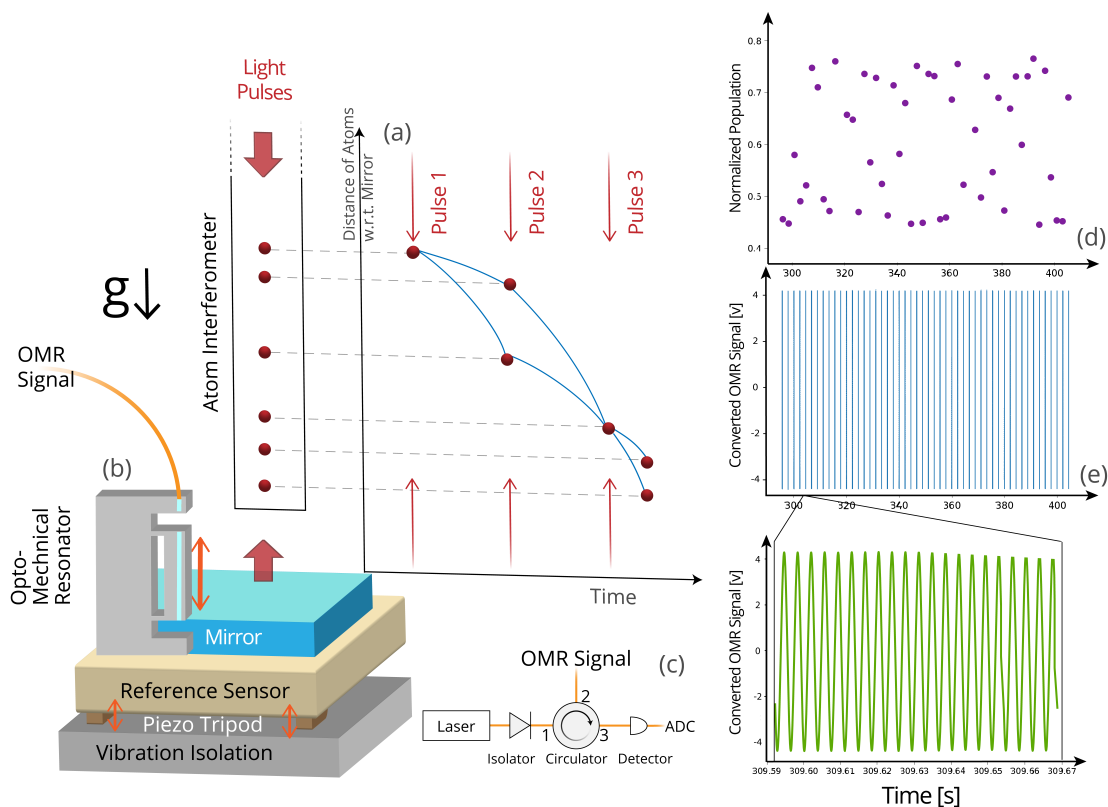


Figure 5B.4: The OMIS setup can be broken into two parts; the optical setup and the mechanical setup. This figure is not to scale. Within the opto-mechanical resonator enhanced atom interferometer, a source laser passes through a fiber isolator and fiber circulator. Light at port 2 is sent to the OMIS and reflected light re-enters port 2 to be sent to port 3. The optical signal is read off using a photo-detector and the voltage across a load resistor of the photo-detector is measured using an ADC. Within the mechanical setup, the OMIS is attached to the side of a 2 inch retro-reflection mirror with glue [Torr seal] and the retro-reflection mirror is then ceramic glued to the top of a Nanometrics Titan. Three piezoelectric stacks are attached to the base of the Nanometrics Titan to be able to inject vibrations. The whole system sits beneath our Raman beam, and is aligned to reflect the Raman beam back through the vacuum chamber. The entire setup lays on top of a vibration isolation platform in an acoustic isolation box.

The mechanical quality factor (Q), can be measured by mechanically exciting the oscillator and then measuring the ring-down:

$$V_{\text{meas}}(t) = V_0 e^{-\omega_0 t / 2Q} \quad (5B.7)$$

To measure the ring-down, we excited the OMIS with external piezoelectric transducer (PZT) (Fig. 5B.4) driving near the OMIS mechanical resonance ω_0 , then the driving voltage to the PZT were abruptly turned off. After the driving oscillation stopped, the signal of the oscillation were measured on a photodetector and an envelope was fit to the oscillations to determine the exponential decay giving Q .

For each sensor, this was measured in *Bremen* at the *DLR* within vacuum. Due to the fact our sensors are operate in atmosphere, when we remeasured these parameters for each sensor, they were much lower ($Q_{\text{Air}} = 193.4$) than what was measured in vacuum ($Q_{\text{Vacuum}} = 1116$). However, a decreased mechanical quality factor primarily affects the sensor's behavior near resonance, which is well outside the frequency region of interest for atom interferometry.

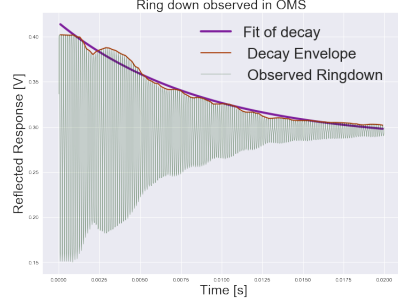


Figure 5B.5: After mechanically exciting the OMIS we turned off the excitation and observed the ringdown of the sensor under atmospheric pressure.

Measuring the Cavity Response

The voltage response of the OMIS is highly dependant on multiple system-specific parameters, such as the efficiency of the photo detector, gain of the amplifier, how much light is reflected from the OMIS, re-coupling of cavity light into the fiber and the output power of the source laser. Due to these multiple dependencies, it is best to measure $dV/d\lambda$ for each specific sensor and setup.

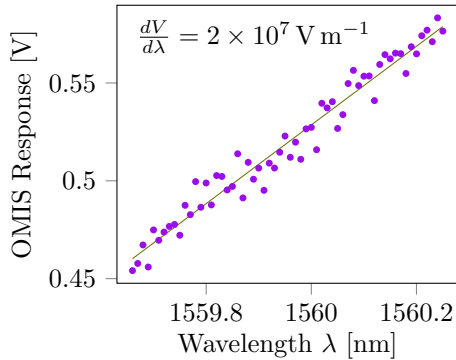


Figure 5B.6: The optical response of OMIS 3 to changes in wavelength. The slope $dV/d\lambda$ can be measured by scanning the wavelength and measuring the reflected response of the sensor using a photo-detector. However, parasitic cavities are also present in the OMIS, leading to a response from multiple cavities when scanning the wavelength.

5B.6).

To measure the voltage response, we scan the source laser wavelength, λ , and measure the output of the circulator on our photo detector. By recording the voltages as a function of wavelength, we can then fit a slope to measure $dV/d\lambda$.

However, when measuring this in practice with our prototype OMIS, it became clear that more cavities, other than the primary cavity, were present. We will collectively refer to all cavities formed, that are not the primary cavity between the lead fiber and fiber fragment, as "parasitic cavities". The effect of these parasitic cavities will be discussed further in section 5B.6.3. For our measurement of the cavity response, as we scan the wavelength, we will also scan the response of these parasitic cavities, meaning our total voltage response is a sum of the primary cavity response plus the parasitic cavities (equation 5B.13).

To measure the slope of $dV/d\lambda$, we average of the measured voltage. We, for example, were able to measure a slope of $dV/d\lambda = 1.68 \times 10^7 \text{ V m}^{-1}$ for OMIS 2 and $dV/d\lambda = 2 \times 10^7 \text{ V m}^{-1}$ for OMIS 3 (Fig

5B.4.1 OMIS Generator Constant

Similar to the generator constant of the classical sensors, we can simplify the multiple parameters that determine the OMIS response to a simple generator constant of the OMIS:

$$G = \frac{|X(\omega)|}{|A(\omega)|} \frac{\lambda_0}{L} \left(\frac{dV}{d\lambda} \right). \quad (5B.8)$$

With the three sensors used, the mechanical transfer function $\frac{|X(\omega)|}{|A(\omega)|}$ is approximately constant for $f < 1000$ Hz. Therefore, for frequencies of interest to our atom interferometer ², post-correction can be performed with a generator constant that is constant with respect to frequency; $a = V_r/G$

5B.5 Results from Hybridization with the Optical Resonator

In this section we will explore the performance of the optical resonator.

5B.5.1 Optical Resonator post-correction in High motion Environments

To evaluate the post-correction performance of the OMIS, we introduced vibrations of a specific frequency and used the OMIS and Titan to post-correct the atom interferometer at a mid-fringe position (section 3.3.1). These measurements provide useful tools for characterizing the OMIS frequency response as well as the performance compared to other classical devices. These measurements were performed for MACH-ZEHNDER type interferometers of various pulse separation times, and induced ground motion. The purpose of these measurements was purely diagnostic and therefore the mid-fringe sweep rate value was chosen near the standard null fringe value, but otherwise arbitrary. Furthermore, we performed these measurements for only one direction of momentum transfer.

The induced ground motion is generated from three piezoelectric transducer (PZT) driven by an external function generator. We can then excite vibrations of the retro-reflector, which can be measured with the Titan and resonator, allowing us to determine the frequency response of our ground motion devices. Due to low frequency ground motion mechanically coupling into the OMIS lead fiber (section 5B.6.3), we cannot perform strap-down measurements which are sensitive to environmental ground motion. Additionally low frequency mechanical coupling to the fiber and intensity noise from the source laser limit the maximum pulse separation time T we can use for a measurement. As T is increased the atom interferometer is less sensitive to higher frequency vibrations. For this reason, measurements were restricted to roughly 10 ms, where we could create enough motion on the inertial reference, while minimally coupling to the fiber. By recording the induced motion with the OMIS and Titan, we can correlate it in time to the atom interferometer and post-correct the phase $\Delta\phi_{PC}$. With the phase correction applied to each data point we can reconstruct the fringe pattern, and fit a sine to our data.

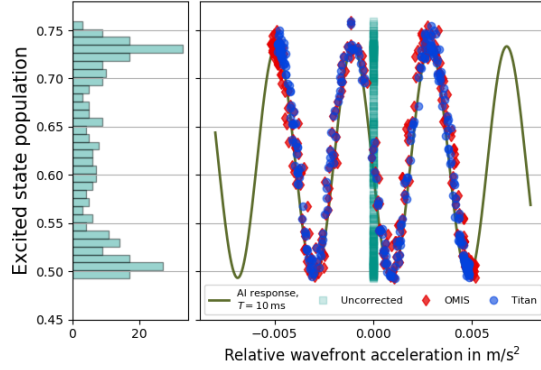


Figure 5B.7: The post-corrected data with a histogram of the distribution. Since the mirror was driven with piezos, the histogram will not follow a bi-modal distribution, however from the histogram the contrast and offset can still be obtained, from which we can fit the post-corrected data.

Results of Hybridization in High Motion Environments

For characterization of the short term performance of the OMIS, we took a 300 cycle atom interferometric measurement with a $T = 10$ ms pulse separation time and cycle time of 1.6 s. During this measurement, the PZTs were driven sinusoidally with a frequency of 350 Hz and a peak-to-peak amplitude of 20 V. During each atom interferometer cycle, data from the OMIS and *Titan* were simultaneously acquired and then recorded and after the measurement was complete, we applied the post-correction algorithm (ref. 3.3.1). The recorded signal from the optical resonator was digitally filtered with a band-pass filter from [300 Hz-400 Hz] to attenuate non-physical electronic noise (section 5.1.4) from outside of the measurement bandwidth of each sensor³.

By binning the normalized $P_{|F=2\rangle}$ population data from each measurement of the atom interferometer, we can form a histogram of the population to determine the AI contrast offset and technical noise. The period of the fringe is determined by the pulse separation time. With these parameters, we bin the 300 point measurement into subsets of 10 points each and fit a sine function with only the phase as a free parameter. From the phase of the fit of the post-corrected data points we calculate the ADEV of the post-corrected data points. By using the suppression factor method outlined in section 5.2 we can quantify the performance of our post-correction. In this case we were able to reduce from the weighted acceleration for the OMIS of $\sigma_{\text{weighted}}^{\text{OMIS}} = 4.69 \times 10^{-3} \text{ m/s}^2/\sqrt{\text{Hz}}$ to $\sigma_{\text{PC}}^{\text{OMIS}} = 1.0 \times 10^{-4} \text{ m/s}^2/\sqrt{\text{Hz}}$ giving us a suppression factor of $\gamma_{\text{OMIS}} = 46.8$. For the *Titan* we were able to post-correct from the weighted uncorrected acceleration $\sigma_{\text{weighted}}^{\text{Titan}} = 4.57 \times 10^{-3} \text{ m/s}^2/\sqrt{\text{Hz}}$ to $\sigma_{\text{PC}}^{\text{Titan}} = 6.52 \times 10^{-5} \text{ m/s}^2/\sqrt{\text{Hz}}$ yielding a suppression factor of $\gamma_{\text{Titan}} = 70.1$. The disparity in suppression factor between the OMIS and *Titan* will be addressed in section 5B.6.

²For a $T = 10$ ms atom interferometer, the corner frequency is 50 Hz. Frequencies above 1×10^3 Hz will be strongly attenuated by the low pass behavior of the atom interferometer.

³For the OMIS this represents the need to suppress intensity noise of the source laser (subsection 5B.6.2).

5B.5.2 Long Term Stability of Hybridization with the Optical Resonator

To determine the performance of the OMIS in a realistic gravimetry setting we performed a 19.5 h 11980 cycle measurement; of which 10900 points were used to measure the local gravitational acceleration with ^{87}Rb . The piezoelectric transducer (PZT) used for exciting vibrations on the retro-reflection mirror (Fig. 5B.4) were driven with 20 V at 350 Hz generating an AI weighted acceleration short term uncertainty of: $\sigma_{\text{weighted}} = 8.00 \times 10^{-3} \text{ m/s}^2/\sqrt{\text{Hz}}$.

We performed interferometry with pulse lengths $T = 9 \text{ ms}$, $T = 10 \text{ ms}$ and $T = 11 \text{ ms}$ for central fringe determination for both directions of momentum transfer. We then determined the mid-fringe position for both directions of momentum transfer ($\alpha_{k_-} = -25.1503 \text{ MHz s}^{-1}$, $\alpha_{k_+} = 25.1501 \text{ MHz s}^{-1}$). When the piezos are turned on, inertial reference motion will shift the output of the interferometer symmetrically several fringes around the mid-fringe position. This spread ensures that with a sample of AI measurements we can fit a sine and measure the local gravitational acceleration. We performed 11 cycles for one direction of momentum transfer and then switched to 11 cycles in the other direction, after which we switched back to the first direction. This processes was repeated for the entire measurement. As was performed in the short term post-correction, during each shot we recorded data from the OMIS and *Titan* simultaneously and in conjunction with the atom interferometer. Each shot contains 20 ms of pre-trigger samples and was measured with a sampling rate of 100 kHz.

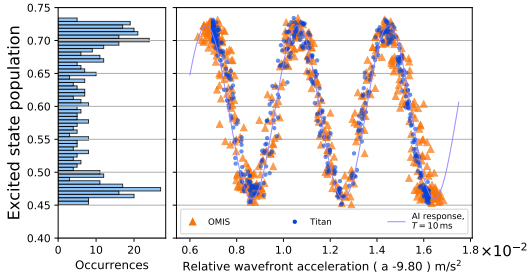


Figure 5B.8: Here 1000 points are shown of k_+ direction of momentum transfer are shown. The offset and amplitude can be extracted from the point spread function (left) of the data set, which we can then use to get a fit of the post-corrected data points (right)

and offset, we cut the data into 545 point segments and performed a histogram of the population. We then separated the data into groups of 50 measurements for fringe fitting. The amplitude and offset are measured from the histogram fit and the frequency comes from the pulse separation time T , leaving only the phase of the fit as a free parameter. From this we can extract \vec{g} for one direction of momentum transfer. We took the half difference between the k_+ and k_- phase fits following the momentum reversal method (section 3.3.2) to get the final result of our measurement of the gravitational acceleration .

After the long term measurement was complete, we sequenced the ground motion data to corresponding k_+ and k_- measurements and then applied a digital band-pass filter of 300-450 Hz. We selected our pre-trigger samples (ref. 4.3) that minimized the residuals of the fit for each sensor. We then applied the generator constant for the *Titan* and the measured generator constant of the OMIS to convert our voltages to accelerations. After this we integrated the time series measured voltage with the sensitivity function (section 2.2.1) to get the total phase shift that occurred during a given shot, and applied that phase correction to the measured mid-fringe point.

We performed this on all of the data points of the measurement for both directions of momentum transfer. To get the value of the amplitude

Post-correction

The measurement had an average per shot cycle time of $\tau_{\text{average}} = 5.44$ s. One measurement of the gravitational acceleration required 100 points total (50 k_+ and 50 k_-), and therefore a total cycle time of $\tau = 272$ s⁴. From the fits of the post-corrected data, we extracted the measured value of the phase, which we then used to calculate the acceleration.

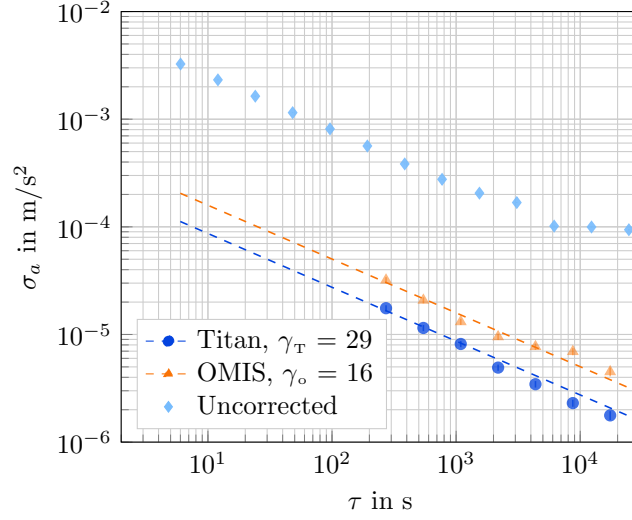


Figure 5B.9: The improvement factor is calculated from the ratio of the short-term uncertainty of the uncorrected data $\sigma_u = 8 \times 10^{-3} \text{ m/s}^2/\sqrt{\text{Hz}}$ to the short term uncertainty of the post-corrected data for the OMIS (**Titan**) $\sigma_O = 5 \times 10^{-4} \text{ m/s}^2/\sqrt{\text{Hz}}$ ($\sigma_T = 2.7 \times 10^{-4} \text{ m/s}^2/\sqrt{\text{Hz}}$).

We fit a $1/\sqrt{\tau}$ curve to the acceleration measurements of the **Titan** and OMIS to extrapolate the short-term uncertainty at $\tau = 5.44$ s (one shot) and also the value of the uncertainty at one second. The suppression factor of the OMIS was $\gamma_o = 16$ and for the **Titan** was $\gamma_T = 29$. The uncorrected short-term uncertainty of $\sigma_u = 8 \times 10^{-3} \text{ m/s}^2/\sqrt{\text{Hz}}$. The short-term uncertainty is calculated after post correction to be $\sigma_O = 5 \times 10^{-4} \text{ m/s}^2/\sqrt{\text{Hz}}$ for the OMIS and $\sigma_T = 2.7 \times 10^{-4} \text{ m/s}^2/\sqrt{\text{Hz}}$ for the **Titan**. We were able to integrate down to $\sigma_O = 4.50 \times 10^{-6} \text{ m s}^{-2}$ with the OMIS and $\sigma_T = 1.77 \times 10^{-6} \text{ m s}^{-2}$ with the **Titan** after 24656.5 s of integration.

⁴Each shot took $\tau = 2.72$ s to complete, but since the k_+ and k_- cycles were interleaved the total cycle time of one direction of momentum transfer was $\tau = 5.44$ s

5B.5.3 Comparison of Titan and OMIS

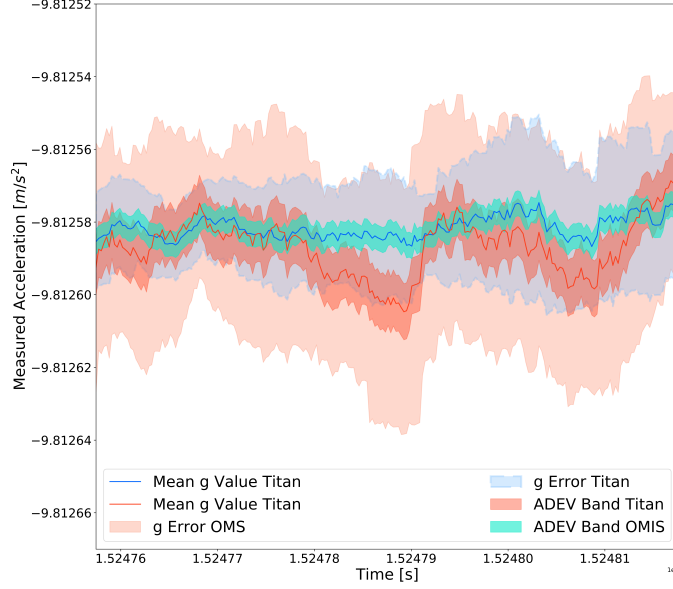


Figure 5B.10: The measured g value after post correction with the **Titan** and **OMIS**. We calculated the rolling average for the **OMIS** (red solid line) and the **Titan** (green solid line). The ADEV uncertainty band for the uncertainty at 6164.1 s is shown for both the **Titan** and **OMIS**. Deviations

To understand the long term behavior of the post-correction of the result, we performed a rolling average (Fig. 5B.10) defined by on the post-corrected data to calculate the average measured gravitational acceleration \bar{g} over time.

$$g_i = \sum_{i=1}^N \frac{g_{i-1} + g_{i+1}}{N} \quad (5B.9)$$

From here we can compare the rolling average signal of the **OMIS** to the Allan Deviation (ADEV) of the **Titan**. We measure a maximum difference between the **Titan** of $\bar{g}_{\text{Titan}} - \bar{g}_{\text{OMIS}} = 1.929 \times 10^{-5} \text{ ms}^{-2}$, corresponding to a difference in 3.6 times the uncertainty of the **Titan** σ_T , or 1.7 times the uncertainty of the **OMIS** at 6164.1 s.⁵ This difference is well within the combined uncertainty of the two sensors, and with this small difference, we can claim that the **OMIS** does not add any bias to the post-correction on the timescale of the measurement.

⁵Defined as the uncertainty at $T = \frac{1}{3}$ measurement total. This corresponds to the stability of the **Titan** and **OMIS** at 6164.1 s

5B.6 OMIS Post Correction Limitations

The OMIS will suffer from some of the same primary noise source contributions as the commercially available motion sensors, however post-correction with the OMIS yields unique limitations to the performance of the post correction. Some contributions such as intensity and frequency noise, are dependent on the source laser, whereas some contributions such as the parasitic cavities and thermal limitations are generated from the OMIS. In this section we will focus on these key differences ⁶.

Table 5B.2: Leading noise contributions for post-correction with OMIS 2 in a $T = 10$ ms atom interferometer

Noise Source	Contribution
Frequency Noise	$\tilde{a}_{\text{Freq}} = 2.1 \times 10^{-5} \text{ m/s}^2/\sqrt{\text{Hz}}$
Intensity Noise ⁷	$\tilde{a}_{\text{Int}} = 2.2 \times 10^{-4} \text{ m/s}^2/\sqrt{\text{Hz}}$
Fiber Noise	$\tilde{a}_{\text{FN}} > 2.7 \times 10^{-3} \text{ m/s}^2/\sqrt{\text{Hz}}$
Transmission Loss	$\tilde{a}_{\text{TL}} = 2.1 \times 10^{-10} \text{ m/s}^2/\sqrt{\text{Hz}}$
Thermal Limit	$\tilde{a}_{\text{Therm}} = 5.8 \times 10^{-11} \text{ m/s}^2/\sqrt{\text{Hz}}$

5B.6.1 Frequency Noise

Frequency noise of the laser enters as displacement noise and is independent of the voltage response $dV/d\lambda$ of the OMIS. From this displacement noise we can use the mechanical transfer function of a harmonic oscillator (equation 5B.2) to calculate the acceleration noise due to a change in frequency as:

$$\delta a_{\text{Freq}}(\omega) = \frac{|A(\omega)|}{|X(\omega)|} \frac{\lambda_0 L}{c} \delta f \quad (5B.10)$$

To obtain the frequency noise of our laser, we beat the free-running laser [NKT ADJUSTIK C-15] against an in-house frequency comb. With this change in measured acceleration as a function of frequency, and we calculated the acceleration power spectral density, from which we could use equation 5B.11 to calculate the RMS acceleration for interferometers of various pulse separation times T .

$$(\tilde{a}_{\text{Freq}})^2 = k_{\text{eff}}^2 \int_0^\infty |H_a(\omega, T)|^2 S_a(\omega) d\omega. \quad (5B.11)$$

For a $T = 10$ ms atom interferometer, we calculated a frequency induced acceleration signal of $\tilde{a}_{\text{Freq}} = 2.11 \times 10^{-5} \text{ m/s}^2$. Our OMIS post-correction measurement is not currently frequency

⁶Noise contributions are given in terms of RMS acceleration \tilde{a} instead of RMS phase as is done in the previous chapter. Since we are not limited by the atom interferometer, it is more useful to look at the limitations of the OMIS compared to other motion sensors which is more convenient to study in terms of acceleration, as opposed to in terms of phase which is useful for understanding limitations of the atom interferometer. One can convert from RMS phase to RMS acceleration using the scale factor $\phi = k_{\text{eff}} T^2 a$.

⁷This is the filtered contribution for filters corresponding to the measurement parameters. Explained further in subsection 5B.6.2.

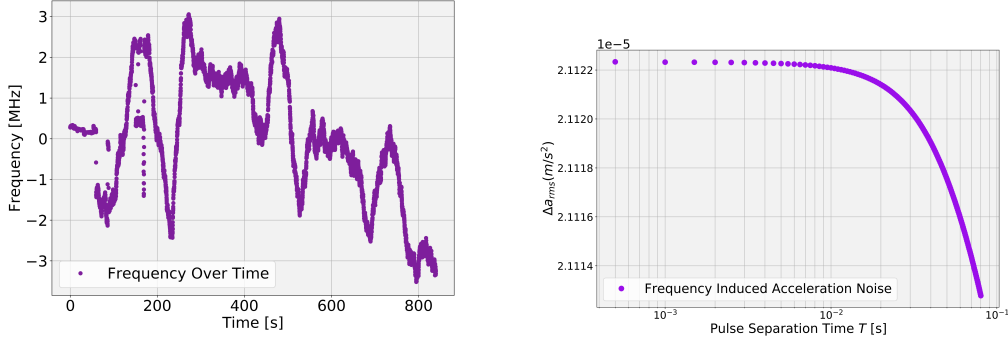


Figure 5B.11: *Left.* The frequency drift of the free running NKT over time. The frequency drift was measured by analyzing a beat of the NKT laser against a frequency comb housed within the institute. The drift around the central beat (34 MHz) is shown. *Right.* From the frequency induced acceleration noise we could calculate the PSD of the noise and use the sensitivity function (equation 5B.11) for interferometers of various pulse separation times T . For $T = 10$ ms the frequency noise created an acceleration noise signal of $\tilde{a}_{\text{Freq}} = 2.11 \times 10^{-5} \text{ m s}^{-2}$

noise limited by the free-running NKT laser. Frequency noise affecting an OMIS with higher sensitivity could mitigate frequency noise by locking the frequency of the laser. One benefit of the 1560 nm wavelength⁸ optics within the sensor is that in the future we could frequency double the light and lock it to the ^{87}Rb D_2 line.

5B.6.2 Intensity Noise

Intensity noise from the source laser presents a major contribution to the total limitations of the sensitivity of the OMIS, and comprises a large reason why filtering of the OMIS signal is required. Intensity noise enters linearly into our OMIS response equation, and therefore a change in intensity will linearly mimic motion of the OMIS. This section will focus on intensity noise from the source laser, fiber induced transmission loss within the fibers will be addressed in the next section.

The voltage response of the photo detector can be modeled as $V = K_{\text{PD}}I$, where K_{PD} is the photo detector gain. With the OMIS generator constant (equation 5B.8) we can model the relative intensity noise as:

$$\delta a_{\text{Intensity}} = \frac{|A(\omega)|}{|X(\omega)|} \frac{L}{\lambda_0} \left(\frac{dV}{d\lambda} \right)^{-1} V_{\text{Mid}} \delta I_{\text{RIN}} \quad (5B.12)$$

Where V_{Mid} is the measured photo-detector voltage at the midfringe, and δI_{RIN} is the relative intensity noise.

⁸In principle the only reason the sensor was designed to operate with 1560 nm light was due to the availability of fiber components at telecom wavelengths. In the future an OMIS could be designed to use a portion of locked cooling light of the ^{87}Rb system.

We directly measured the intensity fluctuations of the source laser with the photo-detector used within the post-correction measurements. From these fluctuations we can use equation 5B.12 to calculate the power spectral density of the intensity induced acceleration noise. This was done for the raw-unfiltered signal giving us the RMS noise over all frequencies, and also calculated for the acceleration contribution to measurements taken within this thesis (Filtered frequencies = 300-450 Hz). For the total RMS acceleration contribution we get a contribution of $\tilde{a}_{\text{Int}}^{\text{Filtered}} = 0.31 \text{ m/s}^2/\sqrt{\text{Hz}}$ for our $T = 10 \text{ ms}$. For the 350-450 Hz filtered signal used for post-correction in this thesis we get a contribution of $\tilde{a}_{\text{Int}}^{\text{Filtered}} = 2.23 \times 10^{-4} \text{ m/s}^2/\sqrt{\text{Hz}}$ for our $T = 10 \text{ ms}$ interferometer.

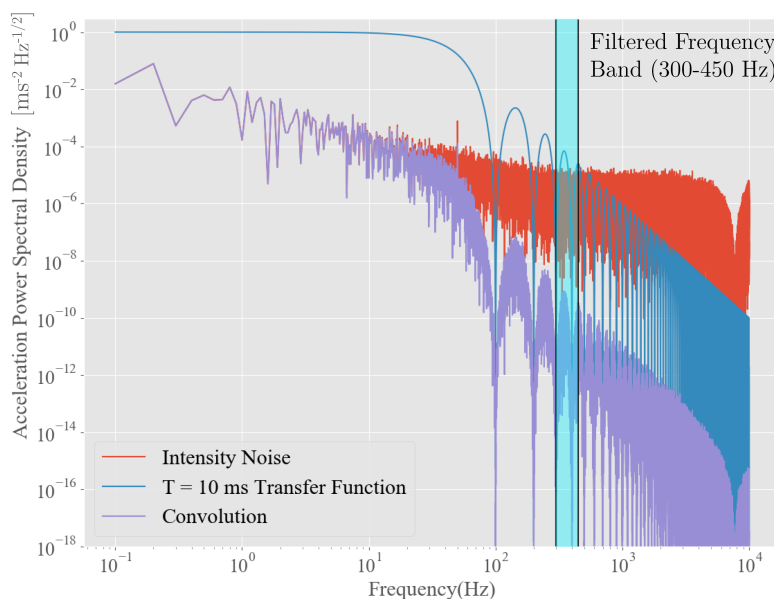


Figure 5B.12: The power spectral density of the intensity noise contribution of the source laser, the transfer function for a $T = 10 \text{ ms}$ atom interferometer and the convolution of the two. Noise contributions are calculated over the entire frequency range, as well as the range in which the measurements are taken 300-450 Hz.

Intensity noise from the source laser presents a major limitation to the sensor. This noise is generated from the relative intensity noise of the laser, and can be addressed in future systems through the use of an intensity stabilization system. For example, a fiber-splitter could divert a portion of light for monitoring, and where this signal could be used to drive a fiber AOM placed before the circulator.

5B.6.3 Parasitic Cavities and Fiber Noise

The splicing and attachment of the lead fiber and test mass fiber, is unique to the construction of each OMIS. This means that each OMIS sensor will have a unique set of optical properties, including

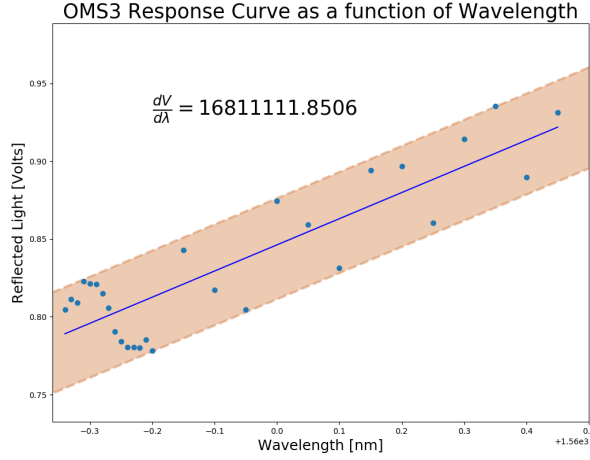


Figure 5B.13: Demonstration of parasitic cavities on OMIS 2, When measuring $dV/d\lambda$ we can see the sinusoidal response of a parasitic cavity on top of the response from the resonator cavity. These parasitic cavities add additional intensity fluctuations that limit the performance of the OMIS.

the optical contribution of parasitic cavities. In the course of measurements taken with OMIS 1 and OMIS 2, the optical contribution of parasitic cavities in conjunction with fiber noise, played a large role in the limitation for measurements of acceleration, primarily in the low frequency regime.

Fiber noise is a generic term referring to the intensity, phase and polarization noise caused by mechanical perturbations of the optical fiber [97, 98].

The calculation of the the cavity response in equation 5B.6 made the assumption that the OMIS has been ideal and that the resonator cavity is the only optical cavity present. To understand how the collective effects of fiber noise plays a role in our measurement from the OMIS we need to include the optical response from additional parasitic cavities in the approximation of low optical finesse:

$$V_r(\lambda) = \underbrace{A_1 \sin\left(\frac{c}{2L_1}\lambda + \phi\right)}_{\text{OMIS Cavity}} + \underbrace{A_2 \sin\left(\frac{c}{2L_2}\lambda + \phi\right) + A_3 \sin\left(\frac{c}{2L_3}\lambda + \phi\right) + \dots}_{\text{Parasitic Cavities}} \quad (5B.13)$$

Where A_n is the cavity amplitude response, L_n is the cavity length and ϕ_n is the offset of a cavity n . We assume the phase offset ϕ_n is constant. Since the optical response of the resonator cavity is much larger ($A_1 \ll A_{n+1}$), the parasitic cavities will not depend on the response of the resonator cavity, and therefore we can approximate the total response as summation of optical responses instead of a product of responses. In the OMIS mid-fringe regime the primary cavity we can apply the small angle approximation which then becomes:

$$V_r(\lambda) = \frac{A_1 c}{2L_1} \lambda + \phi + A_2 \sin\left(\frac{c}{2L_2} \lambda + \phi\right) + A_3 \sin\left(\frac{c}{2L_3} \lambda + \phi\right) + \dots \quad (5B.14)$$

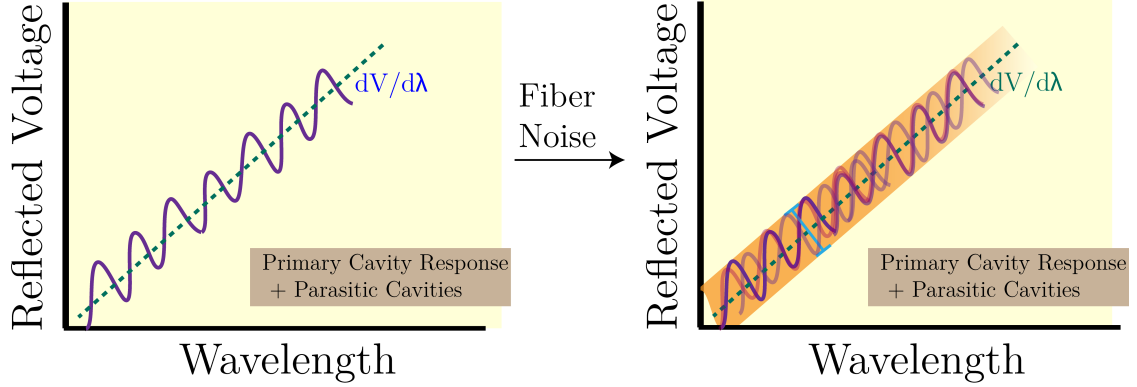


Figure 5B.14: We can model phase noise of the parasitic cavities as intensity noise and therefore put an upper bound on the contribution due to path length changes occurring within the fiber.

We can also calculate the voltage response $dV/d\lambda$:

$$\frac{dV_r}{d\lambda} = \frac{A_1 c}{2L_1} + \frac{A_2 c}{2L_2} \cos\left(\frac{c}{2L_2}\lambda + \phi\right) + \frac{A_3 c}{2L_3} \cos\left(\frac{c}{2L_3}\lambda + \phi\right) + \dots \quad (5B.15)$$

The location of the parasitic cavities within the OMIS system will lead to different behavior. For example, parasitic cavities are formed within the lead fiber will be sensitive to perturbations of the lead fiber, but parasitic cavities contained within the test mass will not. Furthermore, some parasitic cavities will depend on the resonator cavity length and therefore will be sensitive to test mass displacement. For this reason it is important to draw two types of cavity: parasitic cavities that are **inertially sensitive** and parasitic cavities that are **non-inertially sensitive**.

Non-Inertially Sensitive Parasitic Cavities

The YOUNG'S modulus for a coated fiber is $E_g = 16.56 \text{ GPa}$ [99]. Meaning that for the 40 cm lead fiber a force of only 12 mN is enough to change the optical path length by $\lambda/4$ for our 1560 nm light.

Parasitic cavities formed within the optical fiber will be effect by changes in path length of the fiber and can be modeled as:

$$V_r(\lambda) = \frac{A_1 c}{2L_1} \lambda + \phi + A_2 \sin\left(\frac{c}{2(L_2 + \delta L)}\lambda + \phi\right) + A_3 \sin\left(\frac{c}{2(L_3 + \delta L)}\lambda + \phi\right) + \dots \quad (5B.16)$$

For a given fixed source wavelength λ_0 entering the lead fiber mechanical stress due to vibrations will induce length changes δL of the parasitic cavities. These parasitic cavities will change the offset in response measured at port 3, which will mimic an acceleration.

Due to the difficulty of measuring the parasitic cavities within the lead fiber, we cannot determine how much of a length change δL is occurring within the fiber. We can however put an upper bound on the contribution from parasitic cavities by treating a change in offset due to δL as a change in intensity. We can then model this as intensity noise with amplitude δA_N for a cavity N . We can then

use equation 5B.12 to calculate the acceleration noise contribution from such a cavity. For example for OMIS 2, we measured a parasitic cavity amplitude (figure 5B.13) $A_1 = 0.04$ V. From this we get $\tilde{a}_{\text{FN}} > 2.67 \times 10^{-3} \text{ m/s}^2/\sqrt{\text{Hz}}$, which is larger than the short-term uncertainty measured in both the short term measurement and the long term gravitational acceleration measurement. Unfortunately, the construction of the OMIS provides no way to distinguish the parasitic cavity intensities form in this experimental setup there is no way to reduce the constraint of this bound, however methods for addressing the fiber noise will be offered later in this section.

Inertially Sensitive Parasitic Cavities

Parasitic cavities can also be formed that include the length of the primary cavity in the total overall length, meaning for example $L_n = L_1 + L'$. Meaning that a change in the test mass position would also change the overall response.

$$V_r(\lambda) = \frac{A_1 c}{2L_1} \lambda + \phi + A_2 \sin\left(\frac{c}{2(L_1 + L')} \lambda + \phi\right) + A_3 \sin\left(\frac{c}{2(L_1 + L')} \lambda + \phi\right) + \dots \quad (5B.17)$$

This type of parasitic cavity changes $dV/d\lambda$ and therefore makes it difficult to measure the acceleration from the optical cavity response. However due to the multiple medium changes required (*e.g.* $n_{\text{Fused Silica}} \rightarrow n_{\text{Air}}$), the total reflected light from these cavities is minimal. The sensor OMIS 1 was prone to these type of cavities and therefore made it difficult to measure. This was likely due to defects in the construction of the sensor, and OMIS 2 did not have a measurable contribution from inertially sensitive parasitic cavities.

Solutions

We can address the fiber noise in the system by: reducing the number of parasitic cavities; increasing the optical finesse of the OMIS cavity; and minimizing mechanical coupling to the fiber.

Small changes in the design of the OMIS can reduce the ability for parasitic cavities to form. Future designs of the OMIS will incorporate a strong angle cleave on fiber tip at the end of the fiber contained within the test mass. This will minimize reflections within OMIS test mass fiber. We can further eliminate any cavity formed between the APC connector and the lead fiber of the OMIS by fiber splicing port 2 directly to the lead fiber. Further design of the OMIS to suppress parasitic cavities is also being considered. Lastly a non-perpendicular cleave of the lead fiber tip will increase the likelihood of cavities formed from total internal reflection within the fiber. By ensuring a perpendicular cleave we can minimize the effect from these cavities.

The second technique is to mitigate parasitic effects is to simply increase the amount of light reflected from the resonator OMIS cavity. Since all reflecting surfaces assume to be forming parasitic cavities within the OMIS are uncoated, they all have the same reflectivity $\approx 4\%$; the same as the cavity. By coating the fiber tips of the cavity with a reflective material, we can increase the finesse of the resonator cavity reducing the overall percentage of reflected light coming from parasitic cavities. This will of course increase the finesse of the OMIS cavity, and place more stringent requirements on the frequency noise of the source laser.

We can also reduce the mechanical coupling of fibers leading to the OMIS to minimize fiber induced noise, as well as mechanically induced transmission loss (section 5B.6.4) . This was the

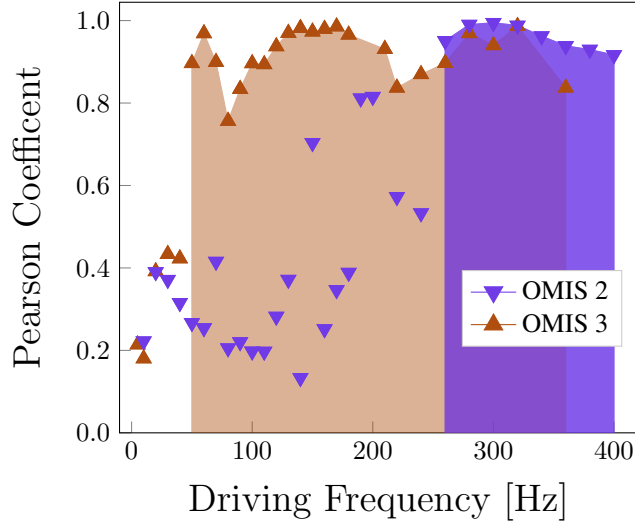


Figure 5B.15: The PEARSON coefficient of a time series signal taken from both an OMIS and Titan at a given frequency. This was performed for both OMIS 2 and OMIS 3. The shaded area represents the frequencies where mechanical oscillations were not coupling into the lead fiber, disturbing the OMIS response. For OMIS 2 the driving frequency where we can measure is $f_d > 260$ Hz and for OMIS 3 $f_d > 50$ Hz. The difference between the two is partially due to higher reflectivity of OMIS 3, lessening the effects of other parasitic cavities formed within the OMIS

method employed in our measurements with the OMIS; and was the primary reason for placing the OMIS-Titan stack on a vibration isolation platform and driving mirror motion with piezo frequencies around 350 Hz. We found that at this driving frequency the vibrations do not mechanically couple in as strongly into the fiber and therefore reduced the effect of parasitic cavity noise.

To measure this effect, we mechanically excited the sensor stack by driving the piezos at a given frequency. We then recorded a 10 s measurement of the OMIS and Titan with a sampling rate of 2×10^5 samples/s. We then correlated the signals and calculated the PEARSON coefficient of the two signals as a function of frequency, see figure 5B.15. This was performed for OMIS 2 and OMIS 3.

5B.6.4 Mechanically Induced Transmission Loss

Mechanical stress of the optical fiber can lead to scattering within the fiber and a mechanical loss of optical signal. This is known as mechanically induced transmission loss [99]. These mechanical induced losses change the intensity transmitted through the fiber to the OMIS, and light reflected from the OMIS. As the attenuation changes, so will the amount of light exiting port 3, mimicking a change in displacement. To characterize the effect of mechanical stress on our system, we sent light into port 2 and placed our photo detector at port 3. We then introduced mechanical oscillations along the path of the light and recorded the intensity fluctuations at the photo detector as a function of frequency.

We were able to measure a change in intensity on the order of $\tilde{a}_{\text{FN Int}} = 2.11 \times 10^{-10} \text{ m/s}^2/\sqrt{\text{Hz}}$ for 350 Hz. Reducing mechanical coupling to the fiber as mentioned in the previous section will

reduce mechanical induced transmission loss.

5B.6.5 Thermal Limitation

The thermal limitation represents the BROWNIAN motion of the sensor and is given by:

$$\tilde{a}_{\text{Therm}} = \sqrt{\frac{4k_B T}{mQ}} \quad (5B.18)$$

Where k_B is the BOLTZMANN Constant, the temperature is 300 K, $m = 25$ mg, and the measured $Q = 193.4$ in air OMIS 2 yielding an acceleration white noise limit $\tilde{a}_{\text{Therm}} = 5.8 \times 10^{-11} \text{ m/s}^2/\sqrt{\text{Hz}}$. Future sensors can minimize the contribution to the thermal limit by operating the sensor at lower temperatures and increasing the mass or the quality factor.

5B.6.6 Combined Noise Sources

We can combine the individual noise sources listed above to determine the current measurement limitation of the sensor with the current optical setup. To perform this measurement the OMIS was placed within the acoustic isolation, with the vibration isolation platform on. The OMIS voltage response $dV/d\lambda$ was measured and the reflected OMIS voltage was measured on a photo-diode for 10 s with a sampling rate of 2×10^4 point per second. Simultaneously signal from the *Titan* was measured to account for any motion during the measurement. The measured *Titan* signal was subtracted from the OMIS and the resulting self noise was plotted. This measurement was compared to the power spectral density of the other noise source contributions.

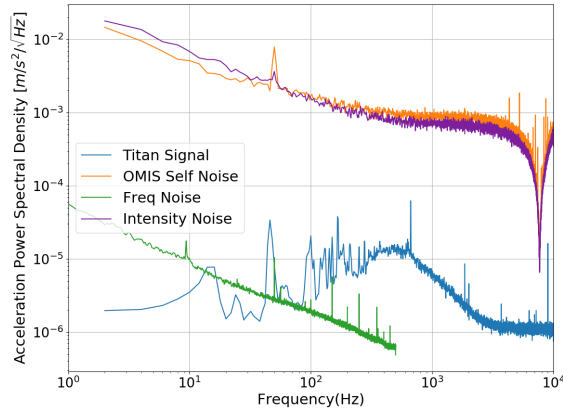


Figure 5B.16: Measurement of the individual noise components, compared to the measured voltage response of the sensor. Averaging of the power spectral density was performed to illustrate more clearly the noise source contributions.

Figure 5B.16 reaffirms what was calculated above; that intensity fluctuations from the the source laser is the dominating noise source of these post-correction taken with the OMIS. The contribution from parasitic cavities is diminished due to the fact this measurement occurred in a relatively quiet environment.

Chapter 6

Conclusion

Mitigation of inertial noise in atom interferometry based gravimeters through the use of inertial noise post-correction has been demonstrated. Post-correction with commercial sensors such as the **Titan** and **Trillium 240** has achieved inertial noise post-correction in low inertial noise environments and high inertial motion environments. In a low inertial noise environment we were able use the **Trillium 240** to post-correct a $T = 78$ ms atom interferometer from a short term uncertainty of $\sigma_{\text{UPC}}^{\text{Trillium}} = 4.4 \times 10^{-6} \text{ m/s}^2/\sqrt{\text{Hz}}$ to $\sigma_{\text{PC}}^{\text{Trillium}} = 9.2 \times 10^{-7} \text{ m/s}^2/\sqrt{\text{Hz}}$. By introducing additional motion we were able to create a strong motion environment, where we able use the **Titan** to post-correct an for a $T = 10$ ms atom interferometer lowering its short term uncertainty of $\sigma_{\text{UPC}}^{\text{Titan}} = 7.4 \times 10^{-3} \text{ m/s}^2/\sqrt{\text{Hz}}$ to $\sigma_{\text{PC}}^{\text{Titan}} = 1.0 \times 10^{-4} \text{ m/s}^2/\sqrt{\text{Hz}}$ yielding a suppression factor of $\gamma = 73.8$. Commercial sensors were limited by either self noise, or the GABOR-limited high-pass filter, both of which resulted from the large frequency resolution of the post-correction signal.

Pilot tests of the OMIS demonstrated a novel sensor capable of performing inertial noise post-correction. The unique advantages of this sensor, such as integrability into the inertial reference, vacuum compatibility and test mass magnetic field insensitivity, show potential for miniaturization efforts that will eventually surpass what is possible with commercial sensors. With the opto-mechanical resonators we were able to show an improvement in the short term stability of $\sigma_{\text{PC}}^{\text{OMIS}} = 8 \times 10^{-3} \text{ m/s}^2/\sqrt{\text{Hz}}$ from $\sigma_{\text{UPC}}^{\text{OMIS}} = 5 \times 10^{-4} \text{ m/s}^2/\sqrt{\text{Hz}}$. Intensity noise of the source laser and parasitic cavities on the lead fiber prevented higher correlation of the atom interferometer with the OMIS.

In this final chapter we will discuss the future directions taken to improve inertial noise post-correction, as well as the impact and implementation of these techniques into future atom interferometers. Improvements of the OMIS and optical setup for inertial noise post-correction are currently underway; construction of new sensors, as well as a better optical setup to reduce frequency and intensity noise within this experiment. Lastly we will discuss developments with the OMIS that will extend past this experiment, and change how gravimetry is performed.

6.1 Improvements in the Post-Correction method

As seen in section 5 A.2.1, motion signal measurements on the order of $\Delta T_{PC} \sim 200$ ms corresponds to a large spectral resolution ΔF_{PC} , a concern for digital filtering. As mentioned previously, this problem can be alleviated by measuring continuously, resulting in an arbitrarily fine spectral resolution.

With higher spectral resolution one can change the nature of the sensor-atom interferometer relationship and use the atom interferometer signal to perform bias corrections on the commercial sensor [50]. As seen in section 5 A.2.1, classical motions sensors drift over long time periods. In the case of inertial navigation, such a drift is problematic and provide false information used for navigation over long time periods. To solve this problem, one could use an absolute accelerometer such as an atom interferometer, however the ‘dead-time’ between measurements in current systems is not suitable for the high repetition rate required for navigation. One can solve both problems by using an atom interferometer to correct long-term drifts of the commercial sensor, providing a hybrid sensor capable of measuring acceleration with a high repetition rate and long term stability.

6.2 Improvements to Post-Correction with the OMIS

The OMIS is independently undergoing active research at the DLR in *Bremen*, where new sensors are being constructed that address parasitic cavity limitations outlined in this thesis. Along with better optical systems for interrogation, these developments will increase the OMIS inertial sensitivity, and allow for better post-correction. Within this section several methods for improving sensor self noise will be outlined, ranging from measurements with lower resonance sensors, to altering the design of the sensor and improving the optical setup.

Low Resonance Frequency OMIS

The high frequency resonance of the OMIS gives us a large measurement bandwidth, allowing us to measure signal up to ≈ 7.7 kHz. However this is far above the corner frequency of the atom interferometer, meaning a large portion of the measurable frequency range of the OMIS is minimally affecting the atom interferometer, and therefore not pertinent to post-correction. By lowering the resonance frequency of the OMIS, we can increase the sensitivity of the sensor to lower frequency accelerations which as has been shown in section 5 A.2.5, are more relevant to inertial noise post-correction. Lowering the resonance increases the displacement to acceleration transfer function $\frac{|X(\omega)|}{|A(\omega)|}$ for frequencies below resonance. We can calculate the improvement by analyzing the displacement to acceleration transfer function for a lower resonance frequency. For example, for a 680 Hz sensor in the flat response region below resonance, we can see an improvement in signal of 130 times the 7.7 kHz sensor. Additionally, decreasing the sensor resonance ω_0 alters the OMIS relation to noise source contributions. Using the measured noise source contributions outlined in the previous chapter, we can calculate the change in noise source contribution for a lower resonance sensor, table 6.1.

As sensitivity to lower frequency motion increases, risks that the sensor leaves the linear measurement regime required for optical readout also increases. Unlike at 7.7 kHz, there is a large amount of ground motion in the 500-700 Hz range, risking excitation of the sensor resonance and possibly displacing the sensor out of the linear regime. Since these sensors are currently under construction,

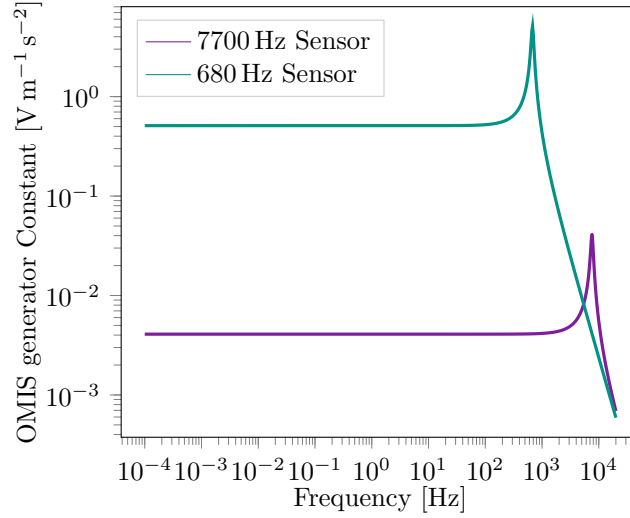


Figure 6.1: By reducing the mechanical resonance of the sensor we can increase the sensor’s sensitivity at lower frequency. Using parameters measured from OMIS 2 with the physical properties of a lower resonance sensor, we can calculate the increase in signal from a lower resonance sensor for an acceleration of 1 m s^{-2} . The response of the 680 Hz sensor to acceleration is a factor of 130 times more sensitive than the 7700 Hz sensor at 1 Hz

Table 6.1: Noise source contribution for a reduced resonance compared to the current high frequency resonance sensor.

Noise Source Contribution	$\omega_0 = 7700 \text{ Hz}$	$\omega_0 = 680 \text{ Hz}$
Frequency Noise	$2.1 \times 10^{-5} \text{ m/s}^2/\sqrt{\text{Hz}}$	$3.7 \times 10^{-7} \text{ m/s}^2/\sqrt{\text{Hz}}$
Intensity Noise (unfiltered)	$0.31 \text{ m/s}^2/\sqrt{\text{Hz}}$	$2.4 \times 10^{-3} \text{ m/s}^2/\sqrt{\text{Hz}}$

we have some preliminary values from these sensors and can perform some cursory calculations. To stay in the linear regime of the sensor, test mass displacement needs to remain less than $\approx 7.5\%$ of the free spectral range (FSR). For a sensor that has a resonance of 680 Hz, with an in-air Q of 700 and a cavity FSR of 775 nm, this means test mass displacement needs to remain below $\sim 30 \text{ nm}$ which corresponds to an acceleration of $\tilde{a}_{\text{RMS}} = 6 \times 10^{-4} \text{ m s}^{-2}$ and a displacement of $5 \times 10^{-10} \text{ m}$. For reference ground motion in our laboratory environment at 680 Hz is $\tilde{a}_{\text{ground}} \approx 5 \times 10^{-5} \text{ m s}^{-2}$.

During construction of these new sensors, additional features have been implemented. Light exiting a fiber tip diverges, which limits the amount of light reflected from the cavity. This problem is exacerbated by large cavity lengths, such as those achieved with the lower resonance cavity. This new sensor utilizes a gradient-index (GRIN) lens attached to the fiber tip to collimate the light entering the cavity. Lastly a quarter wave plate is implemented directly after the GRIN lens so that reflected light re-entering the lead fiber has orthogonal polarization to the light entering. This allows for the use of a polarizing beam-splitter instead of using an optical circulator.

Higher Finesse Cavity

An additional method for improving the sensitivity of the OMIS covered in this thesis is to increase the optical finesse of the OMIS cavity. This can either be achieved by coating the fiber tips, or through the implementation of fiber BRAGG gratings [100]. By increasing the finesse, we can increase the sensitivity of the sensor to test mass motion, while the signal from parasitic cavities within the lead fiber remains the same.

Experimentally a higher finesse cavity will manifest as an increase of $\frac{dV}{d\lambda}$. To estimate the increase in OMIS sensitivity we can calculate the increase in slope of the mid-fringe point as a function of finesse. By normalizing these slopes relative to a cavity with $\mathcal{F} = 2$, we can determine the gain of OMIS sensitivity as a function of finesse (6.2).

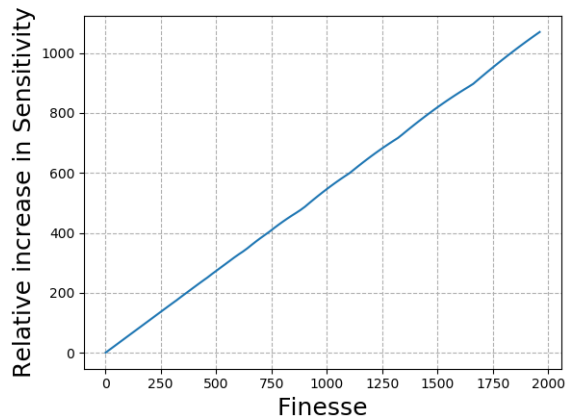


Figure 6.2: The increase in OMIS sensitivity relative to the OMIS 2.

Upgraded optical setup

As is clear from the previous chapter, intensity noise from the source laser is currently limiting post-correction with the OMIS. To reduce this noise source, we need to upgrade the optical setup and implement intensity stabilization. This can be performed in the future using a monitoring diode and an acousto-optic modulator¹. With a portion of light after the optical isolator diverted to a photo-detector, changes in intensity can be corrected feeding the error signal to the AOM.

In the case that frequency noise ever presents the limitation to OMIS measurement sensitivity, the frequency noise contribution can be reduced through frequency locking the source laser. With the current operational setup within the context of atom interferometer post-correction, this is easily possible by frequency doubling the 1560 nm light and offset locking to the ^{87}Rb D_2 transition.

¹In the case of a Gooch and Housego FIBER-Q FIBER COUPLED MODULATORS, the AOM is fiber coupled, leading to a completely fiber coupled system.

6.3 Outlook with Future Sensors

The integration of the OMIS into our inertial post correction system has proven fruitful and the techniques learned here can be applied gravimeters that are under development.

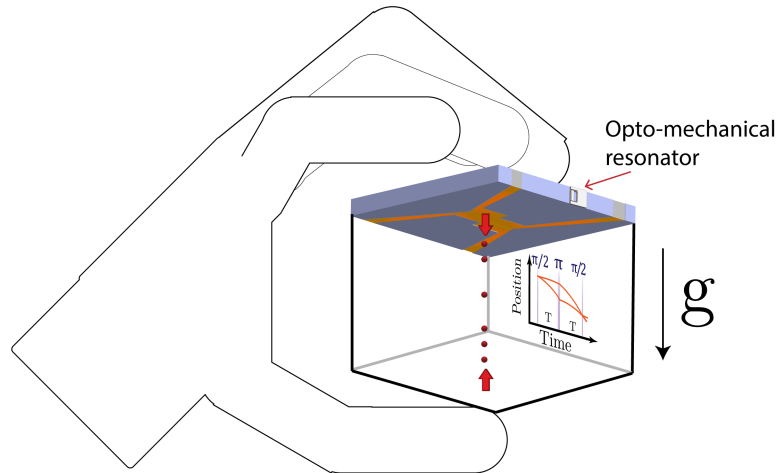


Figure 6.3: The ‘gravity in hand’ concept. A miniature sensor head small enough to hold in one hand could be deployed for field use, with the OMIS directly integrated into the atom chip. This device could measure the gravitation acceleration without vibration isolation, with the OMIS providing the inertial noise post-correction.

One of the benefits of the opto-mechanical sensors is the relative simplicity of materials and construction. The versatility of these sensors allow for them to be directly implemented into the inertial reference point. For example, in the case of our experiment, we could integrate the OMIS directly into the center of motion of the retro-reflection mirror, or in the case of portable gravimeters, we can directly integrate the sensor into the atom chip. This offers a complete solution for future experiments where light used for the cooling and trapping could also be used for optical interrogation the OMIS.

These advances alongside developments in miniaturization of atom gravimeters could help provide portable gravimeters capable of measuring the location of resources, or geological phenomena without the need for vibration isolation platforms. Direct integration of the OMIS could help portable gravimeters such as QG-1; future space missions such as BECCAL; or eventually extremely portable devices such as the “Gravity in hand” concept.

In total the inertial noise post-correction demonstrated within this thesis can be applied to any atom interferometer, reducing one of the largest contributions limiting accurate measurements of acceleration. The work in this thesis represents a step on the path towards portable absolute gravimeters capable of measuring in inertially noisy environments, something not possible with current classical devices.

Appendix A

Sensors

A.1 Motion Sensing

For vibration post correction to be possible we need to be able to record the motion of the retro-reflection mirror during a measurement cycle. Before use of the optomechanical inertial sensor (OMIS) was possible, we used readily available sensors available on the commercial market. To understand how we perform inertial noise post-correction and its limitations, we need to understand the operating principles behind these classical sensors.

In the course of this research we used readily available commercial sensors such as accelerometers capable of measuring accelerations and seismometers which measure velocity. The distinction between accelerometers and seismometers is mostly a historical one, by taking the derivative or using the appropriate sensitivity function both accelerometers and seismometers perform the same purpose¹. For this reason we will refer to both accelerometers and seismometers as commercial **motion sensors**.

The common thread of these sensors is that they are capable of measuring ground motion and outputting an electric potential that is a function of said ground motion. From this output we can convert the output using a generator constant to convert from a voltage to an acceleration.

A.1.1 Simple Harmonic Oscillator Model

In the simplest case we can approximate a ground motion sensor as a damped harmonic oscillator comprised of a test mass M , attached to a spring with stiffness K , and damped by a dampener R . For a ground motion $x(t)$ and test mass position $y(t)$ we define $z(t) = x(t) - y(t)$. We define any external force on the test mass as $f(t)$.

$$M\ddot{z}(t) = f(t) - Kz(t) - R\dot{z}(t) \tag{A.1}$$

From which we can get the relation:

¹The distinction between accelerometers and seismometers typically reflects a frequency band that they are capable of being measured in. Seismometers usually reflect a low frequency range, while accelerometers typically can measure in higher frequencies and have higher dynamic range. The reasons for this will become apparent.

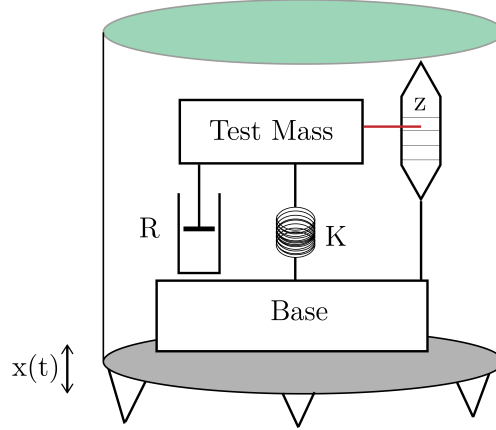


Figure A.1: A simplified model of how a classical motion sensor works. We can approximate the sensor as a dampened harmonic oscillator with a test mass M , spring stiffness K , and dampener R .

$$M\ddot{z}(t) + Rz\dot{(t)} + Kz(t) = f(t) - M\ddot{x}(t) \quad (\text{A.2})$$

For now we assume² $f(t) = -M\ddot{x}(t)$. So for a ground motion of $x(t)$ which applies a force $-M\ddot{x}(t)$ to the mass. In order to keep the test mass in place current is sent to an electromagnetic transducer.

We can use the LAPLACIAN relationship for a general differential equation:

$$\mathcal{L}\{a_0\ddot{p}(t) + a_1\dot{p}(t) + a_2p(t) = b_0\ddot{q}(t) + b_1\dot{q}(t) + b_2q(t)\} \quad (\text{A.3})$$

$$a_0s^2P(s) + a_1sP(s) + a_2P(s) = b_0s^2Q(s) + b_1sQ(s) + b_2Q(s) \quad (\text{A.4})$$

We can perform a LAPLACE transform on equation A.2 to get the equation of motion for Z

$$s^2MZ(s) + sRZ(s) + KZ(s) = F - s^2MX \quad (\text{A.5})$$

Solving for $Z(s)$ we get:

$$Z(s) = \frac{(F/M - s^2X)}{s^2 + sR/M + S/M} \quad (\text{A.6})$$

From which we can try the trial solutions $X(t) = 1/2\pi X e^{-i\omega t}$ and $F(t) = 1/2\pi F e^{-i\omega t}$, from which we get:

$$T(\omega) = \frac{(F/M - \omega^2 X)}{-\omega^2 + \omega R/M + S/M} \quad (\text{A.7})$$

²Later we will discuss the validity and ramifications of this approximation. This approximation is part of the transfer function approximation.

Realistic Motion Sensor

The simple harmonic oscillator gives us a good working model for how motion sensors operate, but in reality their construction is more complicated. We will briefly discuss how they operate beyond the simple harmonic oscillator picture and how this can affect measurement.

The construction seismometers and accelerometers is slightly different and we will briefly outline the construction differences and the effect of this on post-correction.

Force-Balance-Accelerometers

Both the broadband seismometers and accelerometers utilize force balance. The concept here is to provide a feedback loop capable of keeping the tests masses within a set range. Small motion occurring due to ground motion is recorded, then sent back to re-position the mass.

This principle of force balance is employed in ‘strong-motion’ sensors (accelerometers). The servo-loop keeps the test mass in place, and can successfully measure down the DC frequency, however feedback defines the corner frequency, above which the sensor is less sensitive.

$$\frac{U}{\ddot{x}} = \frac{M_{\text{TM}}R_{\Omega}}{E} \quad (\text{A.8})$$

This means by simply changing the resistance we can increase the gain of the accelerometer. Indeed most commercial accelerometers allow us to tune the sensitivity of the sensor by internally or externally changing the resistor in the feedback.

Broad-Band Seismometers

A broadband sensor refers to a sensor capable of measuring in the 1 mHz-50 Hz. The sensitivity at lower frequencies is pertinent to post-correction with atom interferometers, however, they suffer from an extremely low clipping levels, and are unsuitable for seismically loud environments. For this reason, in our post-correction these devices can perform well, but only when placed onto vibration isolation platforms. The readout of these sensors are typically readout by measuring capacitance of the test-mass [101].

In the case of the Trillium 240, the sensor is designed in a ‘tri-axial configuration’, meaning three capacitive outputs are read out in an orthogonal basis \hat{u} , \hat{v} and \hat{w} . This configuration has the benefit that it is less sensitive to sensor tilting.

$$\begin{bmatrix} x \\ y \\ z \end{bmatrix} = \begin{bmatrix} 2 & -1 & -1 \\ 0 & \sqrt{3} & -\sqrt{3} \\ \sqrt{2} & \sqrt{2} & -\sqrt{2} \end{bmatrix} \begin{bmatrix} u \\ v \\ w \end{bmatrix} \quad (\text{A.9})$$

A.1.2 Frequency Response

The frequency response of a sensor is not flat, and will measure different amplitudes and phases for a given incoming frequency. This is known as the frequency response of the sensor.

$$U(\omega) = \frac{X(\omega)}{T(\omega)} \quad (\text{A.10})$$

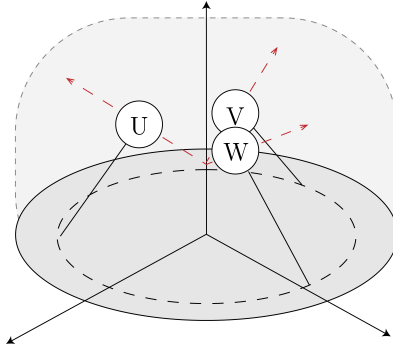


Figure A.2: The tri-axial configuration of the Titan. This configuration mitigates the problems of the horizontal axis having different sensitivities than the vertical. This configuration is currently only used in the **Nanometrics Trillium** and **Streckeisen STS-2**.

For motion at a given frequency $X(\omega)$, the sensor will transform the signal given by $T(\omega)$ and we will measure a signal from our sensor $U(\omega)$.

This frequency response is measured by the manufacturer and is determined by the individual components of the sensor. The frequency response of the sensor can be defined as a series of poles p_n and zeroes z_n following the relation:

$$T(S) = S_{\text{Sensor}} k \frac{\prod(S + p_n)}{\prod(S + z_n)} \quad (\text{A.11})$$

Defined by the poles and zeroes of the sensor. This will define the frequency response for the sensor. In the case of most of the sensors however post correction was performed over a small frequency range.

Bibliography

- [1] Alexander D. Cronin, Jörg Schmiedmayer, and David E. Pritchard. Optics and interferometry with atoms and molecules. *Rev. Mod. Phys.*, 81:1051–1129, Jul 2009. 8
- [2] Yannick Bidel, Olivier Carraz, Renée Charrière, Malo Cadoret, Nassim Zahzam, and Alexandre Bresson. Compact cold atom gravimeter for field applications. *Applied Physics Letters*, 102(14):144107, 2013. 8, 11
- [3] B. Desruelle, P. Vermeulen, V. Menoret, A. Landragin, P. Bouyer, N. Le Moigne, G. Gabalda, and S. Bonvalot. Sub Gal Absolute Gravity Measurements with a Transportable Quantum Gravimeter. *AGU Fall Meeting Abstracts*, December 2017. 8, 11
- [4] C Freier, M Hauth, V Schkolnik, B Leykauf, M Schilling, H Wziontek, H-G Scherneck, J Müller, and A Peters. Mobile quantum gravity sensor with unprecedented stability. *Journal of Physics: Conference Series*, 723(1):012050, 2016. 8, 11
- [5] G Tackmann, P Berg, C Schubert, S Abend, M Gilowski, W Ertmer, and E M Rasel. Self-alignment of a compact large-area atomic sagnac interferometer. *New Journal of Physics*, 14(1):015002, 2012. 8
- [6] P. Berg, S. Abend, G. Tackmann, C. Schubert, E. Giese, W. P. Schleich, F. A. Narducci, W. Ertmer, and E. M. Rasel. Composite-light-pulse technique for high-precision atom interferometry. *Phys. Rev. Lett.*, 114:063002, Feb 2015. 8
- [7] I Dutta, D Savoie, B Fang, B Venon, CL Garrido Alzar, R Geiger, and A Landragin. Continuous cold-atom inertial sensor with 1 nrad/sec rotation stability. *Physical review letters*, 116(18):183003, 2016. 8
- [8] G. Rosi, L. Cacciapuoti, F. Sorrentino, M. Menchetti, M. Prevedelli, and G. M. Tino. Measurement of the gravity-field curvature by atom interferometry. *Phys. Rev. Lett.*, 114:013001, Jan 2015. 8
- [9] Peter Asenbaum, Chris Overstreet, Tim Kovachy, Daniel D. Brown, Jason M. Hogan, and Mark A. Kasevich. Phase shift in an atom interferometer due to spacetime curvature across its wave function. *Phys. Rev. Lett.*, 118:183602, May 2017. 8
- [10] Peter W. Graham, Jason M. Hogan, Mark A. Kasevich, and Surjeet Rajendran. New method for gravitational wave detection with atomic sensors. *Phys. Rev. Lett.*, 110:171102, Apr 2013. 8

-
- [11] D. Schlippert, J. Hartwig, H. Albers, L. L. Richardson, C. Schubert, A. Roura, W. P. Schleich, W. Ertmer, and E. M. Rasel. Quantum test of the universality of free fall. *Phys. Rev. Lett.*, 112:203002, May 2014. 8, 13
- [12] Lin Zhou, Shitong Long, Biao Tang, Xi Chen, Fen Gao, Wencui Peng, Weitao Duan, Jiaqi Zhong, Zongyuan Xiong, Jin Wang, et al. Test of equivalence principle at 10^{-8} level by a dual-species double-diffraction raman atom interferometer. *Physical review letters*, 115(1):013004, 2015. 8
- [13] G Rosi, G D’Amico, L Cacciapuoti, F Sorrentino, M Prevedelli, M Zych, Č Brukner, and GM Tino. Quantum test of the equivalence principle for atoms in coherent superposition of internal energy states. *Nature communications*, 8:15529, 2017. 8
- [14] G Rosi, F Sorrentino, L Cacciapuoti, M Prevedelli, and GM Tino. Precision measurement of the newtonian gravitational constant using cold atoms. *Nature*, 510(7506):518–521, 2014. 8
- [15] Richard H Parker, Chenghui Yu, Weicheng Zhong, Brian Estey, and Holger Müller. Measurement of the fine-structure constant as a test of the standard model. *Science*, 360(6385):191–195, 2018. 8
- [16] Pierre Cladé, Estefania de Mirandes, Malo Cadoret, Saïda Guellati-Khélifa, Catherine Schwob, François Nez, Lucile Julien, and François Biraben. Determination of the fine structure constant based on bloch oscillations of ultracold atoms in a vertical optical lattice. *Phys. Rev. Lett.*, 96:033001, Jan 2006. 8
- [17] Kevin Watkins. Human development report 2006-beyond scarcity: Power, poverty and the global water crisis. 2006. 8
- [18] Mark Giordano and Karen G Villholth. *The agricultural groundwater revolution: opportunities and threats to development*, volume 3. CABI, 2007. 8
- [19] Peter Vajda. Recent developments and trends in volcano gravimetry. In *Updates in Volcanology-From Volcano Modelling to Volcano Geology*. InTech, 2016. 8
- [20] Jaroslava Pánisová and Roman Pašteka. The use of microgravity technique in archaeology: A case study from the st. nicolas church in pukaneč, slovakia. *Contributions to Geophysics and Geodesy*, 39(3):237–254, 2009. 8
- [21] E Issawy and A Radwan. Microgravimetry for archaeo-prospecting in luxor, egypt. In *Near Surface Geoscience 2012–18th European Meeting of Environmental and Engineering Geophysics*, 2012. 8
- [22] AH Jageler et al. Improved hydrocarbon reservoir evaluation through use of borehole-gravimeter data. *Journal of Petroleum Technology*, 28(06):709–718, 1976. 8
- [23] Y Bidel, N Zahzam, C Blanchard, A Bonnin, M Cadoret, A Bresson, D Rouxel, and MF Lequentrec-Lalancette. Absolute marine gravimetry with matter-wave interferometry. *Nature communications*, 9(1):627, 2018. 8

-
- [24] Cheinway Hwang, Tze-Chiang Cheng, CC Cheng, and WC Hung. Land subsidence using absolute and relative gravimetry: a case study in central taiwan. *Survey Review*, 42(315):27–39, 2010. 8
- [25] Albert Einstein and Marcel Grossmann. Kovarianzeigenschaften der feldgleichungen der auf die verallgemeinerte relativitätstheorie gegründeten gravitationstheorie. *Zeitschrift für Mathematik und Physik*, 63, 1914. 8
- [26] Charles W Misner, Kip S Thorne, and John Archibald Wheeler. *Gravitation*. Princeton University Press, 2017. 8
- [27] Isaac Newton. *Philosophiae naturalis principia mathematica*, volume 1. G. Brookman, 1833. 9
- [28] 9, 10, 45
- [29] JC Harrison and Tadahiro Sato. Implementation of electrostatic feedback with a lacostereomberg model g gravity meter. *Journal of Geophysical Research: Solid Earth*, 89(B9):7957–7961, 1984. 9
- [30] RP Middlemiss, Antonio Samarelli, DJ Paul, James Hough, Sheila Rowan, and GD Hammond. Measurement of the earth tides with a mems gravimeter. *Nature*, 531(7596):614, 2016. 9
- [31] Heikki Virtanen et al. Studies of earth dynamics with the superconducting gravimeter. 2006. 9
- [32] O Gerberding, F Guzmán Cervantes, J Melcher, J R Pratt, and J M Taylor. Optomechanical reference accelerometer. *Metrologia*, 52(5):654, 2015. 9, 13, 68
- [33] Glenn S Sasagawa, Fred Klopping, Timothy M Niebauer, James E Faller, and Richard L Hilt. Intracomparison tests of the fg5 absolute gravity meters. *Geophysical Research Letters*, 22(4):461–464, 1995. 10
- [34] Roberto Colella, Albert W Overhauser, and Samuel A Werner. Observation of gravitationally induced quantum interference. *Physical Review Letters*, 34(23):1472, 1975. 10
- [35] Jun John Sakurai and Eugene D Commins. *Modern quantum mechanics, revised edition*. AAPT, 1995. 10
- [36] John F Clauser and Shifang Li. Talbot-vonlau atom interferometry with cold slow potassium. *Physical Review A*, 49(4):R2213, 1994. 10
- [37] Fujio Shimizu, Kazuko Shimizu, and Hiroshi Takuma. Stark phase shift and deflection in the ultracold atomic interferometer. *Japanese journal of applied physics*, 31:L436–L438, 1992. 10
- [38] Mark Kasevich and Steven Chu. Atomic interferometry using stimulated raman transitions. *Physical review letters*, 67(2):181, 1991. 10, 20
- [39] M Kasevich and S Chu. Measurement of the gravitational acceleration of an atom with a light-pulse atom interferometer. *Applied Physics B*, 54(5):321–332, 1992. 10

-
- [40] Achim Peters, Keng Yeow Chung, and Steven Chu. Measurement of gravitational acceleration by dropping atoms. *Nature*, 400(6747):849, 1999. 10
- [41] D. Schlippert, H. Albers, L. L. Richardson, D. Nath, H. Heine, C. Meiners, É. Wodey, A. Billon, J. Hartwig, C. Schubert, N. Gaaloul, W. Ertmer, and E. M. Rasel. Ground Tests of Einstein’s Equivalence Principle: From Lab-based to 10-m Atomic Fountains. *ArXiv e-prints*, July 2015. 11, 45, 56
- [42] S. Abend, M. Gebbe, M. Gersemann, E. M. Rasel, and Quantus Collaboration. Symmetric large momentum transfer for atom interferometry with BECs. In *APS Division of Atomic, Molecular and Optical Physics Meeting Abstracts*, page P9.005, April 2017. 11
- [43] Leonardo Salvi, Nicola Poli, Vladan Vuletić, and Guglielmo M. Tino. Squeezing on momentum states for atom interferometry. *Phys. Rev. Lett.*, 120:033601, Jan 2018. 11
- [44] Lin Zhou, Shitong Long, Biao Tang, Xi Chen, Fen Gao, Wencui Peng, Weitao Duan, Jiaqi Zhong, Zongyuan Xiong, Jin Wang, Yuanzhong Zhang, and Mingsheng Zhan. Test of equivalence principle at 10^{-8} level by a dual-species double-diffraction raman atom interferometer. *Phys. Rev. Lett.*, 115:013004, Jul 2015. 11
- [45] P. Vermeulen, N. Lemoigne, V. Ménoret, B. Desruelle, A. Landragin, P. Bouyer, C. Busquet, A.-K. Cooke, S. Bonvalot, and J. Lautier Gaud. Evaluation of the repeatability and the stability of an operational Absolute Quantum Gravimeter. In *EGU General Assembly Conference Abstracts*, volume 20 of *EGU General Assembly Conference Abstracts*, page 17565, April 2018. 11
- [46] P A Altin, M T Johnsson, V Negnevitsky, G R Dennis, R P Anderson, J E Debs, S S Szigeti, K S Hardman, S Bennetts, G D McDonald, L D Turner, J D Close, and N P Robins. Precision atomic gravimeter based on bragg diffraction. *New Journal of Physics*, 15(2):023009, 2013. 11
- [47] Xuejian Wu, Fei Zi, Jordan Dudley, Ryan J. Bilotta, Philip Canozza, and Holger Müller. Multiaxis atom interferometry with a single-diode laser and a pyramidal magneto-optical trap. *Optica*, 4(12):1545–1551, Dec 2017. 11
- [48] Brynle Barrett, Laura Antoni-Micollier, Laure Chichet, Baptiste Battelier, Thomas Lévèque, Arnaud Landragin, and Philippe Bouyer. Dual matter-wave inertial sensors in weightlessness. *Nature Communications*, 7, 2016. 12, 13
- [49] F. Sorrentino, Q. Bodart, L. Cacciapuoti, Y.-H. Lien, M. Prevedelli, G. Rosi, L. Salvi, and G. M. Tino. Sensitivity limits of a raman atom interferometer as a gravity gradiometer. *Phys. Rev. A*, 89:023607, Feb 2014. 12, 13, 21, 42, 43, 44
- [50] Pierrick Cheiney, Lauriane Fouché, Simon Templier, Fabien Napolitano, Baptiste Battelier, Philippe Bouyer, and Brynle Barrett. Navigation-compatible hybrid quantum accelerometer using a kalman filter. *arXiv preprint arXiv:1805.06198*, 2018. 12, 89
- [51] Felipe Guzmán Cervantes, Lee Kumanchik, Jon Pratt, and Jacob M. Taylor. High sensitivity optomechanical reference accelerometer over 10 khz. *Applied Physics Letters*, 104(22):221111, 2014. 13

-
- [52] Marco Pisco, Francesco Antonio Bruno, Danilo Galluzzo, Lucia Nardone, Grzegorz Gruca, Niek Rijnveld, Francesca Bianco, Antonello Cutolo, and Andrea Cusano. Opto-mechanical lab-on-fibre seismic sensors detected the norcia earthquake. *Scientific reports*, 8, 2018. 13
- [53] Sébastien Merlet, J Le Gouët, Quentin Bodart, Andre Clairon, Arnaud Landragin, F Pereira Dos Santos, and Pierre Rouchon. Operating an atom interferometer beyond its linear range. *Metrologia*, 46(1):87, 2009. 13, 38
- [54] Christopher J Foot et al. *Atomic physics*, volume 7. Oxford University Press, 2005. 17, 24
- [55] JF Schaff, T Langen, and J Schmiedmayer. Interferometry with atoms. *Atom Interferometry (Proc. Int. School of Physics ‘Enrico Fermi’, Course 188, Varenna)*, pages 1–87, 2014. 20
- [56] J. Le Gouët, T.E. Mehlstäubler, J. Kim, S. Merlet, A. Clairon, A. Landragin, and F. Pereira Dos Santos. Limits to the sensitivity of a low noise compact atomic gravimeter. *Applied Physics B*, 92(2):133–144, Aug 2008. 21
- [57] D. Schlippert. *Quantum Tests of the Universality of Free Fall*. PhD thesis, Gottfried Wilhelm Leibniz Universität Hannover, 2014. 24, 31, 33
- [58] CG Townsend, NH Edwards, CJ Cooper, KP Zetie, CJ Foot, AM Steane, P Szriftgiser, H Perrin, and J Dalibard. Phase-space density in the magneto-optical trap. *Physical Review A*, 52(2):1423, 1995. 24, 29
- [59] K Dieckmann, RJC Spreeuw, M Weidemüller, and JTM Walraven. Two-dimensional magneto-optical trap as a source of slow atoms. *Physical Review A*, 58(5):3891, 1998. 24
- [60] J Schoser, A Batär, R Löw, V Schweikhard, A Grabowski, Yu B Ovchinnikov, and T Pfau. Intense source of cold rb atoms from a pure two-dimensional magneto-optical trap. *Physical Review A*, 66(2):023410, 2002. 24, 30
- [61] X Baillard, A Gauguet, S Bize, P Lemonde, Ph Laurent, A Clairon, and P Rosenbusch. Interference-filter-stabilized external-cavity diode lasers. *Optics Communications*, 266(2):609–613, 2006. 28
- [62] M Gilowski, Ch Schubert, M Zaiser, Werner Herr, T Wübbena, T Wendrich, T Müller, EM Rasel, and W Ertmer. Narrow bandwidth interference filter-stabilized diode laser systems for the manipulation of neutral atoms. *Optics Communications*, 280(2):443–447, 2007. 28
- [63] W. Herr. Realisierung eines schmalbandigen diodenlasersystems hoher ausgangsleistung zur rauscharmen detektion und manipulation von -atomen mit hilfe der atom-licht-wechselwirkung. Master’s thesis, Leibniz Universität Hannover, 2007. 28
- [64] J. Dalibard and C. Cohen-Tannoudji. Laser cooling below the doppler limit by polarization gradients: simple theoretical models. *J. Opt. Soc. Am. B*, 6(11):2023–2045, Nov 1989. 32
- [65] J. Dalibard and C. Cohen-Tannoudji. Laser cooling below the doppler limit by polarization gradients: simple theoretical models. *J. Opt. Soc. Am. B*, 6(11):2023–2045, Nov 1989. 32

- [66] J. Hartwig. *Analyse eines Atomaren Gravimeters hinsichtlich eines Quantentests des Äquivalenzprinzips*. PhD thesis, Gottfried Wilhelm Leibniz Universität Hannover, 2013. 33
- [67] Mark Kasevich, David S Weiss, Erling Riis, Kathryn Moler, Steven Kasapi, and Steven Chu. Atomic velocity selection using stimulated raman transitions. *Physical review letters*, 66(18):2297, 1991. 33
- [68] Keith D Bonin and Thomas J McIlrath. Two-photon electric-dipole selection rules. *JOSA B*, 1(1):52–55, 1984. 34
- [69] Daniel A Steck. Rubidium 87 d line data, 2001. 34
- [70] David W Allan. Statistics of atomic frequency standards. *Proceedings of the IEEE*, 54(2):221–230, 1966. 39
- [71] D. S. Weiss, B. C. Young, and S. Chu. Precision measurement of μ s based on photon recoil using laser-cooled atoms and atomic interferometry. *Applied Physics B*, 59(3):217–256, Sep 1994. 39
- [72] R Chicireanu, Karl D Nelson, S Olmschenk, Nathan Lundblad, A Derevianko, and James V Porto. Differential light-shift cancellation in a magnetic-field-insensitive transition of rb 87. *Physical review letters*, 106(6):063002, 2011. 39
- [73] Anne Louchet-Chauvet, Tristan Farah, Quentin Bodart, André Clairon, Arnaud Landragin, Sébastien Merlet, and Franck Pereira Dos Santos. The influence of transverse motion within an atomic gravimeter. *New Journal of Physics*, 13(6):065025, 2011. 39
- [74] Bing Cheng, Pierre Gillot, Sébastien Merlet, and F Pereira Dos Santos. Influence of chirping the raman lasers in an atom gravimeter: Phase shifts due to the raman light shift and to the finite speed of light. *Physical Review A*, 92(6):063617, 2015. 39
- [75] Jon R. Peterson. Observations and modeling of seismic background noise. Technical report, U.S. Geological Survey, 1993. 41
- [76] Berger Jonathan, Davis Peter, and Ekström Göran. Ambient earth noise: A survey of the global seismographic network. *Journal of Geophysical Research: Solid Earth*, 109(B11). 41
- [77] Bryan O Skipp. *Ground dynamics and man-made processes: prediction, design and management*. Thomas Telford, 1998. 41
- [78] Victor V Krylov. *Noise and vibration from high-speed trains*. Thomas Telford, 2001. 41
- [79] P Gillot, O Francis, A Landragin, F Pereira Dos Santos, and S Merlet. Stability comparison of two absolute gravimeters: optical versus atomic interferometers. *Metrologia*, 51(5):L15, 2014. 45
- [80] Alberto Stochino, Riccardo DeSalvo, Yumei Huang, and Virginio Sannibale. Improvement of the seismic noise attenuation performance of the monolithic geometric anti-spring filters for gravitational wave interferometric detectors. *Nuclear Instruments and Methods in Physics Research Section A: Accelerators, Spectrometers, Detectors and Associated Equipment*, 580(3):1559 – 1564, 2007. 45

-
- [81] D. Vassalos and S. Huang. Dynamics of small-sagged taut-slack marine cables. *Computers Structures*, 58(3):557 – 562, 1996. 49
- [82] *NI-DAQmx Python Documentation*. 50
- [83] R. Kirchhoff, C. M. Mow-Lowry, V. B. Adya, G. Bergmann, S. Cooper, M. M. Hanke, P. Koch, S. M. Köhlenbeck, J. Lehmann, P. Oppermann, J. Wöhler, D. S. Wu, H. Lück, and K. A. Strain. Huddle test measurement of a near johnson noise limited geophone. *Review of Scientific Instruments*, 88(11):115008, 2017. 61
- [84] Kristi Twilley, Helena Murvosh, Jin Cheng, Barbara Luke, Don Rock, and Yimin Tu. Deployment of a passive seismic array to remotely monitor for rockfall in underground excavations. 08 2018. 61
- [85] Dennis Gabor. Theory of communication. part 1: The analysis of information. *Journal of the Institution of Electrical Engineers-Part III: Radio and Communication Engineering*, 93(26):429–441, 1946. 63
- [86] A Peters, K Y Chung, and S Chu. High-precision gravity measurements using atom interferometry. *Metrologia*, 38(1):25, 2001. 65
- [87] Markus Aspelmeyer, Tobias J. Kippenberg, and Florian Marquardt. Cavity optomechanics. *Rev. Mod. Phys.*, 86:1391–1452, Dec 2014. 68
- [88] Stefan Nimmrichter, Klaus Hornberger, and Klemens Hammerer. Optomechanical sensing of spontaneous wave-function collapse. *Phys. Rev. Lett.*, 113:020405, Jul 2014. 68
- [89] Pavel Sekatski, Markus Aspelmeyer, and Nicolas Sangouard. Macroscopic optomechanics from displaced single-photon entanglement. *Phys. Rev. Lett.*, 112:080502, Feb 2014. 68
- [90] Sebastian G. Hofer, Denis V. Vasilyev, Markus Aspelmeyer, and Klemens Hammerer. Time-continuous bell measurements. *Phys. Rev. Lett.*, 111:170404, Oct 2013. 68
- [91] K. Stannigel, P. Komar, S. J. M. Habraken, S. D. Bennett, M. D. Lukin, P. Zoller, and P. Rabl. Optomechanical quantum information processing with photons and phonons. *Phys. Rev. Lett.*, 109:013603, Jul 2012. 68
- [92] Xu Han, King Y Fong, and Hong X Tang. A 10-ghz film-thickness-mode cavity optomechanical resonator. *Applied Physics Letters*, 106(16):161108, 2015. 68
- [93] Kyu Hyun Kim, Gaurav Bahl, Wonsuk Lee, Jing Liu, Matthew Tomes, Xudong Fan, and Tal Carmon. Cavity optomechanics on a microfluidic resonator with water and viscous liquids. *Light: Science & Applications*, 2(11):e110, 2013. 68
- [94] Felipe Guzmán Cervantes, Lee Kumanchik, Jon Pratt, and Jacob M Taylor. High sensitivity optomechanical reference accelerometer over 10 khz. *Applied Physics Letters*, 104(22):221111, 2014. 68

- [95] Philipp Haslinger, Matt Jaffe, Victoria Xu, Osip Schwartz, Matthias Sonnleitner, Monika Ritsch-Marte, Helmut Ritsch, and Holger Müller. Attractive force on atoms due to blackbody radiation. *Nature Physics*, 14(3):257, 2018. 68
- [96] D. T. Smith, J. R. Pratt, and L. P. Howard. A fiber-optic interferometer with subpicometer resolution for dc and low-frequency displacement measurement. *Review of Scientific Instruments*, 80(3):035105, 2009. 69
- [97] Stefano Bottacchi. *Noise and Signal Interference in Optical Fiber Transmission Systems*. Wiley, 2009. 83
- [98] Long-Sheng Ma, Peter Jungner, Jun Ye, and John L. Hall. Delivering the same optical frequency at two places: accurate cancellation of phase noise introduced by an optical fiber or other time-varying path. *Opt. Lett.*, 19(21):1777–1779, Nov 1994. 83
- [99] Paulo Antunes, Fatima Domingues, Marco Granada, and Paulo Andre. Mechanical properties of optical fibers. 02 2012. 84, 86
- [100] K. O. Hill and G. Meltz. Fiber bragg grating technology fundamentals and overview. *Journal of Lightwave Technology*, 15(8):1263–1276, Aug 1997. 91
- [101] R V Jones and J C S Richards. The design and some applications of sensitive capacitance micrometers. *Journal of Physics E: Scientific Instruments*, 6(7):589, 1973. 98

